Transport in Low Dimensional Systems with Spin-Orbit Coupling

Dissertation
zur Erlangung des Doktorgrades
des Fachbereichs Physik
der Universität Hamburg

vorgelegt von
Maxim Trushin
aus Saransk

Hamburg
2005

Gutachter der Dissertation: Prof. Dr. D. Pfannkuche
Priv. Doz. Dr. S. Kettemann

Gutachter der Disputation: Prof. Dr. A. Lichtenstein
Dr. A. Chudnovskiy

Datum der Disputation: 22.12.2005

Vorsitzender des Prüfungsausschusses: Prof. Dr. M. Rübhausen

Vorsitzender des Promotionsausschusses: Prof. Dr. G. Huber

Dekan des Fachbereichs Physik: Prof. Dr. G. Huber

Zusammenfassung

Diese theoretische Arbeit beschäftigt sich mit dem Elektronen-Transport in einem eindimensionalen System mit Rashba Spin-Bahn Kopplung.

Als erstes Ergebnis dieser Arbeit haben wir die Manifestation einer Spin-Orbit Berry Phase in der Leitfähigkeit eines mesoscopischen Ringes mit Rashba Spin-Bahn Kopplung und externem Magnetfeld senkrecht zur Ringebene. Speziell wurden die Transmissionswarscheinlichkeiten für einen geraden Quantendraht und für einen Quantenring aus demselben Material berechnet und miteiander verglichen. Der Unterschied zwieschen den beiden wurde untersucht und als Manifestation einer Spin-Orbit Berry Phase indentifieziert. Ebenso wurde die Manifestation einer nicht adiabatischen Aharonov-Anandan Phase bei kleinen Ringdurchmessern gefunden.

Als zweites Ergebnis haben wir festgestellt, dass ein stark gekrümmter, eindimensionaler, ballistischer Draht mit intrinsischer Spin-Bahn Wechselwirkung in der Lage ist, die Stromdichte zwischen zwei Spin-aufgespalteten Moden zu verteilen und somit die Möglichkeit bietet, die Spinpolarization zu ändern ohne ferromagnetische Kontakte, Tunnelbarieren, externe Felder oder dergleichen zu verwenden. Unter Verwendung der für InAs relevanten Parameter, schlagen wir auf Grundlage dieses Effekts ein reflektionslosen Spinschalter vor.

Als drittes Ergebnis beschreiben wir ein eindimensionales System, in dem die Fermigeschwindigkeit wie auch die Zustandsdichte für die sich nach links und nach rechts bewegenden Elektronen ungleich sind. Ein solches System kann sich in einem isolierten Quantenring mit Spin-Bahn Kopplung und senkrechtem magnetischen Feld herausbilden. Um den Einfluss der Elektron-Elektron Wechselwirkung auf die chirale Asymmetrie der Zustandsdichte beschreiben zu können, wird das Tomonaga-Luttinger Model angewandt. Wie sich herausstellt, führt die Elektron-Elektron Wechselwirkung zu einer Ausrichtung der Zustandsdichte der sich nach links und nach rechts bewegenden Elektronen. Zusätzlich wurde der Landauer-Büttiker Formalismus für ein System mit chiraler Asymmetrie der Zustandsdichte veralgemeinert.

Abstract

This is a theoretical study of electron transport in one-dimensional systems with spin-orbit coupling of Rashba type.

First, we have found a manifestation of spin-orbit Berry phase in the conductance of a mesoscopic loop with Rashba spin-orbit coupling placed in an external magnetic field perpendicular to the loop plane. In detail, the transmission probabilities for a straight quantum wire and for a quantum loop made of the same wire have been calculated and compared with each other. The difference between them has been investigated and identified with a manifestation of spin-orbit Berry phase. The manifestation of a non-adiabatic Aharonov-Anandan phase at small radii of the loop has been found as well.

Second, we have found that a strongly curved one-dimensional ballistic wire with intrinsic spin-orbit interactions can redistribute the current density between the two spin-split modes and, thus, makes it possible to change the spin-polarization without using ferromagnetic contacts, tunneling barriers, external radiation etc. Assuming parameters relevant for InAs we propose a scheme of a reflectionless spin-switch based on this effect.

Third, we have described a one-dimensional system, where the Fermi velocities (as well as the densities of states) for the left- and right-moving electrons are not equal to each other. Such a system can be formed in an isolated quantum loop with spin-orbit coupling placed into a magnetic field perpendicular to the loop plane. The Tomonaga-Luttinger model has been applied in order to describe the influence of electron-electron interactions on the chiral asymmetry of the density of states. We have found, that electron-electron interactions lead to the alignment of the densities of states for the left- and right- moving electrons. In addition, the Landauer-Büttiker formalism has been generalized for systems with chiral asymmetry of the density of states.

4

Contents

1 Spintronics and spin-orbit coupling in semiconductors

Spintronics is one of the most promising fields of modern solid state physics in view of its possible applications in commercial electronic devices. In contrast to mainstream electronics in which the spin of the electron is ignored, the basic concept of spintronics is the combination of standard microelectronics and spin-dependent effects that arise from the interaction between spin of the carrier, its orbital degree of freedom and magnetic properties of the material. One of such spin-dependent effects found in many semiconductor structures is the so-called spin-orbit coupling (in particular, Rashba spin-orbit coupling). In general, the effect is due to the spatial inverse symmetry breaking that occurs in some crystals of zinc blende type structure as well as in low dimensional systems with asymmetric confinement.

Adding the spin degree of freedom to conventional semiconductor charge-based electronics or using the spin degree of freedom alone will add substantially more capability and performance to electronic products. The advantages of these new devices would be their non-volatility, increased data processing speed, decreased electric power consumption, and increased integration densities compared with conventional semiconductor devices [1]. The foregoing example is meant to illustrate that the switching speed of an ideal device based on the Rashba spin-orbit coupling effect in InAs structure is much higher than the characteristic speeds of nowadays microelectronics elements.

In order to switch any of conventional semiconductor devices (e. g. transistor), one has to remove (or add) a huge amount of electrons from (or to) the conduction band by means of the external electric field. All manipulations of that kind bring about a waste of time and energy. Therefore, the switching speed of modern transistors tops out at a cycle time of between 2.5 and 10 GHz [2]. Moreover, the overheating of the chip can be a big problem.

In contrast, a spintronics element operates not with an electron itself, but with its spin orientation. It is not necessary to transfer all the electrons from one place to another for each cycle; it is enough just to change their spin-orientation. (The electrons, of course, must be spin-polarized.) Let us estimate the switching speed of the spintronic device based on Rashba effect in the ballistic transport regime. We take the parameters relevant for InAs, i. e. the characteristic length of the "active" region necessary to rotate the electron spin to its opposite direction is equal to $\sim 10^{-5}$cm (spin precession length), whereas the characteristic velocity is $5 \cdot 10^7$cm/s. Then we have, that the cycle time is 0.2ps that corresponds to 5 THz. Thus, hypothetical spintronic computers might be one thousand times faster than conventional ones!

In view of the importance of the Rashba effect in spintronics, it has become necessary to inves-

tigate properties related to the spin-orbit coupling in low-dimensional systems. This will be the main topic addressed in this work.

This thesis is organized as follows. In the Chapter 2, we explain the origin of the Rashba effect using very general solutions of the Dirac equation. In the same Chapter we give a brief overview of recent work concerning the geometrical phases in solid state physics and progress in spin-manipulation. The introduction to the Tomonaga-Luttinger model in connection with spin-dependent effects is given as well.

In the next three Chapters, we focus on the interplay between Rashba spin-orbit coupling, Zeeman effect, electron-electron interactions in one-dimensional systems of non-zero curvature. The spin-orbit Berry phase in a quantum loop will be investigated in the Chapter 3. In the Chapter 4, we show how curved one-dimensional wires with intrinsic spin-orbit interactions can redistribute the current density between two spin-split modes. In addition, the spin-switching device based on this effect is proposed.

The results of Chapter 5 are more fundamental. The chiral asymmetry of electron density of states is found in a curved one-dimensional wire with Rashba coupling and Zeeman spin-splitting. The influence of electron-electron interactions on the chiral asymmetry is studied as well. The Landauer-Büttiker formalism is generalized to apply to systems with the chiral asymmetry of the density of states.

At the end of the beginning, we wish the reader to enjoy the thesis.

2 Rashba effect in low-dimensional systems: origin and manifestations

In this chapter we show how the Rashba spin-orbit coupling term arises in the Hamiltonian of an electron gas placed in an external electric field. Three-, two- and one-dimensional cases are considered. It is shown that the Rashba effect in one-dimensional rings leads to the effective magnetic field crown-like texture and in that way makes it possible to observe the spin-orbit Berry's phase. Moreover, the applications of Rashba effect in spin-filtering technique are discussed. Finally, we give an introduction to the Tomonaga-Luttinger model and discuss its applications to one-dimensional systems with spin-dependent effects (such as Rashba and Zeeman ones).

2.1 Spin-orbit interactions in a bulk sample

It has been established both theoretically and experimentally that in electron gases of narrow-gap semiconductors there is an energy splitting between up-spin and down-spin electrons even when there is no magnetic field. The dominant mechanism for this "zero-field spin-splitting" is believed to be spin-orbit interactions. We focus here on the spin-orbit coupling of Rashba form. Other mechanisms for bulk structures such as the bulk inversion asymmetry term (spin-orbit interactions of Dresselhaus form) also contribute to the zero-field spin splitting; however we ignore these here as they are usually smaller in narrow-gap semiconductors.

The problem of an electron moving in a solid is usually treated using the stationary Schrödinger equation

$$\frac{1}{2m}\left(\mathbf{p}-\frac{e}{c}\mathbf{A}\right)^2\psi + e\phi(\mathbf{r})\psi = E\psi, \tag{2.1}$$

where $\phi(\mathbf{r})$ is a given electrostatic potential, $\mathbf{p}$ is the electron momentum, $\mathbf{A}$ is the vector potential, and $e = |e|$, m are the electron charge and mass respectively. The electron spin has, however, essentially relativistic origin. Therefore, the non-relativistic stationary Schrödinger equation (2.1) could not be used for the description of spin-orbit interactions in the electron motion.

In order to introduce the appropriate spin-orbit interaction term into (2.1), we start with the four-component Dirac equation

$$i\hbar\frac{\partial\Psi(\mathbf{r},t)}{\partial t} = H_D\Psi(\mathbf{r},t). \tag{2.2}$$

Here

$$H_D = \alpha c\left(\mathbf{p}-\frac{e}{c}\mathbf{A}\right) + \beta mc^2 + I_4 e\phi(\mathbf{r}), \tag{2.3}$$

where

$$\alpha = \begin{pmatrix} \sigma & 0 \\ 0 & -\sigma \end{pmatrix}, \quad \beta = \begin{pmatrix} 0 & I_2 \\ I_2 & 0 \end{pmatrix}, \quad I_4 = \begin{pmatrix} I_2 & 0 \\ 0 & I_2 \end{pmatrix}, \tag{2.4}$$

I_2 is the unit matrix 2×2

$$I_2 = \begin{pmatrix} 1 & 0 \\ 0 & 1 \end{pmatrix}, \tag{2.5}$$

and σ are the Pauli matrices

$$\sigma_x = \begin{pmatrix} 0 & 1 \\ 1 & 0 \end{pmatrix}, \quad \sigma_y = \begin{pmatrix} 0 & -i \\ i & 0 \end{pmatrix}, \quad \sigma_z = \begin{pmatrix} 1 & 0 \\ 0 & -1 \end{pmatrix}. \tag{2.6}$$

The usual way [3] to solve the Dirac equation (2.2) is to reduce it to two components using the substitution

$$\Psi(\mathbf{r},t) = \Psi'(\mathbf{r},t)e^{-itmc^2/\hbar}, \tag{2.7}$$

where

$$\Psi'(\mathbf{r},t) = \begin{pmatrix} \varphi'(\mathbf{r},t) \\ \vartheta'(\mathbf{r},t) \end{pmatrix}. \tag{2.8}$$

Then we have the following system of equations

$$\begin{cases} \left(i\hbar\frac{\partial}{\partial t} + mc^2 - e\phi(\mathbf{r}) \right) \varphi' &= mc^2\vartheta' + c\sigma\left(\mathbf{p} - \frac{e}{c}\mathbf{A}\right)\varphi', \\ \left(i\hbar\frac{\partial}{\partial t} + mc^2 - e\phi(\mathbf{r}) \right) \vartheta' &= mc^2\varphi' - c\sigma\left(\mathbf{p} - \frac{e}{c}\mathbf{A}\right)\varphi'. \end{cases} \tag{2.9}$$

Performing a second substitution

$$\tilde{\varphi}' = \frac{\varphi' + \vartheta'}{2}, \quad \tilde{\vartheta}' = \frac{\varphi' - \vartheta'}{2}, \tag{2.10}$$

we arrive at

$$\begin{cases} \left(i\hbar\frac{\partial}{\partial t} - e\phi(\mathbf{r}) \right) \tilde{\varphi}' &= c\sigma\left(\mathbf{p} - \frac{e}{c}\mathbf{A}\right)\tilde{\vartheta}', \\ \left(i\hbar\frac{\partial}{\partial t} + 2mc^2 - e\phi(\mathbf{r}) \right) \tilde{\vartheta}' &= c\sigma\left(\mathbf{p} - \frac{e}{c}\mathbf{A}\right)\tilde{\varphi}'. \end{cases} \tag{2.11}$$

From the second equation of (2.11) we have

$$\tilde{\vartheta}' = \left(i\hbar\frac{\partial}{\partial t} + 2mc^2 - e\phi(\mathbf{r}) \right)^{-1} c\sigma\left(\mathbf{p} - \frac{e}{c}\mathbf{A}\right)\tilde{\varphi}'. \tag{2.12}$$

The electron energy in solid state physics is much smaller than mc^2. Therefore, one can approximate (2.12) as

$$\tilde{\vartheta}' = \left[1 - \frac{\left(i\hbar\frac{\partial}{\partial t} - e\phi(\mathbf{r}) \right)}{2mc^2} \right] \frac{c\sigma\left(\mathbf{p} - \frac{e}{c}\mathbf{A}\right)}{2mc^2}\tilde{\varphi}'. \tag{2.13}$$

Using this approximate expression and the first equation of (2.11) we finally arrive at

$$\left(i\hbar\frac{\partial}{\partial t} - e\phi(\mathbf{r}) \right) \tilde{\phi}' = \frac{1}{2m} \left[\sigma\left(\mathbf{p} - \frac{e}{c}\mathbf{A}\right) \right] \left[\sigma\left(\mathbf{p} - \frac{e}{c}\mathbf{A}\right) \right] \tilde{\phi}'$$

$$-\frac{1}{4m^2c^2} \left[\sigma\left(\mathbf{p} - \frac{e}{c}\mathbf{A}\right) \right] \left(i\hbar\frac{\partial}{\partial t} - e\phi(\mathbf{r}) \right) \left[\sigma\left(\mathbf{p} - \frac{e}{c}\mathbf{A}\right) \right] \tilde{\phi}'. \tag{2.14}$$

This is the basic equation for description of spinfull electron motion. We find it necessary to make several remarks concerning (2.14). First of all, using the commutation relation between momentum and coordinate operators as well as relations between Pauli matrices $\sigma_x\sigma_y = i\sigma_z$, $\sigma_x\sigma_z = -i\sigma_y$, $\sigma_y\sigma_z = i\sigma_x$ one can show, that the first term on the right-hand side of eq. (2.14) is nothing else than the sum of ordinary kinetic and Zeeman energies. The second term on the right-hand side of eq. (2.14) gives actually two contributions. The first one is the negligible first-order of $E/2mc^2$ relativistic correction for kinetic and Zeeman energies, while the second one explicitly represents spin-orbit interactions. Let us finally note, that equation (2.14) is still time-dependent, while we are going to study stationary cases. Then, performing the standard substitution $\tilde{\phi}'(\mathbf{r},t) = \psi(\mathbf{r})\exp(-iEt/\hbar)$ in (2.14), we arrive at the stationary Schrödinger equation [cf. (2.1)] with relativistic corrections

$$\frac{1}{2m}\left(\mathbf{p} - \frac{e}{c}\mathbf{A}\right)^2 \psi - \mu_B\left(\sigma\cdot\mathbf{B}\right)\psi +$$

$$+\frac{1}{4m^2c^2}\left[\sigma\left(\mathbf{p} - \frac{e}{c}\mathbf{A}\right)\right] e\phi(\mathbf{r}) \left[\sigma\left(\mathbf{p} - \frac{e}{c}\mathbf{A}\right)\right] \psi + e\phi(\mathbf{r})\psi = E\psi. \tag{2.15}$$

Here $\mu_B = e\hbar/(2mc)$ is the Bohr magneton.

As from now, we call these relativistic corrections "spin-orbit coupling in general form" and use the notation

$$H_{SO} = \frac{1}{4m^2c^2}\left[\sigma\left(\mathbf{p} - \frac{e}{c}\mathbf{A}\right)\right] e\phi(\mathbf{r}) \left[\sigma\left(\mathbf{p} - \frac{e}{c}\mathbf{A}\right)\right]. \tag{2.16}$$

In the following, we study the effects of this term in some particular cases.

2.2 Rashba spin-orbit coupling in a two-dimensional electron gas

Let us consider the relativistic spin-orbit corrections H_{SO} in the case of a two-dimensional electron gas confined in the xy plane by a given electrostatic potential $V_c(z)$. Then the potential $\phi(\mathbf{r})$ in (2.15), (2.16) is nothing else than the confining one $\phi(z) = V_c(z)/e$ and the coresponding electric field $E(z)$ reads

$$E(z) = -\frac{\partial\phi(z)}{\partial z}.$$

It is important to note, that if the confining potential is symmetric $\phi(z) = \phi(-z)$, then the total electric field E_z experienced by the electrons in the 2D gas (see fig. 2.1) is zero. In contrast, $E_z \neq 0$ as soon as $\phi(z) \neq \phi(-z)$.
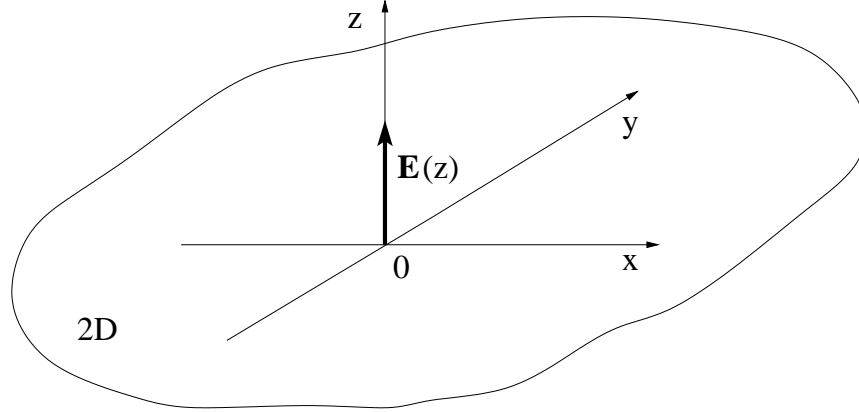
Figure 2.1: The coordinate system used throughout this thesis for the description of the 2D electron gas placed in the electric field **E**.

We restrict ourselves to the case of a homogeneous magnetic field $|\mathbf{B}| = B_z$ perpendicular to the electron gas plane. The gauge is chosen so, that

$$A_x = -\frac{1}{2}B_z y, \quad A_y = \frac{1}{2}B_z x, \quad A_z = 0. \tag{2.17}$$

Then, neglecting the terms of order

$$\left[\frac{1}{2m} \left(\mathbf{p} - \frac{e}{c}\mathbf{A} \right)^2 \right] \frac{e\phi(z)}{2mc^2},$$

we rewrite the spin-orbit coupling term (2.16) in the more conventional form

$$H_{SO} = \frac{e\hbar E_z}{4m^2 c^2} \left[i\hat{p}_z + \sigma_x \left(\hat{p}_y - \frac{e}{c}A_y \right) - \sigma_y \left(\hat{p}_x - \frac{e}{c}A_x \right) \right]. \tag{2.18}$$

As a final step, we assume, that the size quantization in z direction is so strong, that only one subband is occupied by electrons. Therefore, the p_z-dependent term in (2.18) gives just a constant (which is usually set to zero). Thus, the spin-orbit interaction term takes a form (the original Rashba form H_R [4, 5]) often encountered in the literature, namely

$$H_{SO} \equiv H_R = \alpha \left[\sigma \times \mathbf{k} \right]_z, \tag{2.19}$$

where the Rashba constant is

$$\alpha = \frac{e\hbar^2 E_z}{4m^2 c^2}, \tag{2.20}$$

and

$$\mathbf{k} = \frac{1}{\hbar} \left(\mathbf{p} - \frac{e}{c}\mathbf{A} \right)$$

is the electron wave vector. The Rashba constant α has the dimension of length×energy, and can not be measured directly. There are, however, several indirect methods (e. g. using Shubnikov-de Haas oscillations [6, 7, 8]) that allow to determine α.

Let us emphasize, that the spin-orbit coupling of Rashba type is associated with the interfacial electric field E_z in the quantum well that confines the two-dimensional electron gas. This electric field can be governed by the voltage applied to metallic gates on top of the heterojunction. Thus, such an internal property of semiconductor structures as spin-orbit coupling is experimentally tunable. This is a distinct feature of the 2D electron gas confined in a heterojunction compared to the bulk case. Of course, the spin-orbit interactions are present in bulk semiconductors as well (e. g. Dresselhaus spin-orbit coupling). However, these effects arise essentially from the particular (internal!) properties of the zinc-blende crystal lattice structure. The external tuning of bulk spin-orbit effects is, therefore, rather difficult. In contrast, the Rashba effect is much more promising in this sense. Indeed, tuning of the Rashba spin-orbit coupling by means of an external gate voltage was recently demonstrated in different semiconductors by Nitta et al. [9] and others [6, 10, 7] and more recently by Grundler [11] applying a back gate voltage while the carrier density was kept constant. It has also been achieved in a p-type InAs semiconductor by Matsuyama et al. [8].

2.3 Rashba spin-orbit interactions in one-dimensional structures

The results given in the previous section suggest, that confining electrons from bulk semiconductors with spin-orbit interactions to the two-dimensional limit is very useful since it allows the tunability of the Rashba constant. In this section, we address the question what new effects can be reached by further restriction of the dimensionality of the electron gas. Namely, we consider the one-dimensional case. In particular, we focus on the Rashba term (2.19) in the following two limits: (i) 1D wire (see fig. 2.2a), and (ii) 1D arc that is, in other words, a *curved* 1D wire (see fig. 2.2b).

The first limit is rather trivial. Indeed, assuming that the electron gas is confined in y direction so, that the k_y-dependent term in eq. (2.19) represents just a constant (which is set to zero) we arrive at the following simple form for the Rashba term

$$H_R^{\text{1Dwire}} = \begin{pmatrix} 0 & i\alpha\hat{k}_x \\ -i\alpha\hat{k}_x & 0 \end{pmatrix}, \tag{2.21}$$

where $\hat{k}_x = -i\frac{\partial}{\partial x}$.

The solutions of the Schrödinger equation for a 1D wire with the Hamiltonian $H^{\text{1Dwire}} = H_{\text{kin}}^{\text{1Dwire}} + H_R^{\text{1Dwire}}$, where $H_{\text{kin}}^{\text{1Dwire}} = \hbar^2 \hat{k}_x^2/2m$, read

$$\psi_{\text{1Dwire}}^+(x) = \frac{1}{\sqrt{2}}e^{ik^+x}\begin{pmatrix} 1 \\ -i \end{pmatrix}, \quad \psi_{\text{1Dwire}}^-(x) = \frac{1}{\sqrt{2}}e^{ik^-x}\begin{pmatrix} -i \\ 1 \end{pmatrix}, \tag{2.22}$$

where $k^\pm$ satisfy the dispersion relation

$$E_k^\pm = \frac{\hbar^2}{2m}(k \pm k_{\text{SO}})^2 - \frac{\hbar^2 k_{\text{SO}}^2}{2m}. \tag{2.23}$$
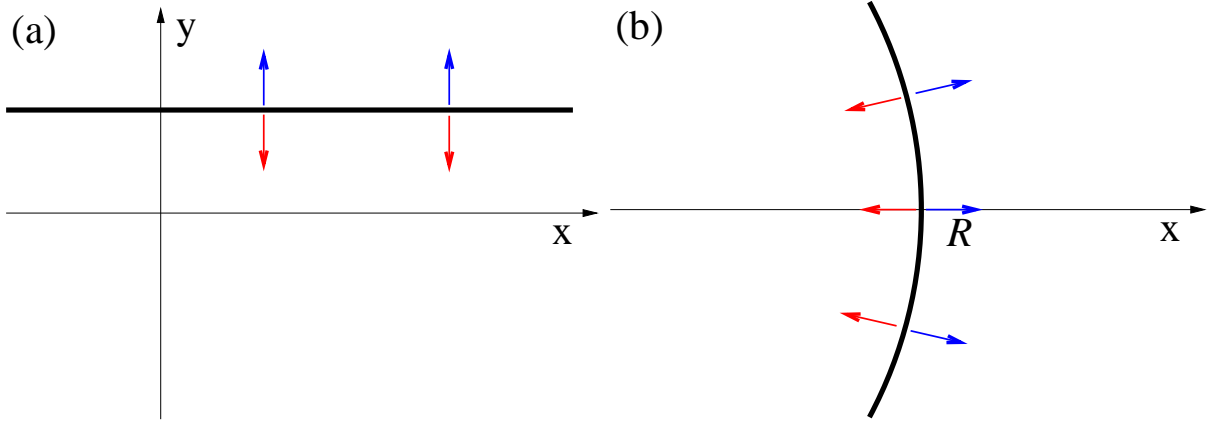
Figure 2.2: The solution of the Schrödinger equation (cf. fig. 2.3 and fig. 2.4) for a 1D wire in the presence of Rashba coupling depends strongly on whether the wire is straight (a) or curved (b). The arrows depict two possible spin directions in the eigen states of the system.

Here we have introduced the following constant characterizing Rashba spin-splitting (see fig. 2.3)

$$k_{SO} = \frac{m\alpha}{\hbar^2}. \tag{2.24}$$

Equation (2.23) always has two solutions with respect to k corresponding to left- and right-moving particles for a given spin index "+" or "−". Let us make some important comments on the eigen functions (2.22) and the dispersion relation (2.23).

First, both elements of spinors (2.22) are not equal to zero. This reflects the fact, that the spin quantization axis does not coincide with the z direction. In contrast, the electron spin in eigen states (2.22) is directed along the y axis (see fig. 2.2a). Thus, the electrons injected into a 1D wire in their eigen states (2.22) keep constant direction of their spins along that axis. If an electron is not in its eigen state ψ_{1Dwire}^+ or ψ_{1Dwire}^-, then the Rashba effect rotates the spin while it moves through the 1D wire. This particular fact is utilized in some spintronic devices such as spin field effect transistors (see section 5 of this Chapter).

Second, the Rashba coupling shifts the dispersion curves along the momentum axis by the value $\pm \hbar k_{SO}$ (depending on spin index) *and* along the energy axis by $-\hbar^2 k_{SO}^2/(2m)$. Notice, that the shift along the energy axis changes the Fermi velocity in the wire (if the Fermi level is fixed). However, in contrast to the Zeeman effect, this "vertical" shift does not depend on spin index.

Let us turn to the case of a wire with finite curvature (see fig. 2.2b). This case is not so trivial as one might think.

The conventional way to obtain the Hamiltonian for a 1D arc (or ring) from the Hamiltonian in 2D consists of two steps. The Hamiltonian operator is transformed into cylindrical coordinates r and φ. Adopting $x = r\cos\varphi$, $y = r\sin\varphi$, the momenta operators read

$$-i\hbar\frac{\partial}{\partial x} = -i\hbar\left(\cos\varphi\frac{\partial}{\partial r} - \frac{\sin\varphi}{r}\frac{\partial}{\partial\varphi}\right),$$
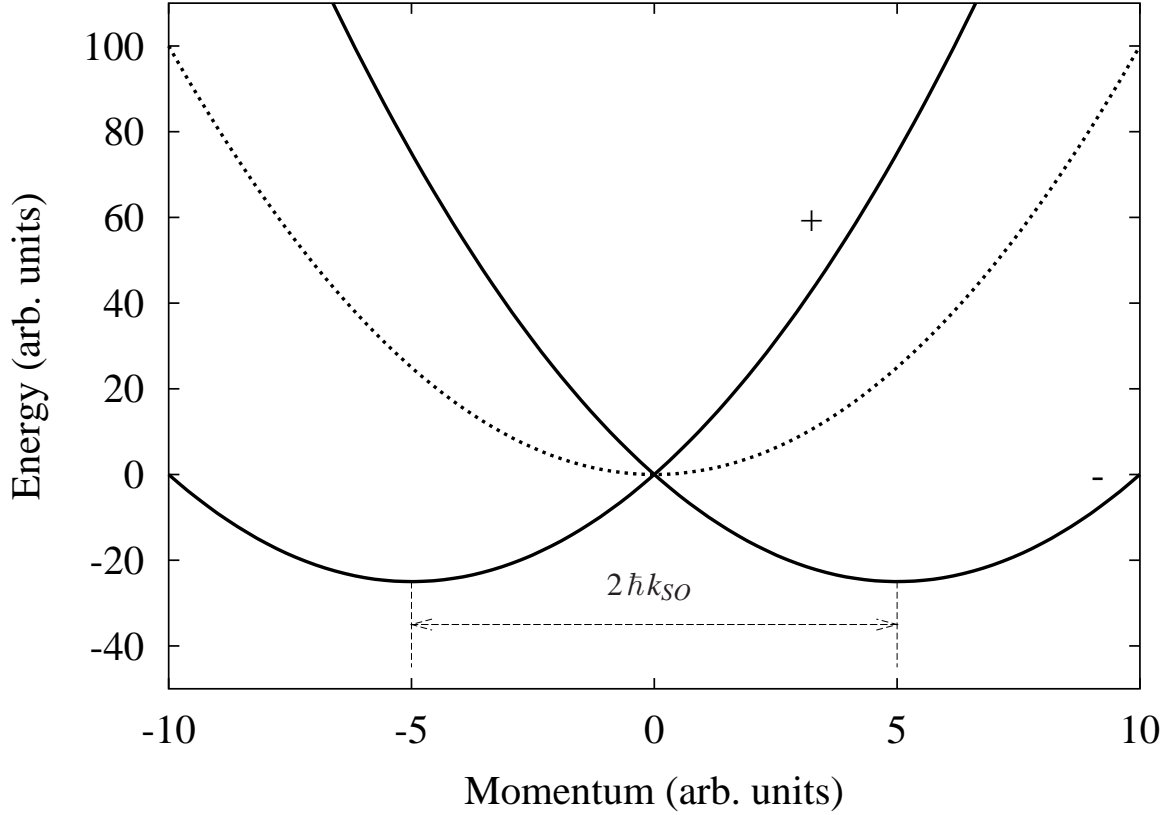
Figure 2.3: Typical dispersion law for a 1D wire with Rashba spin-orbit coupling given by the relation (2.23) (solid line). The dashed line corresponds to the case of zero spin-orbit coupling, i. e. $E_k^{\pm} = p^2/2m$, p being momentum. The signs "$\pm$" denote the spin indices. Note, that there is no spin-splitting at zero momentum.

$$-i\hbar\frac{\partial}{\partial y} = -i\hbar\left(\sin\varphi\frac{\partial}{\partial r} + \frac{\cos\varphi}{r}\frac{\partial}{\partial\varphi}\right);\tag{2.25}$$

and the Rashba operator acquires the following form

$$H_R = \alpha\begin{pmatrix} 0 & r^{-1}e^{-i\varphi}\left(-i\frac{\partial}{\partial\varphi}\right) + e^{-i\varphi}\frac{\partial}{\partial r} \\ r^{-1}e^{i\varphi}\left(-i\frac{\partial}{\partial\varphi}\right) - e^{i\varphi}\frac{\partial}{\partial r} & 0 \end{pmatrix}.\tag{2.26}$$

Then, naively one could set r to a constant R and discard all terms proportional to derivatives with respect to r. This procedure works perfectly in simple cases, such as free electrons or electrons in the presence of a uniform (or textured [12]) magnetic field. However, it does not work in the presence of Rashba spin-orbit interactions!

Indeed, let us have a closer look on the Rashba operator for curved 1D system obtained by the

conventional procedure described above

$$H'_R = \frac{\alpha}{R} \begin{pmatrix} 0 & e^{-i\varphi}\left(-i\frac{\partial}{\partial\varphi}\right) \\ e^{i\varphi}\left(-i\frac{\partial}{\partial\varphi}\right) & 0 \end{pmatrix}. \tag{2.27}$$

We introduce two different probe functions $\Phi(\varphi)$ and $\Psi(\varphi)$

$$\Phi(\varphi) = \begin{pmatrix} \Phi_1 \\ \Phi_2 \end{pmatrix}, \quad \Psi(\varphi) = \begin{pmatrix} \Psi_1 \\ \Psi_2 \end{pmatrix}, \tag{2.28}$$

which are defined in the interval (φ_1, φ_2) (arc geometry) or $(0, 2\pi)$ (ring geometry) so, that $\Phi(\varphi_{1,2}) = \Psi(\varphi_{1,2}) = 0$ (arc geometry) or $\Phi(0) = \Phi(2\pi)$, $\Psi(0) = \Psi(2\pi)$ (ring geometry). Then, we calculate the matrix elements

$$\int d\varphi\, \Phi^*(\varphi)\left[H'_R \Psi(\varphi)\right] = \int d\varphi\left\{ \Phi_1^*\left[e^{-i\varphi}\left(-i\frac{\partial}{\partial\varphi}\right)\Psi_2\right] + \Phi_2^*\left[e^{i\varphi}\left(-i\frac{\partial}{\partial\varphi}\right)\Psi_1\right] \right\}. \tag{2.29}$$

The following equalities can be derived straightforwardly,

$$\int d\varphi\, \Phi_1^* e^{-i\varphi}\left(-i\frac{\partial}{\partial\varphi}\right)\Psi_2 = \int d\varphi\, \Psi_2\left(-ie^{i\varphi}\frac{\partial}{\partial\varphi}\Phi_1 + \Phi_1 e^{i\varphi}\right)^*,$$

$$\int d\varphi\, \Phi_2^* e^{i\varphi}\left(-i\frac{\partial}{\partial\varphi}\right)\Psi_1 = \int d\varphi\, \Psi_1\left(-ie^{-i\varphi}\frac{\partial}{\partial\varphi}\Phi_2 - \Phi_2 e^{-i\varphi}\right)^*. \tag{2.30}$$

Substituting (2.30) into (2.29) we find, that

$$\int d\varphi\, \Phi^*(\varphi)\left[H'_R \Psi(\varphi)\right] \neq \int d\varphi\, \Psi(\varphi)\left[H'_R \Phi(\varphi)\right]^*. \tag{2.31}$$

The inequality (2.31) shows that, in general, the operator H'_R is not Hermitian. Note, that performing the same verification procedure for the initial operator (2.26) we conclude that H_R as a whole is (of course) Hermitian (because of the term $\partial/\partial r$). However, if r is set to a constant R then all terms proportional to derivatives with respect to r do not give a contribution, and (2.26) becomes non-Hermitian, which results in an imaginary energy spectrum at low energies [13].

There are a couple of methods how to deal with (2.26) in order to get its correct 1D form in polar coordinates. The first one is very direct [14]. Let us add a potential $V(r)$ to this Hamiltonian (2.26), which forces the electron wave functions to be localized on the arc (ring) in the radial direction. Specifically $V(r)$ is small in a narrow region around $r = R$ and large outside this region. For a narrow arc (ring) the confining energy in the radial direction is much larger than the spin-orbit coupling energy and the kinetic energy in the azimuthal direction. This allows us to solve the Hamiltonian for the radial wave function first and treat H_R (as well as kinetic term) as a perturbation. However, in order to obtain the 1D Hamiltonian explicitly, we have to calculate the lowest radial mode for a given confining potential. The authors of [14] assume a harmonic confining potential for $V(r)$ and find that the expectation values of r-dependent terms are

$$\left\langle R_0(r)\left|\frac{1}{r}\right|R_0(r)\right\rangle = \frac{1}{R}, \tag{2.32}$$

and, most surprisingly,

$$\left\langle R_0(r) \left| \frac{\partial}{\partial r} \right| R_0(r) \right\rangle = -\frac{1}{2R}. \tag{2.33}$$

Here $|R_0(r)\rangle$ is the r-dependent part of the normalized solution for the lowest radial mode. The relation (2.33) shows, that we cannot safely disregard the $\partial/\partial r$ term in order to obtain the correct Hamiltonian for curved 1D systems with spin-orbit interactions.

Of course, it is not essential to choose a very harmonic potential. To show this, the authors of [14] give the following general reasonings. Let $|R_0(r)\rangle$ be the lowest radial mode for an *arbitrary* confining potential. Now, let us find the expectation value of the operator $\partial/\partial r + 1/2r$ that reads

$$\left\langle R_0(r) \left| \frac{\partial}{\partial r} + \frac{1}{2r} \right| R_0(r) \right\rangle = \left\langle R_0'(r) \left| \frac{1}{r} \frac{\partial}{\partial r} \right| R_0'(r) \right\rangle, \tag{2.34}$$

where $|R_0'(r)\rangle = \sqrt{r}\,|R_0(r)\rangle$. From direct calculations it follows that

$$\left\langle R_0'(r) \left| \frac{1}{r} \frac{\partial}{\partial r} \right| R_0'(r) \right\rangle = \left. \frac{R_0'^2(r)}{2} \right|_0^\infty = \left. \frac{r R_0^2(r)}{2} \right|_0^\infty = 0.$$

We then obtain

$$\left\langle R_0(r) \left| \frac{\partial}{\partial r} \right| R_0(r) \right\rangle = -\left\langle R_0(r) \left| \frac{1}{2r} \right| R_0(r) \right\rangle = -\frac{1}{2R}. \tag{2.35}$$

The term (2.35) is neglected if we follow the conventional procedure. It is only recovered by the projection of the original Rashba operator (2.26) defined on the Hilbert space of spinors in two dimensions on a restricted Hilbert subspace, spanned by the complete set of the spinors, which are functions of the φ coordinate only. In the simple cases mentioned earlier (e. g., free electrons), there are no terms present in the Hamiltonian proportional to both $\partial/\partial r$ and some function of φ (i. e. the two-dimensional Hamiltonian is separable). In these cases the conventional procedure produces the correct result. In all other cases it is necessary to take into account properly the confinement of the wave function in the radial direction as it has been shown above.

Having established the generality of relation (2.35), we can now write down the Rashba operator for the 1D arc (or ring) explicitly in the form

$$H_R^{\mathrm{arc}} = \begin{pmatrix} 0 & \frac{\alpha}{R} e^{-i\varphi} \left(\hat{q}_\varphi - \frac{1}{2} \right) \\ \frac{\alpha}{R} e^{i\varphi} \left(\hat{q}_\varphi + \frac{1}{2} \right) & 0 \end{pmatrix}, \tag{2.36}$$

where $\hat{q}_\varphi = -i\frac{\partial}{\partial \varphi}$ is the angular momentum operator. This is the the Rashba operator for electrons in a 1D arc (or ring) that we shall use throughout the thesis.

It is interesting to note that the Rashba operator in such a geometry is not symmetric. (In contrast to (2.21), $H_{SO}^{12} \neq -H_{SO}^{21}$ here.) This property of the operator (2.36) leads to a certain asymmetry of the electron eigen states in 1D arcs (or in 1D rings as well) in the presence of spin-orbit coupling.
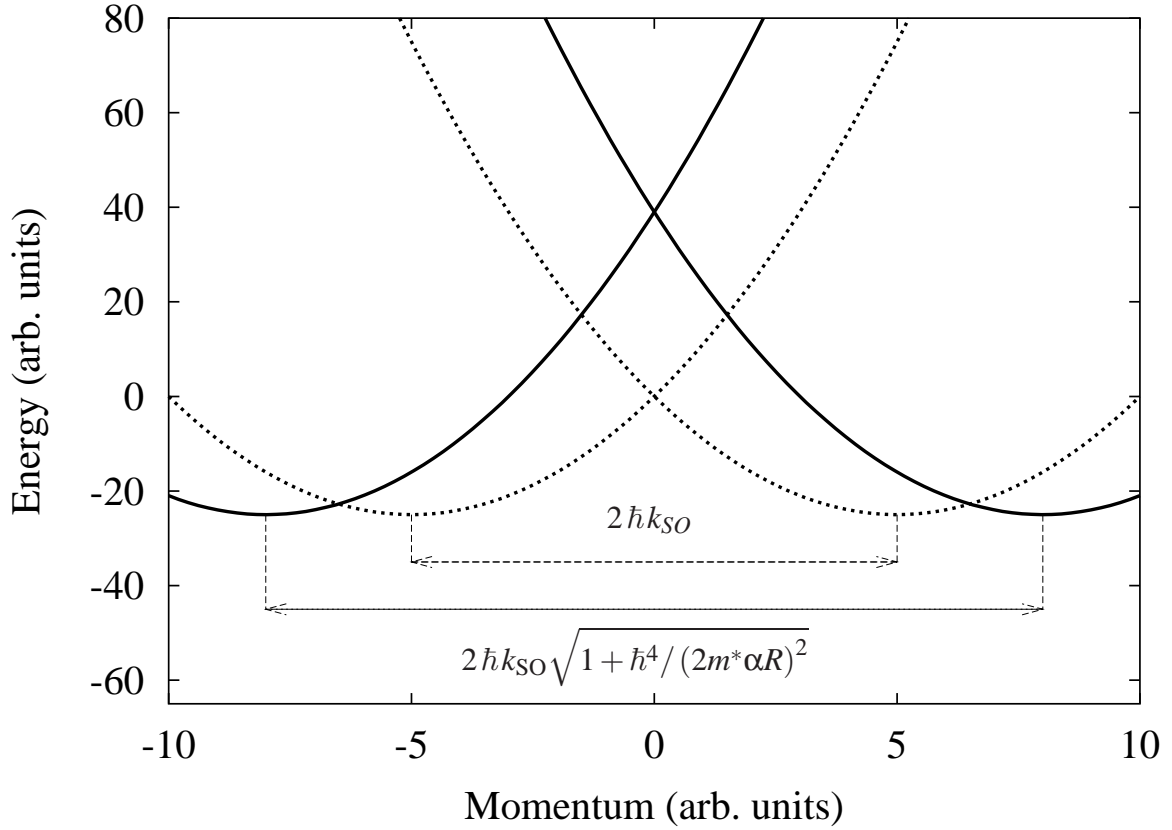
Figure 2.4: The solid line is the typical dispersion law for *curved* 1D wires (R is the radius of curvature) with Rashba spin-orbit coupling. The dashed line corresponds to the case of $R \to \infty$, i. e. the curved wire goes towards a line. One can see, that the finite radius of the wire increases the spin-splitting along momentum axis and, as a consequence, changes the Fermi momenta. The Fermi velocities, however, remain constant.

Indeed, the eigenfunctions of the Hamiltonian $H^{\text{arc}} = H^{\text{arc}}_{\text{kin}} + H^{\text{arc}}_R$, where $H^{\text{arc}}_{\text{kin}} = \hbar^2 \hat{q}^2_\varphi/(2mR^2)$, read

$$\Psi^+_{\text{arc}}(\varphi) = \begin{pmatrix} \cos\gamma \left[C^+_1 e^{i(q^+ - \frac{1}{2})\varphi} + C^+_2 e^{-i(\frac{1}{2} + q^+)\varphi} \right] \\ \sin\gamma \left[C^+_1 e^{i(\frac{1}{2} + q^+)\varphi} + C^+_2 e^{-i(q^+ - \frac{1}{2})\varphi} \right] \end{pmatrix},$$

$$\Psi^-_{\text{arc}}(\varphi) = \begin{pmatrix} \sin\gamma \left[C^-_1 e^{i(q^- - \frac{1}{2})\varphi} + C^-_2 e^{-i(\frac{1}{2} + q^-)\varphi} \right] \\ \cos\gamma \left[C^-_1 e^{i(\frac{1}{2} + q^-)\varphi} + C^-_2 e^{-i(q^- - \frac{1}{2})\varphi} \right] \end{pmatrix}, \tag{2.37}$$

where

$$\tan\gamma = \frac{\varepsilon_0 R}{\alpha} + \sqrt{1 + \left(\frac{\varepsilon_0 R}{\alpha} \right)^2}, \tag{2.38}$$

$\varepsilon_0 = \hbar^2/(2mR^2)$ is the confinement energy, and $q^\pm$ have to satisfy the following dispersion rela-

17

tions

$$E_q^{\pm} = \frac{\varepsilon_0}{4} + \varepsilon_0 q^2 \pm q\sqrt{\left(\frac{\alpha}{R}\right)^2 + \varepsilon_0^2}. \tag{2.39}$$

Similar to (2.23), the equation (2.39) has two solutions with respect to q corresponding to the left- and right-moving particles for a given spin index "+" or "−". In contrast to (2.22), the spinors (2.37) are not symmetric in the sense that their two components have different weights: $\cos\gamma$ and $\sin\gamma$. These weights depend on the arc (ring) radius R so, that in the limit of $R \to 0$ the difference between them is maximal ($\gamma = \pi/2$). Of course, in the opposite limit $R \to \infty$ we arrive at the symmetric solution (2.22).

The effect of the finite radius on the dispersion law (2.39) is shown in fig. 2.4. One can easily see, that the change of arc radius shifts the dispersion curves along the momenta axis, while the tuning of the Rashba constant α (by using external electric fields) shifts them along *both* momentum and energy axes. The bending of 1D wires with spin-orbit coupling demonstrates, therefore, an intriguing effect: the spin-splitting increases, while the Fermi velocities remain constant. As it will be shown in the present thesis, this interesting feature can be used in *reflectionless* spin-switch (see Chapter 4). One can find a review of previous papers related to this topic in the present Chapter, section 5.

The system discussed above becomes even more interesting if we place the curved 1D wire in the magnetic field perpendicular to its plane. In particular, this makes it possible to find the manifestation of spin-orbit Berry's phase in a quantum loop (see the next section for a review or the next Chapter for our results). Moreover, the coupling between Rashba and Zeeman effects in a curved 1D wire (in a straight 1D wire this feature does not occur!) produces a deformation of the dispersion curves in such a way, that the Fermi velocities for left- and right- moving electrons become unequal. The chiral densities of states are, therefore, not equal as well. Thus, such a system gives us at least the theoretical possibility to distinguish somehow the chiral states. (Here, "left" is not equal to "right" in a certain sense.) The question is, however, how stable this effect is. What happens if, for example, the electron-electron interactions are switched on? The answer will be given in the framework of a Tomonaga-Luttinger liquid description in Chapter 5 of this thesis. For an introduction to the Tomonaga-Luttinger model see sections 6 and 7 of the present Chapter.

2.4 Introduction to the spin-orbit Berry phase

The beauty of the topological Berry phase concept [15] inspires much theoretical and experimental activity aimed at finding its manifestations in different areas of modern physics [16]. Berry describes a quantal system in an eigenstate, slowly transported around a circuit by varying a parameter λ in its Hamiltonian so, that

$$\lambda_{\text{initial}} = \lambda_{\text{final}} = \lambda_0,$$

and

$$H(\lambda_0) = H(\lambda_{\text{initial}}) \to H(\lambda_1) \to H(\lambda_2) \to \dots \to H(\lambda_n) \to H(\lambda_{\text{final}}) = H(\lambda_0).$$

According to the adiabatic theorem, if the Hamiltonian is returned to its original form, the system will return to its original state, apart from a phase factor

$$\Psi(\lambda_0) \rightarrow e^{i(\phi_B + \phi_D)} \Psi(\lambda_0).$$

In addition to the familiar dynamical phase ϕ_D, such a state can acquire a geometrical, circuit-dependent phase factor ϕ_B, which is the result of the adiabatic variation of the external parameters. This phase ϕ_B is known as Berry's phase. (See also a fundamental generalization of this idea for non-adiabatic evolution [17].)

A possible candidate for the role of such a parameter λ in solid state physics is the external magnetic field **B** that interacts with the electron spin via the Zeeman effect. This interaction is described by the following Hamiltonian

$$H_Z = \frac{g\mu_B}{2} \sigma \cdot \mathbf{B}, \tag{2.40}$$

where $\sigma = \{\sigma_x, \sigma_y, \sigma_z\}$ are the Pauli matrices (2.6), and μ_B, g are Bohr magneton and g-factor respectively. When the value of the magnetic field is constant and its direction follows adiabatically a closed trajectory, the spin wave function acquires the topological phase factor ϕ_B which is proportional to the solid angle subtended in a space by the magnetic field [15].

The possibility to control the Berry phase by means of the Zeeman effect is the central issue explored in the pioneering [12, 18, 19] and recent [20, 21, 22, 23, 24, 25, 26] papers. In particular, the authors consider the adiabatic as well as non-adiabatic motion of electrons through a mesoscopic ring in the presence of a static, inhomogeneous magnetic field. It is shown that the Berry phase, accumulated by the spins of electrons encircling the ring, leads to persistent equilibrium charge and spin currents [12, 18] or affects the conductance of the ring [19, 21, 25] in a way similar to the Aharonov-Bohm effect [27].

The latter point is of particular interest to the topic. Indeed, since Aharonov-Bohm and Berry phases can be varied individually, the interplay of the two phases yields a rich variety of behavior. In particular, the amplitudes of the Aharonov-Bohm oscillations are strongly affected by the Berry phase [21]. Moreover, the authors of [21] show that these amplitudes can be completely suppressed at certain magic tilt angles of the external fields.

As was noted above, in order to observe the geometric phase in an electronic system with spin, the application of an orientationally inhomogeneous (e. g. radial) magnetic field is necessary. However, the manner in which the magnetic field is varied in [12, 18, 19, 20, 21, 22, 23, 24, 25, 26] leads to rather difficult experiments. Fortunately, the desired magnetic field texture can be experimentally implemented via fabricating the loop (or ring) from a material with spin-orbit interactions of Rashba type (2.19). Indeed, the Rashba operator for 1D rings (2.36) derived in the previous section can be rewritten in the quasi-classical limit $q \gg 1$ as

$$H_R = \frac{\alpha}{R} \left(\sigma_x \cos\varphi + \sigma_y \sin\varphi \right) \hat{q}_\varphi. \tag{2.41}$$

At the same time, in the presence of a radial in-plane magnetic field B_{in} the Zeeman term (2.40) can be rewritten in polar coordinates as

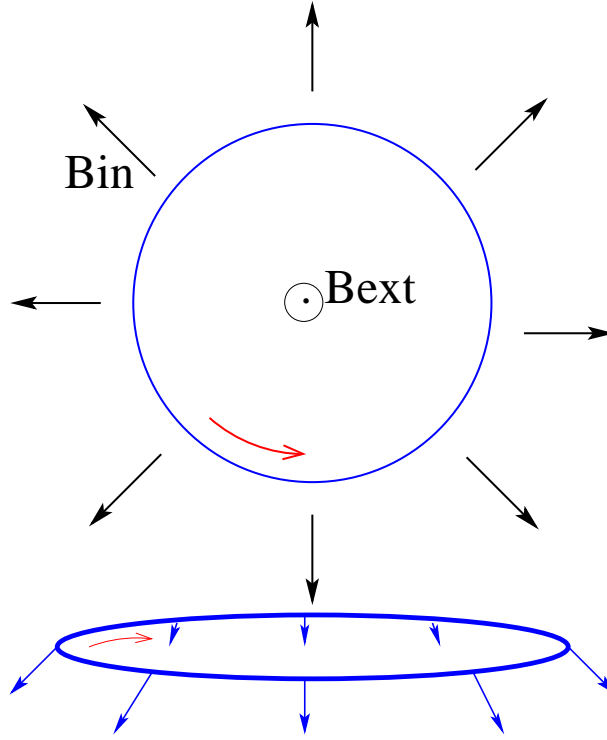$$H_Z = \frac{g\mu_B}{2} \left(\sigma_x \cos\varphi + \sigma_y \sin\varphi \right) B_{in}. \tag{2.42}$$

Figure 2.5: The in-plane radial effective magnetic field B_{in} (which stems from the Rashba effect) and the real external one B_{ext} form in the ring the effective magnetic field crown-like texture which is shown in the lower part of the figure. The total magnetic field changes its direction adiabatically while an electron moves in a circle, and, therefore, the electron wave function acquires a geometrical phase.

Now, the effect of Rashba spin-orbit coupling on the electron motion in the ring is seen clearly by comparing eq. (2.41) and (2.42): namely, the electrons in such a ring experience a radial built-in Zeeman-like magnetic field

$$B_{\text{in}} = \frac{2\alpha q}{g\mu_B R},\tag{2.43}$$

here q is the characteristic angular wave vector. In other words, the Rashba effect in the quasiclassical limit represents the effective Zeeman-like magnetic field B_{in}. It is important to emphasize, that this in-plane magnetic field *does not* relate to the real external magnetic field B_{ext}, but stems from the internal properties of the substance (spin-orbit interactions). Most important, however, the external B_{ext} and in-plane B_{in} components form the desired inhomogeneous magnetic field texture shown in fig. 2.5 and in that way can provide the geometric phase indications through interference patterns in the conductance of the ring. This pretty idea is attracting both theoretical [13, 28, 29, 30, 31] and experimental [32, 33, 34, 35, 36] attention. In what follows, we review the problems and advantages of spin-orbit Berry's phase manifestations in low-dimensional systems.

Let us consider the geometric phase that the wave function of a charged *and* spin-full particle

acquires as it travels around the ring structure with Rashba spin-orbit coupling (2.41). The system is placed in the external magnetic field B_{ext}, which is perpendicular to the ring plane (see the magnetic field configuration in fig. 2.5). Firstly, since the particle carries a charge, it picks up an Aharonov-Bohm phase [27]

$$\phi_{\text{AB}} = 2\pi \frac{\Phi}{\Phi_0}, \tag{2.44}$$

where Φ_0 is the flux quantum, and $\Phi = \pi R^2 B_{\text{ext}}$ is the magnetic flux enclosed by the ring. Secondly, if the particle carries a spin of $1/2$ and its motion is adiabatic, then the spin geometric phase, according to Berry's definition [15], reads

$$\phi_B = \pi \left(1 - \frac{B_{\text{ext}}}{\sqrt{B_{\text{ext}}^2 + B_{\text{in}}^2}} \right), \tag{2.45}$$

and the full geometric phase is a sum of both $\phi = \phi_B + \phi_{\text{AB}}$. Note that the adiabaticity requires comparatively large values of B_{in} and B_{ext} so that the electron spin precesses few times within a cycle.

In [13], the authors established a one-particle Hamiltonian for electrons moving on a 1D ring in the presence of Rashba spin-orbit coupling and Zeeman splitting. Furthermore, the ballistic motion of electrons in the absence of scattering and spin-flip processes has been studied. In the spirit of the seminal papers by Büttiker, Landauer, Imry, Azbel and Pinhas [37, 38, 39], the transmission amplitude of the ring has been derived and the conductance oscillations have been investigated. We should note, however, that authors of [13] used a non-Hermitian operator (2.27) in the Hamiltonian. Zhou, Li, and Xue [28] noticed this fact and derived a different (Hermitian) Hamiltonian operator. However, in their Hamiltonian the spin-orbit coupling originates from an electric field pointing in the radial direction and not in the direction perpendicular to the plane of the ring. This is not the correct Rashba term for inversion layers [5]. The procedure for obtaining the correct Hamiltonian has been described in [14] as well as in the previous section of this Chapter.

In spite of the mentioned shortcoming, [13] has been the stimulus for the subsequent studies. In particular, topological transitions in the ring conductance interference pattern subject to Berry's phase have been studied in [29]. It manifests itself in a steplike conductance-magnetic field and conductance-gate voltage characteristics. The transition takes place when the Berry phase is dropped by an additional static magnetic field B_{ext} from odd of π to zero as it follows from equation (2.45). The non-adiabatic spin-orbit geometric phase (of non-Berry, but Aharonov-Anandan type [17]) in quantum rings has been investigated in [30]. It has been shown that such a phase becomes the spin-orbit Berry phase in the adiabatic limit. In order to analyse the structure of the Aharonov-Bohm oscillations influenced the by spin-orbit Berry phase, the Fourier spectra of conductance has been calculated [31]. Note that the method of Fourier analysis is the only suited one for comparison of the theoretical results with the experimental data discussed below.

In pioneering observations of Berry's phase [32, 33], the Aharonov-Bohm oscillations were studied in InAs two-dimensional two-contact quantum rings with strong spin-orbit interaction. The Fourier transforms of over 30 traces of oscillations were averaged and a small splitting of the
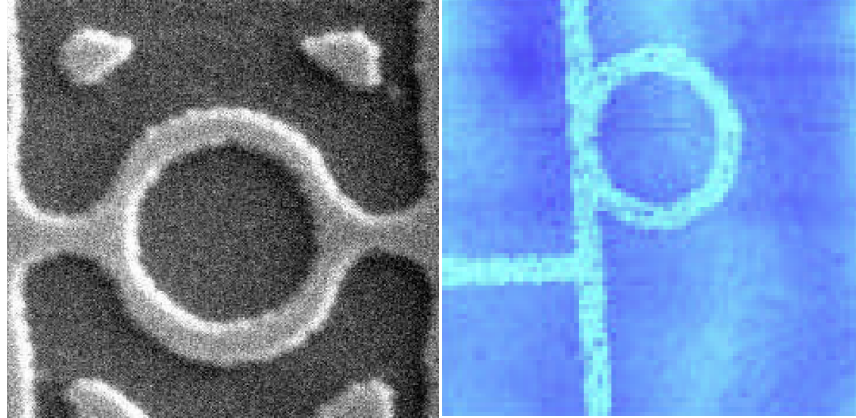
Figure 2.6: AFM images of two-contact (left) and one-contact (right) rings used for Berry's phase observations. The images are taken from the corresponding papers discussed in the text.

main peak in the final Fourier spectrum was interpreted as a possible manifestation of the spin Berry phase. (See [40, 41] for subsequent discussions.)

An attempt has been made to observe Berry's phase in quantum rings fabricated in a GaAs/AlGaAs heterostructure with a 2D hole system [34] (see fig. 2.6, left panel). In such a setup, the inversion asymmetry results from the GaAs zinc blende crystal structure as well as from an electric field, which is perpendicular to the 2D plane. Along with the main peak whose frequency corresponds to the magnetic flux enclosed by the ring, there are some extra peaks in the Fourier spectra of the measured Aharonov-Bohm oscillations. A qualitative comparison of the Fourier transforms with its simple simulation provides a striking demonstration of the Berry phase. (See also subsequent Comments and Replies [42, 43, 44, 45])

In contrast to earlier work, the authors of [35, 36] furnish a novel configuration, in which the ballistic ring forms *one* collimating contact with the tangential current lead (see fig. 2.6, right panel). Beside the absence of unknown asymmetry in the arm length (that always gave an uncertainty in a two-contact configuration) and additional spin rotation at contacts, such a setup allows to let only one transverse mode with a small longitudinal momentum enter the ring through the contact (see fig. 2.7a). In what follows, we provide a description of the momentum-filtering mechanism used in this configuration.

Since the tangential lead is quite narrow the electron motion is strongly quantized in the transversal direction. According to the conductance quantization measurements, there are only four subbands occupied (Zeeman spin-splitting included). Let $p_F = \hbar k_F$ be a characteristic value of the Fermi longitudinal momentum in the upper subband. Note, that the upper subbands have smaller Fermi longitudinal momenta than the lower ones. The corresponding Fermi velocity and Fermi vector are v_F, k_F respectively, and the latter can be estimated via geometrical parameters of the contact. Let l, d be the contact length and width respectively (see fig. 2.7b) and $\delta x_\perp$ is the transverse shift of an electron while it moves through the lead in the contact region. On one hand, if the electron is going to enter the ring then the inequality $\delta x_\perp \geq d$ should be satisfied. On the other
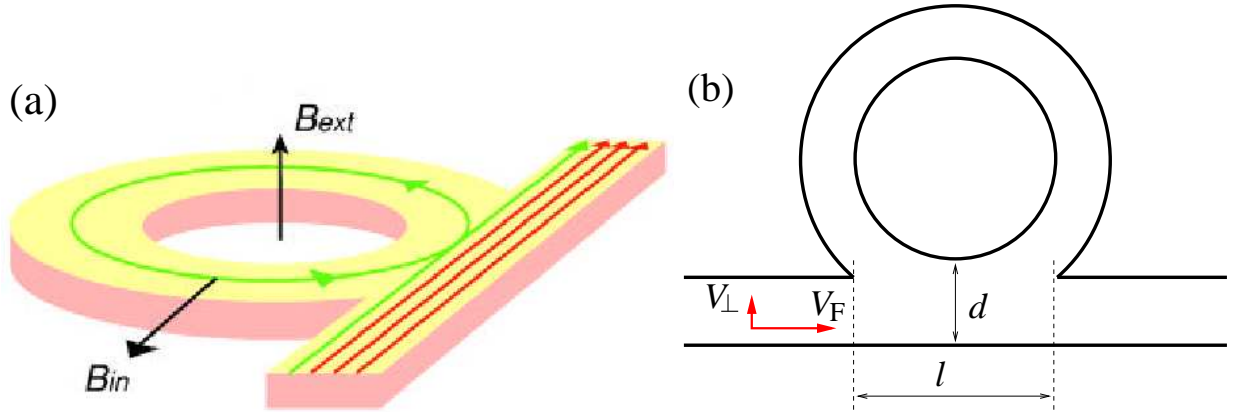
Figure 2.7: (a) Trajectories of electrons in the one-collimating-contact ring. The green curve corresponds to the trajectory of electrons from the upper mode in the tangential lead, while the red ones are related to the lower modes with comparatively large tangential Fermi momenta. This picture is taken from [36]. (b) Geometrical parameters of the one-collimating-contact ring used in text.

hand, the shift $\delta x_\perp$ is nothing else than the transverse component of the trajectory that was acquired by the electron with velocity $v_\perp = p_\perp/m$ (here m is the *effective* electron mass) during the period of time $\tau = l/v_F$ of its passage through the contact region so, that $\delta x_\perp = (p_\perp/m)(l/v_F)$. The transverse component of the electron's momentum $p_\perp$ can be estimated from the uncertainty relation $p_\perp \approx \hbar/d$. Thus, if we want only a single (upper) mode to enter the ring then the electron Fermi vector $k_F = mv_F/\hbar$ of that mode should be as small as $k_F \leq l/d^2$. The lower modes are much faster so, that $k_F^{\text{lower}} > l/d^2$. As a result of such momentum filtering by the contact, the interference pattern in the conductance is determined solely by *a single* transverse mode. It is therefore possible to apply a 1D model for emulation of the ballistic electron transport through such a system.

There are, however, some parameters related to one-collimating-contact rings that look rather problematic. For instance, the estimated wave vector k_F is as small as $7.5 \times 10^6 \text{m}^{-1}$ which makes the electron motion very sensitive to the potential landscape. The samples must, therefore, be perfectly clean. Nevertheless, the authors of [35, 36] have managed somehow to solve the problems, and the observed beating in the Aharonov-Bohm conductance oscillations was interpreted as conclusive evidence of the spin-orbit Berry phase in the conductance of quantum rings.

In this thesis we study theoretically a system similar to [35, 36]. The distinct feature between our model and the real device in [35, 36] is as follows. We describe a purely 1D case, and, therefore, we do not take into account the electrons which bypass the ring (red trajectories in fig. 2.7a). In other words, our system is rather a quantum *loop* than a quantum ring. The detailed description and solution of the model as well as the discussion of its possible applications is given in the Chapter 4.
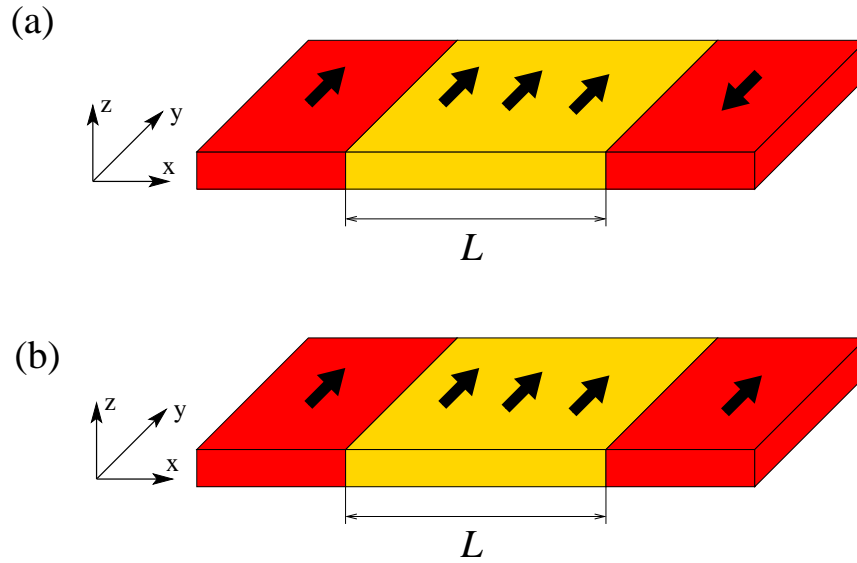
Figure 2.8: Schematics of the spin-valve device. Red regions are ferromagnetics that serve as a polariser and analyser of the electron spin. The yellow region in between is the ballistic semiconductor (e. g. p-InAs) with spin-orbit coupling. The spins are injected in their eigen states in the semiconductor element, therefore, they keep constant orientation. We can open (a) or close (b) the spin-valve by switching the polarization in one of the ferromagnetic contacts.

2.5 Introduction to spin manipulation

In the past few years the idea to use electron spin in mesoscopic devices has generated a lot of interest. In [46], Datta and Das describe how Rashba spin-orbit coupling can be used to modulate the current. The underlying idea is to drive a modulated spin-polarized current entirely electrically, combining just ferromagnetic metals and semiconductor materials. One of the simplest solutions is the spin-valve setup (see fig. 2.8) where the output current is governed by switching of the spin-polarization in one of the ferromagnetic contacts. The second possibility is the so-called spin field effect transistor (see fig. 2.9). Here, the spin-polarized current is injected from a ferromagnetic material into the region with Rashba spin-orbit coupling (formed at a semiconductor heterojunction) and then collected by the second ferromagnetic material. In basic terms, the idea is that the Rashba effect will induce a spin precession of the electrons moving parallel to the interface, rotating them with respect to the magnetization direction of the second ferromagnet (collector). Then by adding a gate voltage the net effective electric field (and hence, the spin-orbit interaction) at the interface can be modified, tuning the spin precession, and therefore, the transmitted spin-polarized current is modulated accordingly.

The problem of the spin-filtering contacts is still attracting both experimental [47, 48, 49, 50] and theoretical [51, 52, 53, 54, 55, 56, 57, 58, 59, 60] attention. The conventional approach [46] employs contacts made of a ferromagnetic material like iron. At the Fermi level in such materials the density of states for electrons with one spin greatly exceeds that for the other spin direction, so
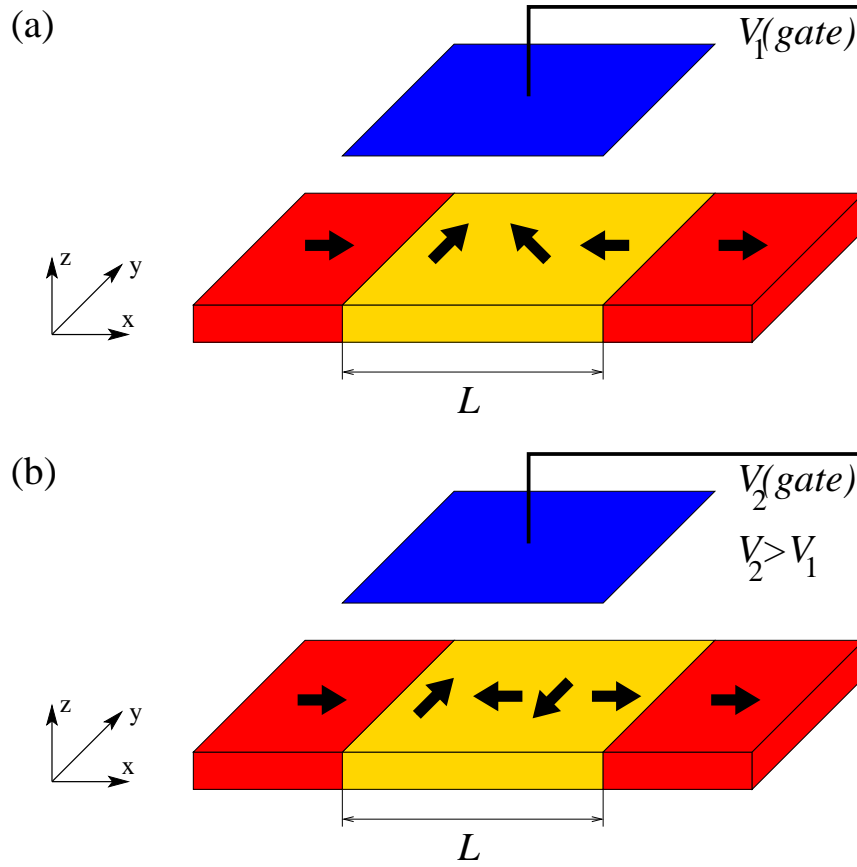
Figure 2.9: Schematics of the Datta-Das spin-modulator device (spin field effect transistor). The blue plate is the metallic gate which allows to tune the Rashba coupling strength. In contrast to spin-valve geometry, the spins injected are *not* in their eigen states in the semiconductor region, but in a linear combination of them (the initial polarization is along *x* axis). Therefore, the spin rotation governed by the Rashba coupling strength occurs while the electrons flow through the semiconductor. Changing the gate voltage, we are able to tune the speed of spin rotation and in that way to control the output current: (a) device is closed (b) device is opened.

that the contact preferentially injects and detects electrons with a particular spin. In the seminal paper [46] there was a brief discussion about whether such a spin polariser (as well as an analyser) can be well implemented in a two-dimensional electron gas. Although great progress has been achieved in theoretical understanding [53, 57, 59] and experimental realization [47, 48] of the magnetized contacts, fabrication of these structures can pose further material-science challenges and may require rather complicated chip design. Achieving spin filtering and spin manipulation by means of intrinsic spin-dependent effects in semiconductors is, therefore, highly desirable.

One of the treatments is to use optical excitations from spin-split hole subbands in asymmetric quantum wells. In [49, 61], a non-equilibrium population of spin-up and spin-down states in quantum well structures has been experimentally established applying circularly polarized radi-

ation. The spin polarization results in a directed motion of free carriers in the plane of a quantum well perpendicular to the direction of light propagation. Because of the spin selection rules, the direction of the current is determined by the helicity of the light and can be reversed by switching the helicity from right to left handed. In [55], Mal'shukov and Chao show theoretically that spin polarization can be created in the well by radiative electron-hole recombination.

The literature concerning spin filtering using intrinsic spin-orbit interactions suggests many solutions of the problem [51, 52, 54, 56, 58, 62, 60]. (Note, that in contrast to the spin-orbit splitting, use of the Zeeman splitting is not the most practical way to achieve spin polarization, as needed magnetic field strengths are often large [63] and on-chip placement of micromagnets is required.)

In [52], Kiselev and Kim have published very impressive results based on the Rashba effect. Their structure consists of a T-shaped quasi-one-dimensional channel and an electrode placed near the channel intersection to control the spin-orbit interaction of electrons. The calculations demonstrate that the proposed device can redirect electrons with opposite spins from an unpolarized source to left and right output leads, respectively, and, thus, serve as a spin filter. The stronger spin-orbit coupling improves the spin-polarization efficiency [64]. Depending on parameters of the system, the polarization approaches nearly 100%.

There are further examples. The spin-dependent electron resonant tunneling through non-magnetic asymmetric *double* barriers is studied theoretically in [51]. It is shown, that an unpolarized beam of conduction band electrons can be strongly polarized, at zero magnetic field, by spin-dependent resonant tunneling, due to the Rashba spin-orbit interaction. The spin-dependent resonant tunneling is also used in [54]. The authors propose an electronic spin-filter device that consists of a non-magnetic *triple* barrier and combines the spin-split resonant tunneling levels induced by the Rashba spin-orbit interaction and the spin blockade phenomena between two regions separated by the middle barrier in the structure. Detailed calculations using the InAlAs/InGaAs material system show, that the filtering efficiency exceeds 90% at the peak positions.

A lateral interface connecting two regions with different strengths of the Rashba spin-orbit interaction can also be used as a spin polarizer of electrons in two-dimensional semiconductor heterostructures [60, 62]. A beam with a nonzero angle of incidence is split after transmission into two spin polarized components propagating at different angles. In contrast to [62], the case when one of the two regions is ballistic, while the other one is diffusive, is the central issue explored in the recent paper [60]. The technique developed for the solution of the problem of diffuse emission [65] is generalized to the case of spin-dependent scattering at the interface and the distribution of electrons emitted from the diffusive region is determined. It has been shown that the emission in the diffusive regime is an effective way to get electrons propagating at small angles to the interface that are most appropriate for the spin filtration and a subsequent spin manipulation.

Another original device proposed in [56] to achieve spin filtering without using ferromagnets is based on the interplay of the Rashba effect and the wave-number selectivity due to the momentum-resolved tunneling between two parallel electron wave guides (one-dimensional quantum wires, fig. 2.10). One of the wires has intrinsic coupling of electron spin to its momentum, while in the other wave guide spin-orbit interactions are assumed to be absent (see fig. 2.11). Due to the wave-number selectivity, tunneling can only occur for electron states with wave numbers close
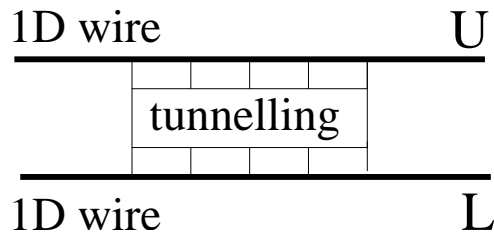
Figure 2.10: Schematic picture of the spin-filtering device proposed by Governale et al.[56]: two parallel 1D quantum wires, labelled "U" and "L", are each connected to separated reservoirs. The upper wire has intrinsic coupling of electron spin to its momentum, while in the lower one the spin-orbit interactions are assumed to be absent. The wires are coupled via tunneling through an extended uniform barrier.

to the point where the dispersion curves of two wires cross so that the conservation of energy and momentum is fulfilled. Because of the Rashba effect, dispersion curves for spin-up and spin-down electrons in one of the wires are split along the momentum axis. Thus, the momentum resolved tunneling current is always spin-polarized. Such current can be created by applying
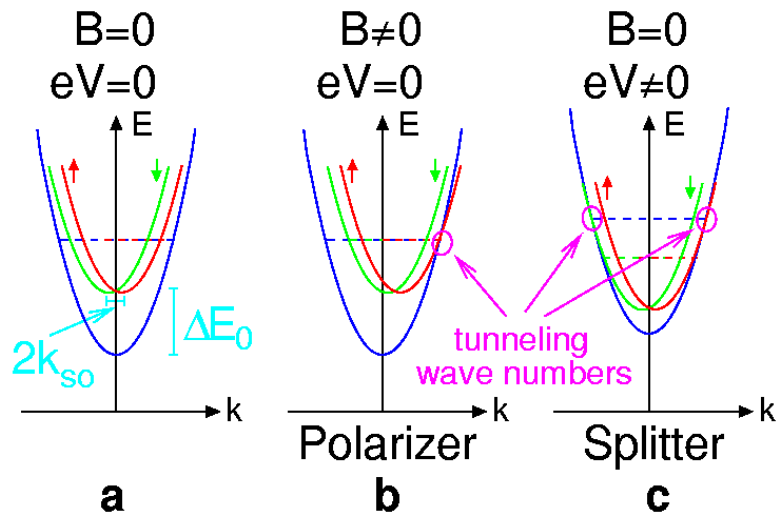

Figure 2.11: Illustration of device operation depicted in fig. 2.10 as spin polarizer or spin splitter (a) Due to the Rashba effect, dispersion curves for spin-up and spin-down electrons in the upper wire are shifted horizontally by $2k_{SO}$ (see eq. 2.24). In the lower wire, where spin-orbit coupling is assumed to be absent, energy dispersion curves are spin degenerate. (b) Tuning wavenumber selectivity by a magnetic field B, tunneling is selectively enabled for right-moving electrons with spin up. (c) At a certain value of voltage V, tunneling becomes possible for left-moving spin-down electrons and right-moving spin-up electrons. Note that parabolicity of electron bands is not essential to achieve coincidences and, hence, spin-polarized currents. This figure is taken from cond-mat/0105066.
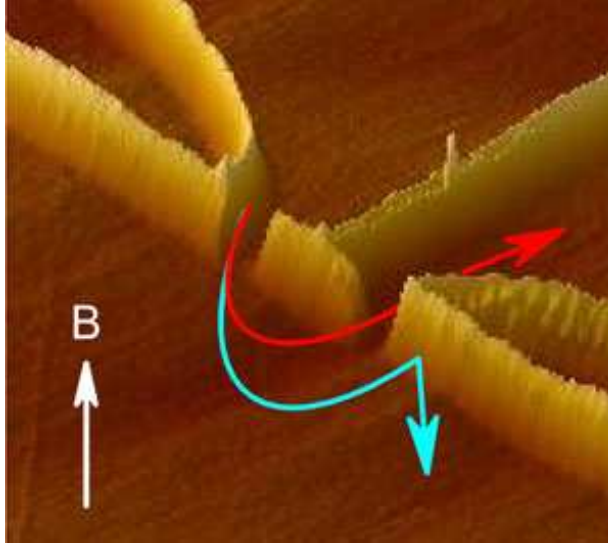
Figure 2.12: AFM micrograph of a sample (5μm $\times$ 5μm) showing two point contacts. Light lines are the oxide which separates different regions of a 2D hole gas. Conductance of the quantum point contacts is controlled via voltages applied to the detector, injector and the central gates. Semicircles show schematically the trajectories for two spin orientations. The red one corresponds to the spin-split branch (see fig. 2.3) with lower momenta. The image is taken from [50].

voltages (shifting of the energy band bottom) or small magnetic fields (momentum shifting). It looks so, that switching between opposite spin polarizations is easily achieved.

The fact that due to the strong spin-orbit interaction the particles at the Fermi energy have different momenta for two possible spin states traveling in the same direction (and, correspondingly, different cyclotron orbits) is also utilized in [50]. In that experimental work, two point contacts designed on *GaAs* and a narrow detector arranged in the magnetic focusing geometry are demonstrated to work as a tunable spin filter (see fig. 2.12). Note, that the phenomenon is not restricted to holes in *GaAs* but is generic to any system with intrinsic spin-orbit interactions (e. g. InSb [66]).

The investigation presented in this thesis also focuses on the spin manipulation using intrinsic spin-orbit interactions. We show in Chapter 4, that the specific geometry of ballistic 1D quantum channels with Rashba spin-orbit coupling can change the initial spin-polarization of the current and serve as an effective spin-switch.

2.6 Introduction to the Tomonaga-Luttinger liquid

A Tomonaga-Luttinger liquid is the analytically solvable model for interacting fermions in one dimension. The key point of this approach is the so-called *bosonization*: a technique for representing one-dimensional fermion fields $\psi_\eta(x)$, where η is a species (e.g. spin or chirality) index,
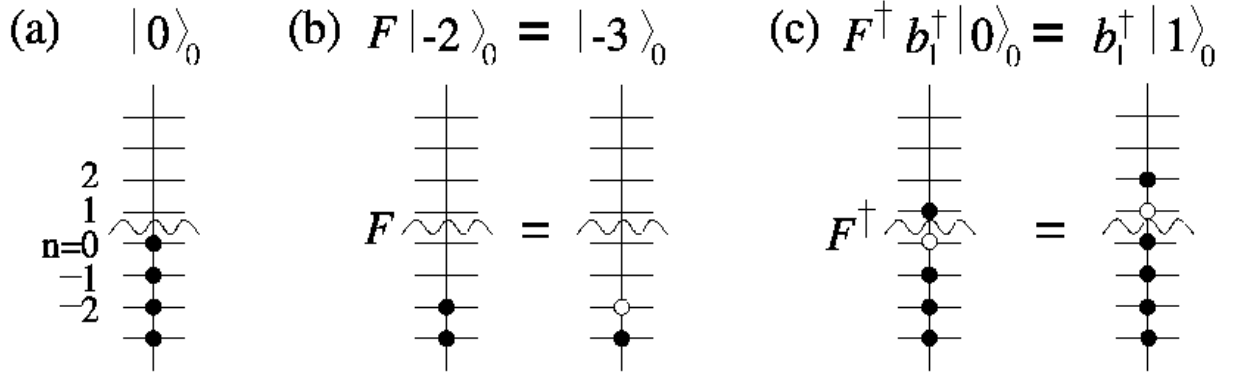
Figure 2.13: (a) The vacuum state $\left|\vec{0}\right\rangle_0$; (b) the action of the Klein factor F on a (-2)-particle ground state $|-2\rangle_0$, which yields $|-3\rangle_0$; (c) the action of the Klein factor $F^\dagger$ on the 0-particle excited state $b_1^\dagger|0\rangle_0 = ic_1^\dagger c_0|0\rangle_0$ (one boson is one particle-hole excitation), which yields $b_1^\dagger|1\rangle_0$. The wavy lines indicate the Fermi level. These figures are taken from [67].

in terms of bosonic fields $\phi_\eta(x)$ through a relation of the form

$$\psi_\eta(x) = F_\eta a^{-1/2} e^{-\frac{2\pi i x}{L}\left(\hat{N}_\eta - \frac{1}{2}\delta_b\right)} e^{-i\phi_\eta(x)}. \tag{2.46}$$

Here L is the wire length, $a > 0$ is an infinitesimal regularization parameters needed to regularize ultraviolet divergent momentum sums, and δ_b is the parameter determined by boundary conditions for the fermion fields $\psi_\eta(x)$. The boundary condition leads to the quantization of the fermionic momentum k in the form

$$k = \frac{2\pi}{L}\left(n_k - \frac{1}{2}\delta_b\right), \tag{2.47}$$

where n_k are integers. In the following, we choose (for definiteness) anti-periodic boundary conditions $\psi_\eta(L/2) = -\psi_\eta(-L/2)$. Note, that that the specific choice of boundary condition becomes unimportant in the continuum limit $L \to \infty$.

The operator $\hat{N}_\eta$ counts the number of η-electrons relative to the so-called vacuum state (or Fermi sea) $\left|\vec{0}\right\rangle_0$ defined by such a way, that the highest filled level of $\left|\vec{0}\right\rangle_0$ is labelled by $n_k = 0$ and the lowest empty level by $n_k = 1$ (see fig. 2.13a). Finally, F_η is a Klein factor which lowers the number of η-fermions by one (see fig. 2.13b).

The boson fields $\phi_\eta(x)$ are defined via bosonic creation and annihilation operators $b_{q\eta}^\dagger$ and $b_{q\eta}$

$$\phi_\eta(x) = -\sum_{q>0} \frac{1}{\sqrt{n_q}}\left(e^{-iqx}b_{q\eta} + e^{iqx}b_{q\eta}^\dagger\right)e^{-aq/2}, \tag{2.48}$$

where $q = \frac{2\pi}{L}n_q$ is the *bosonic* momentum, which is, of course, also quantized as soon as boundary conditions are imposed. In our model, bosonic creation and annihilation operators create and

annihilate the particle-hole excitations in the Fermi sea (see fig. 2.13c). The latter is defined as a state that does not contain any particle-hole excitations so, that

$$b_{qn}\left|\vec{N}\right\rangle_0 = 0, \quad \forall \quad q, \eta. \tag{2.49}$$

The particle-hole excitations subject to electron-electron interactions are often called plasmons.

Tomonaga [68] was the first to identify boson-like behavior of certain elementary excitations in a one-dimensional theory of interacting fermions. A precise definition of these bosonic excitations in terms of bare fermions was given by Mattis and Lieb [69], who took the first step towards a correct solution of a model of interacting one-dimensional fermions earlier proposed by Luttinger [70]. A bosonic representation of a fermion field at a single point, essentially of the form $\psi_\eta(x = 0) \sim e^{-i\phi_\eta(x=0)}$, was first introduced by Schotte and Schotte [71] to calculate x-ray edge transition rates. The extension of their relation to arbitrary x was discovered simultaneously by Mattis [72] and by Luther and Peschel [73], which made the systematic calculation of general correlation functions very simple. However, they did not discuss the number-lowering Klein factors F_η. The first completely precise bosonization relation in the solid-state literature (though from a field-theoretical viewpoint) was given by Heidenreich [74]. The first explicit construction of the Klein factors F_η in terms of bare fermionic operators was given by Haldane [75], whose detailed discussion in [76] essentially completed the development of the bosonization formalism.

Originally, the Tomonaga-Luttinger model was treated for spinless fermions. The inclusion of spin still leads to an exactly solvable model [77, 78]. The solution of that model shows, however, drastic differences from the spinless case. It is commonly known, that the spectral function is generally broadened in any interacting system. However, in a Fermi liquid (even if quasiparticle spin is taken into account), the spectral function still exhibits a distinct single-electron-like peak, making it possible to represent the system of interacting electrons as a system of noninteracting quasiparticles that carry the same quantum numbers as free electrons. Such a quasiparticle peak is absent in the spectral function of a spinfull Tomonaga-Luttinger liquid. Instead, a characteristic double-peak structure appears. The existence of the two peaks whose energy dispersions follow those of the elementary charge and spin-density excitations can be interpreted as the dynamical breakup of the electron into two independent entities representing its spin and charge degrees of freedom. This is the most striking feature of a Tomonaga-Luttinger liquid.

All the abovementioned work relates to the simplest case of a 1D interacting electron system without Zeeman splitting and spin-orbit coupling. The most recent publications proceed with further generalizations of the Tomonaga-Luttinger model for 1D wires taking into account Zeeman [79, 80] and Rashba [56, 81, 82] effects. In particular, an interacting spinfull 1D electron gas placed in the magnetic field may be described as a Tomonaga-Luttinger model comprising two components with *different* Fermi velocities due to the Zeeman splitting [80]. This destroys the spin-charge separation mentioned above, and even quantities such as the density-density correlation involve the spins. In [79], the authors demonstrate that the tunneling density of states in a Tomonaga-Luttinger liquid is singular at energies $\pm g^* \mu_B B$, where the effective Lande factor g^* is renormalized by the interaction.

Let us focus on the paper by A. V. Moroz, K. V. Samokhin and C. H. W. Barnes [81] (and its extended version [82]) as closely related to the results presented in Chapter 5 of this thesis. The
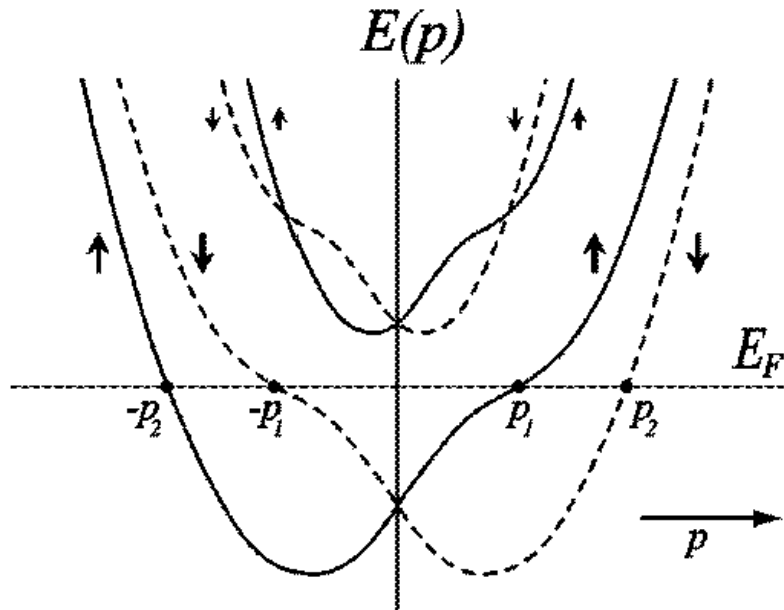
Figure 2.14: Lowest and the first excited spin-split subbands of a quasi 1D quantum wire with strong Rashba spin-orbit coupling. Here, the characteristic spin-orbit interaction energy $\hbar^2 k_{SO}^2/(2m)$ is comparable with interband spacing subject to confinement. Therefore, the dispersion curves are deformed as compared to the ones for "ideal" 1D systems (fig. 2.3). This figure is taken from [82].

authors studied *quasi* one-dimensional wires with Rashba spin-orbit coupling. In such quasi-1D systems (i. e. in the presence of a confining potential) the transverse single-particle wave functions are not plane waves like (2.22). Since the exact analytical solution of the corresponding Schrödinger equation is rather difficult in this case, perturbation theory is usually applied. As a result, along with the horizontal splitting of the spin branches, spin-orbit coupling leads to a deformation of each branch of the single-particle dispersion relations (see fig. 2.14). The most important feature of this deformation is that each branch loses its vertical symmetry axis and the electron Fermi velocities become different for different directions of motion. In other words, a breakdown of chiral symmetry occurs. Since this effect was predicted only recently [83, 56], an experimental measurement of its strength is not available yet. Nevertheless, the mentioned calculations indicate that the difference of the Fermi velocities monotonically increases as the spin-orbit coupling is enhanced, and in some quasi-1D semiconductor systems may reach 20% [82]. Since the strength of the Rashba spin-orbit coupling and the carrier concentration can be changed independently, it appears possible to create a strongly interacting (i. e. with small carrier concentration) quasi-1D electron system whose single-particle energy spectrum lacks chiral symmetry as in fig. 2.14. In this case one faces the following fundamental question: how does such an interacting system respond to the asymmetry of the single electron spectrum? The au-

thors have solved analytically the problem and found the following: First, the spin-charge separation of the traditional Tomonaga-Luttinger liquid is destroyed by the spin-orbit coupling in a quasi-1D wire (cf. [80]). The independent bosonic spin and charge excitations of the Tomonaga-Luttinger model are replaced by two independent bosonic mixed spin and charge excitations. As the strength of the spin-orbit coupling increases, the velocity of one of these excitations decreases to zero where it becomes predominantly a spin excitation. Second, the single-particle characteristics, such as the spectral function and the density of states, are essentially modified and controlled by the strength of the spin-orbit coupling. Moreover, varying the spin-orbit coupling with the external electric field can be used to extract the microscopic parameters of the quantum wires.

In this section, we presented the basic ideas of the bosonization technique and gave a brief review of pioneering and recent papers related to the topic of Chapter 5. We did not aim to describe all the technical details of the Tomonaga-Luttinger model so far. Furthermore, the complete textbook-like introduction and historical overview for the bosonization technique partly cited here can be found in the very instructive paper by Jan von Delft and Herbert Schoeller [67]. Nevertheless, in order to demonstrate our progress in this field we shall often refer to the very details of the conventional solution for Tomonaga-Luttinger model. In the next section, we, therefore, solve the model for the simplest case of spinless electrons and derive the plasmon density of states in such a system.

2.7 Density of states in the Tomonaga-Luttinger model

Over the years, the bosonization technique has become a rather popular tool for treating strongly-correlated electron systems in one dimension. The reason for its popularity is that some problems which appear intractable when formulated in terms of fermions turn out to become easy, when formulated in terms of boson fields. For example, the bosonic representation of the Hamiltonian describing interacting one-dimensional electrons, though *biquadratic* in the fermion field, is *quadratic* in bosonic variables, and, therefore, the Hamiltonian can be diagonalized straightforwardly.

As an illustration, let us consider a quantum wire of free, spinless left- and right-moving one-dimensional electrons, labelled by the indices L and R respectively, with dispersion $\varepsilon(p)$ that is bounded from below. We begin by linearizing the initial dispersion relation close to the Fermi points $\pm p_F$ (see fig. 2.15)

$$\varepsilon_{L/R}(k) = \varepsilon(0) \mp \hbar v_F \left(k + k_F \right). \tag{2.50}$$

Here $k \in [-k_F, \infty)$ is the electron wave vector counted from the Fermi one, and

$$v_F = \frac{\partial \varepsilon(p)}{\partial p}$$

is the Fermi velocity. Then the standard definition for the physical fermion field is

$$\psi_{\text{phys}}(x) = \left(\frac{2\pi}{L} \right)^{1/2} \sum_{k=-k_F}^{\infty} \left(e^{-i(k_F+k)x} c_{k,L} + e^{i(k_F+k)x} c_{k,R} \right), \tag{2.51}$$
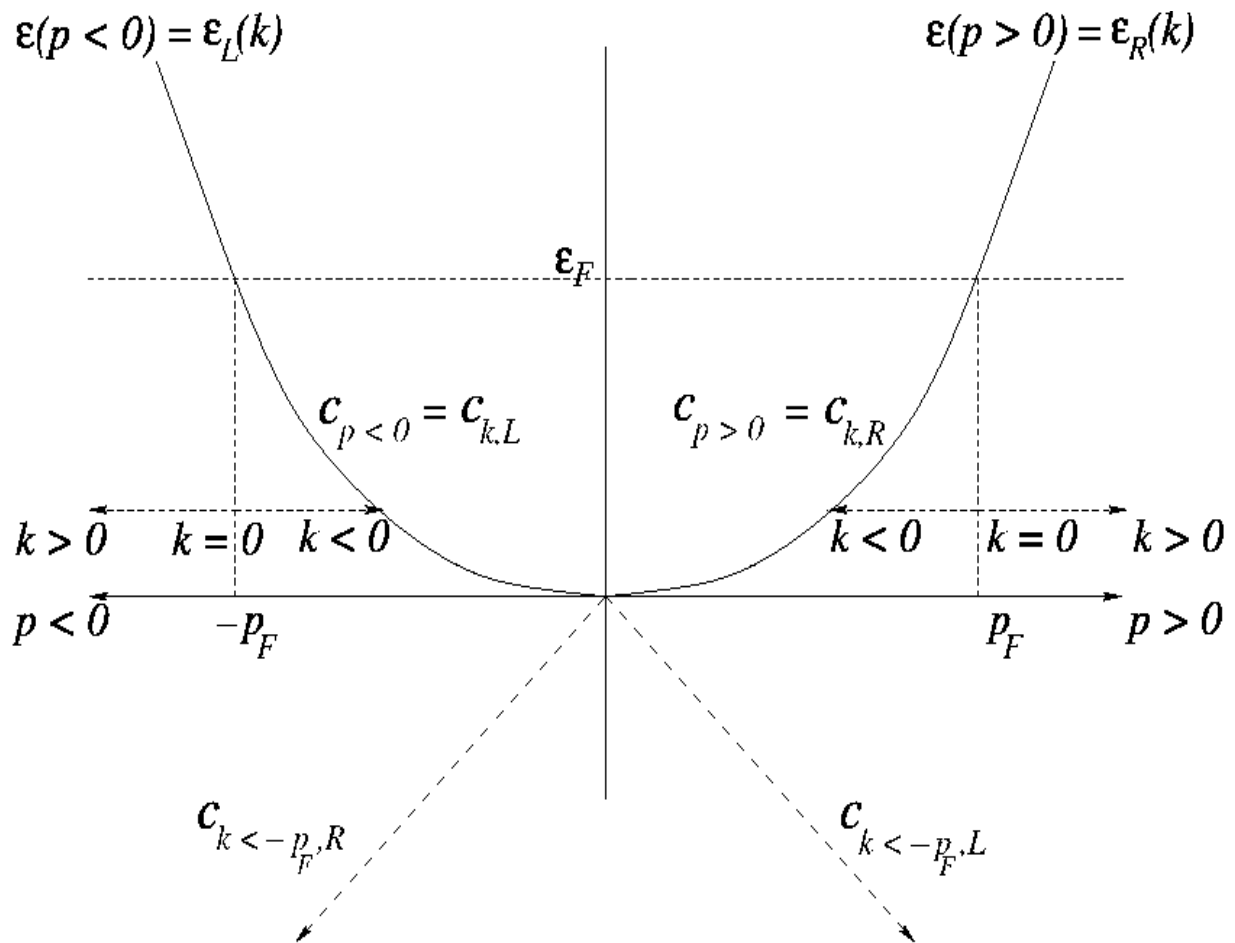
Figure 2.15: The dispersion relation $\varepsilon(p)$ of a 1D wire containing left- and right-moving electrons with $p < 0$ and $p > 0$ respectively. This figure is taken from [67].

where

$$c_{k,L/R} = c_{\mp(k+k_F)}. \tag{2.52}$$

Note, however, that the natural definition of wave vector in (2.50) (where k is bounded from below) contradicts the definition (2.47) used in the bosonization technique (where $k \in (-\infty, \infty)$). To remedy this, we introduce (following Haldane [76] or von Delft & Schoeller [67]) additional unphysical positron states at the bottom of the Fermi sea: we simply extend the range of k to be unbounded by taking $k \in (-\infty, \infty)$, and define the corresponding energies in such a way that they all lie below $\varepsilon(p = 0)$ (see fig. 2.13). The inclusion of positron states in the single-particle Hilbert space and the imposing of definite boundary conditions (in order to quantize k) should be viewed merely as formal tricks that make the problem amenable to bosonization. It is important, that the introduction of those extra unphysical states does not change the low-energy physics of the system, since by construction they require very high energies ($> \varepsilon_F$) for their excitation. (However, they would be excited if a perturbation such as an electric field or impurity

potential were sufficiently strong. Therefore, strong perturbations cannot be dealt with using bosonization.)

Now, we rewrite ψ_{phys} (which is actually not *physical* any more, because the additional unphysical states are included) in the form including positron states

$$\psi_{\text{phys}}(x) = e^{-ik_F x}\psi_L(x) + e^{ik_F x}\psi_R(x), \tag{2.53}$$

where

$$\psi_{L/R}(x) = \left(\frac{2\pi}{L}\right)^{1/2} \sum_{k=-\infty}^{\infty} e^{\mp ikx} c_{k,L/R}. \tag{2.54}$$

Since the fields ψ_L and ψ_R formally differ from each other only by the factor $e^{\mp ikx}$, the only change needed in the bosonization identity (2.46) for ψ_R relative to ψ_L is to replace x by $-x$

$$\psi_{L/R} = F_{L/R}a^{-1/2}e^{\mp\frac{2\pi ix}{L}\left(\hat{N}_{L/R}-\frac{1}{2}\delta_b\right)}e^{-i\phi_{L/R}(x)}, \tag{2.55}$$

where

$$\phi_{L/R}(x) = -\sum_{n_q>0} \frac{1}{\sqrt{n_q}} \left(e^{\mp iqx}b_{q,L/R} + e^{\pm iqx}b_{q,L/R}^{\dagger}\right)e^{-aq/2}. \tag{2.56}$$

In order to study the electron-electron interactions in a one-dimensional wire, we shall consider the following Hamiltonian

$$H = H_{\text{kin}} + H_{\text{int}}, \tag{2.57}$$

where

$$H_{\text{kin}} = \hbar v_F \int_{-L/2}^{L/2} \frac{dx}{2\pi} \left[\psi_L^{\dagger}(x)\left(i\frac{\partial}{\partial x}\right)\psi_L(x) + \psi_R^{\dagger}(x)\left(-i\frac{\partial}{\partial x}\right)\psi_R(x)\right], \tag{2.58}$$

$$H_{\text{int}} = \hbar v_F \int_{-L/2}^{L/2} \frac{dx}{2\pi} \left(g_2\psi_L^{\dagger}(x)\psi_L(x)\psi_R^{\dagger}(x)\psi_R(x) + \right.$$
$$\left. +\frac{1}{2}g_4\left\{\left[\psi_L^{\dagger}(x)\psi_L(x)\right]^2 + \left[\psi_R^{\dagger}(x)\psi_R(x)\right]^2\right\}\right). \tag{2.59}$$

The kinetic term H_{kin} assumes a linear dispersion $\varepsilon = \hbar v_F k$, whereas H_{int} describes local (point-like) electron-electron interactions, parameterized by the dimensionless coupling strengths g_4 and g_2 [67]. The interaction constants g_4 and g_2 can be determined via the Fourier transform of a given inter-electron potential [84], but in practice they are treated as adjustable parameters. Note, that all products of ψ's in (2.58) and (2.59) are fermion normal ordered with respect to the vacuum state $\left|\vec{0}\right\rangle_0$. Using the bosonization identity (2.55) and the boundary conditions for $\phi_{L,R}$ we arrive at the bosonized form of H_{kin} and H_{int}

$$H_{\text{kin}} = \frac{\hbar v_F}{2} \sum_{v=L,R} \left\{\frac{2\pi}{L}N_v + \int_{-L/2}^{L/2} \frac{dx}{2\pi} \left[\frac{\partial\phi_v(x)}{\partial x}\right]^2\right\}, \tag{2.60}$$

$$H_{\text{int}} = \frac{\hbar v_F}{2} \frac{2\pi}{L} \left(g_4 N_L^2 + g_4 N_R^2 + 2 g_2 N_L N_R \right) +$$

$$+ \frac{\hbar v_F}{2} \int\limits_{-L/2}^{L/2} \frac{dx}{2\pi} \left\{ 2 g_2 \frac{\partial \phi_L(x)}{\partial x} \frac{\partial \phi_R(x)}{\partial x} + g_4 \left[\left(\frac{\partial \phi_L(x)}{\partial x} \right)^2 + \left(\frac{\partial \phi_R(x)}{\partial x} \right)^2 \right] \right\}. \tag{2.61}$$

Now, the tremendous advantage of the bosonic representations is clear: H is quadratic in bosonic variables and can be rewritten in the convenient 2×2 matrix form

$$H = \frac{\hbar v_F}{2} \int\limits_{-L/2}^{L/2} \frac{dx}{2\pi} \left(\frac{\partial \phi_L(x)}{\partial x}, \ \frac{\partial \phi_R(x)}{\partial x} \right) \left(\begin{array}{cc} 1+g_4 & g_2 \\ g_2 & 1+g_4 \end{array} \right) \left(\begin{array}{c} \frac{\partial \phi_L(x)}{\partial x} \\ \frac{\partial \phi_R(x)}{\partial x} \end{array} \right). \tag{2.62}$$

The Hamiltonian (2.62) can be diagonalized straightforwardly using a Bogoljubov transformation [85, 67] of the $b_{q,L/R}$'s or just introducing so-called dual fields [86, 87]

$$\Theta(x) = \frac{1}{\sqrt{2}} \left(\phi_L(x) - \phi_R(x) \right),$$

$$\Phi(x) = \frac{1}{\sqrt{2}} \left(\phi_L(x) + \phi_R(x) \right). \tag{2.63}$$

In the latter case we have for H the following expression

$$H = \frac{\hbar v_F}{2} \int\limits_{-L/2}^{L/2} \frac{dx}{2\pi} \left[(1+g_4+g_2) \left(\frac{\partial \Theta(x)}{\partial x} \right)^2 + (1+g_4-g_2) \left(\frac{\partial \Phi(x)}{\partial x} \right)^2 \right]. \tag{2.64}$$

Finally, let us rescale the boson fields $\Phi(x)$ and $\Theta(x)$ in a way which leads the Hamiltonian (2.62) to the canonical, non-interacting-like form (2.60). It is important, however, that the rescaling procedure must preserve the duality of the boson fields. Therefore, the transformation from the old boson fields to the new ones must be *conformal* [84]. In our particular case, the relations between $(\Phi(x), \Theta(x))$ and canonical fields read

$$\Theta_{\text{can}}(x) = \left(\frac{1+g_4+g_2}{1+g_4-g_2} \right)^{\frac{1}{4}} \Theta(x),$$

$$\Phi_{\text{can}}(x) = \left(\frac{1+g_4-g_2}{1+g_4+g_2} \right)^{\frac{1}{4}} \Phi(x), \tag{2.65}$$

and the Hamiltonian takes the form

$$H = \frac{\hbar u}{2} \int\limits_{-L/2}^{L/2} \frac{dx}{2\pi} \left[\left(\frac{\partial \Theta_{\text{can}}(x)}{\partial x} \right)^2 + \left(\frac{\partial \Phi_{\text{can}}(x)}{\partial x} \right)^2 \right], \tag{2.66}$$

where the renormalized velocity u reads

$$u = v_F \sqrt{(1 + g_4)^2 - g_2^2}. \tag{2.67}$$

Here, we arrive at a very interesting point of this section. We have started from the rather complicated Hamiltonian (2.57) and, after some manipulations, obtained the much simpler form (2.66) which looks like the non-interacting one (2.60). The properties of free bosons described by (2.60) are, of course, very well known. Thus, the interacting case can be easily described in terms of free boson fields $(\Phi_{\text{can}}(x), \Theta_{\text{can}}(x))$ with a certain renormalized velocity u. To illustrate the last statement, we shall calculate something measurable, namely, the density of states in the one-dimension wire described by the Hamiltonian (2.57) or (2.66). (The density of states for such a simple system will be compared with the more complicated case investigated in Chapter 5.)

The density of states in the case of interacting electrons can be derived via corresponding fermionic Green's functions $G_{L/R}^{\text{ret}}(x,t)$ [88]

$$\rho_{L/R}^{\text{DoS}}(\omega) = -\frac{1}{2} \Im \int\limits_{-\infty}^{\infty} \frac{dt}{2\pi\hbar} e^{i\omega t} G_{L/R}^{\text{ret}}(x = 0, t), \tag{2.68}$$

where $\hbar\omega$ is the excitation energy, and the Green's functions are the correlators

$$G_{L/R}^{\text{ret}}(x,t) = \frac{1}{i} \left\{ \left\langle \mathcal{T} \, \psi_{L/R}(x,\tau)\psi_{L/R}^{\dagger}(0,0) \right\rangle |_{\tau=i(t-i0)} - \right.$$

$$\left. - \left\langle \mathcal{T} \, \psi_{L/R}(x,\tau)\psi_{L/R}^{\dagger}(0,0) \right\rangle |_{\tau=i(t+i0)} \right\} \Theta(t). \tag{2.69}$$

Here τ is the Matsubara time, and $\Theta(t)$ is the Heaviside theta function of the real time t. The fermionic correlators in (2.69) can be calculated via bosonic ones using the bosonization identity (2.55). The following relation can be obtained straightforwardly

$$\left\langle \mathcal{T} \, \psi_{L/R}(x,\tau)\psi_{L/R}^{\dagger}(0,0) \right\rangle =$$

$$= \frac{\text{sign}_\tau}{a} \exp\left(\left\langle \mathcal{T} \, \phi_{L/R}(x,\tau)\phi_{L/R}^{\dagger}(0,0) - \phi_{L/R}(0,0)\phi_{L/R}^{\dagger}(0,0) \right\rangle \right), \tag{2.70}$$

where sign_τ is simply the sign of τ.

The free bosonic correlation function for one-dimensional wires of the length L has been derived, for example, in [67]. The expression has the form

$$\left\langle \mathcal{T} \, \Phi_{\text{can}}(x,\tau)\Phi_{\text{can}}^{\dagger}(0,0) \right\rangle = -\ln\left[\frac{2\pi}{L} \left(\text{sign}_\tau \, v_F \tau + i\text{sign}_\tau \, x + a \right) \right]. \tag{2.71}$$

Using (2.71) and the relations (2.65), (2.63) between $\phi_{L/R}$ and the canonical boson fields we come to the following formula for the *interacting* bosonic correlation functions

$$\left\langle \mathcal{T} \, \phi_{L/R}(x,\tau)\phi_{L/R}^{\dagger}(0,0) \right\rangle = -\nu\ln\left[\frac{2\pi}{L} \left(\text{sign}_\tau \, u\tau + i\text{sign}_\tau \, x + a \right) \right], \tag{2.72}$$
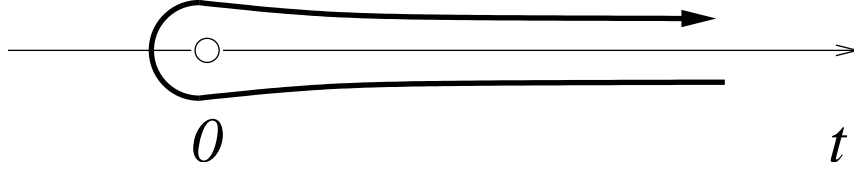
Figure 2.16: The contour C for the integral over t (2.76) in the density of states.

where ν is the interaction parameter related to g_2 and g_4 as

$$\nu = \frac{1}{2}\left(\sqrt{\frac{1+g_4+g_2}{1+g_4-g_2}} + \sqrt{\frac{1+g_4-g_2}{1+g_4+g_2}}\right). \tag{2.73}$$

It is interesting to note, that the interactions between electrons with opposite chiralities (parameterized by g_2) play a significant role here. Indeed, if g_2 is zero, then $\nu = 1$ (as if it was a non-interacting case), though $g_4 \neq 0$. Note, however, that the velocity u is renormalized (compared to v_F) in both cases: $g_2 = 0$, $g_4 \neq 0$ and $g_{2,4} \neq 0$.

Substituting (2.72) into (2.70), we obtain the following useful relation

$$\left\langle \mathcal{T}\, \psi_{L/R}(x,\tau)\psi^{\dagger}_{L/R}(0,0)\right\rangle = \frac{\operatorname{sign}_\tau a^{\nu-1}}{(\operatorname{sign}_\tau u\tau + i\operatorname{sign}_\tau x + a)^{\nu}}. \tag{2.74}$$

Now we are ready to derive $\rho^{\mathrm{DoS}}_{L/R}(\omega)$. Using (2.74), (2.69) and (2.68) we get

$$\rho^{\mathrm{DoS}}_{L/R}(\omega) = -\frac{1}{2}\Im\left(\frac{1}{i}\right)^{1+\nu}\frac{a^{\nu-1}}{u^{\nu}}\int\limits_{0}^{\infty}\frac{dt}{2\pi\hbar}e^{i\omega t}\left[\frac{1}{(t-i0)^{\nu}} - \frac{1}{(t+i0)^{\nu}}\right]. \tag{2.75}$$

The integral over t can be rewritten as

$$\int\limits_{0}^{\infty}\frac{dt}{2\pi\hbar}e^{i\omega t}\left[\frac{1}{(t-i0)^{\nu}} - \frac{1}{(t+i0)^{\nu}}\right] = \frac{i^{\nu+1}\omega^{\nu-1}}{2\pi\hbar}\int\limits_{C}dz\frac{e^{-z}}{(-z)^{\nu}}, \tag{2.76}$$

where the contour C is depicted in fig. 2.16.

At this point, it is convenient to utilize the definition of the Γ-function [89]. Then the density of states reads

$$\rho^{\mathrm{DoS}}_{L/R}(\omega) = -\frac{1}{2\pi\hbar u}\left(\frac{a\omega}{u}\right)^{\nu-1}\sin(\pi\nu)\,\Gamma(1-\nu). \tag{2.77}$$

For the free-fermion case $g_{2,4} = 0$ we have $\nu = 1$, i. e. in this case we recover the standard Fermi-liquid property $\rho^{\mathrm{DoS}}_{L/R} = (2\pi\hbar v_F)^{-1}$ for any value of ω. However, for any $g_2 \neq 0$ we have $\nu > 1$, i. e. $\rho^{\mathrm{DoS}}_{L/R} \to 0$ for $\omega \to 0$. Thus, the interactions cause the density of states to vanish at the Fermi energy [67]. This property is one of the most spectacular differences between a Tomonaga-Luttinger liquid and a Fermi one.

In view of the results given in Chapter 5, it is also important to emphasize here, that the density of states is equal for both left- and right-moving electrons. The index L/R in (2.77) is, therefore, not really important. However, this is not the case as soon as the spin-orbital effects are in play. Then ρ_L^{DoS} can not be equal to ρ_R^{DoS} even for $\nu = 1$, and the solution of the Tomonaga-Luttinger model becomes very non-trivial. The problem will be discussed in Chapter 5 of this thesis.

3 Spin-orbit Berry phase in a quantum loop

In this Chapter, we find a manifestation of a spin-orbit Berry phase in the conductance of a mesoscopic loop with Rashba spin-orbit coupling placed in an external magnetic field which is perpendicular to the loop plane. The transmission probability at different radii and potential profiles of the loop is calculated as a function of the external magnetic field. In addition, the non-adiabatic regime (at small loop radii) is investigated.

3.1 Description of the system

As it was discussed in the introductory Chapter 2, the adiabatic Berry phase (as well as its non-adiabatic generalization — the Aharonov-Anandan geometric phase) is a key aspect of electronic transport in inhomogeneous magnetic fields. In spite of a large variety of implementations, all schemes mentioned in the review involve Aharonov-Bohm oscillations as a necessary component for Berry phase investigations. In the present work, we find a manifestation of Berry's phase in the conductance oscillations that stem directly from the interference between two spin states with different dynamical phases, and the Aharonov-Bohm oscillations do not occur. We concentrate on the theoretical investigation of the setup similar to [35, 36] (see the detailed description in Chapter 2). There are, however, some important differences.

First, the possibility for electrons to bypass the ring is assumed to be negligible in our system. Therefore, the electron beam does not split while it enters or leaves the ring. Thus, we study rather *a quantum loop* (fig. 3.1) than *a quantum ring* connected to the tangential lead [36, 35]. That is why, the Aharonov-Bohm effect does not occur here.

Second, we consider a modulation of the potential profile in the loop region by means of a gate voltage applied to the structure. Although the fabrication of such a setup may require rather complicated design, the authors of [36, 35] let us know of their latest development, where they have managed to solve the technological problems and gated InAs rings have been fabricated.

And finally, our system is purely one-dimensional, while this is not the case in [36, 35]. However, as long as a gate voltage can be applied, the upper bands can be easily depopulated so that only a single band is occupied. Therefore, the one-dimensionality of the quantum loop is not a big problem anymore.

In order to find the transmission probability through such a system we have to solve the corresponding Schrödinger equation. To this end we divide the system in three parts: input channel,
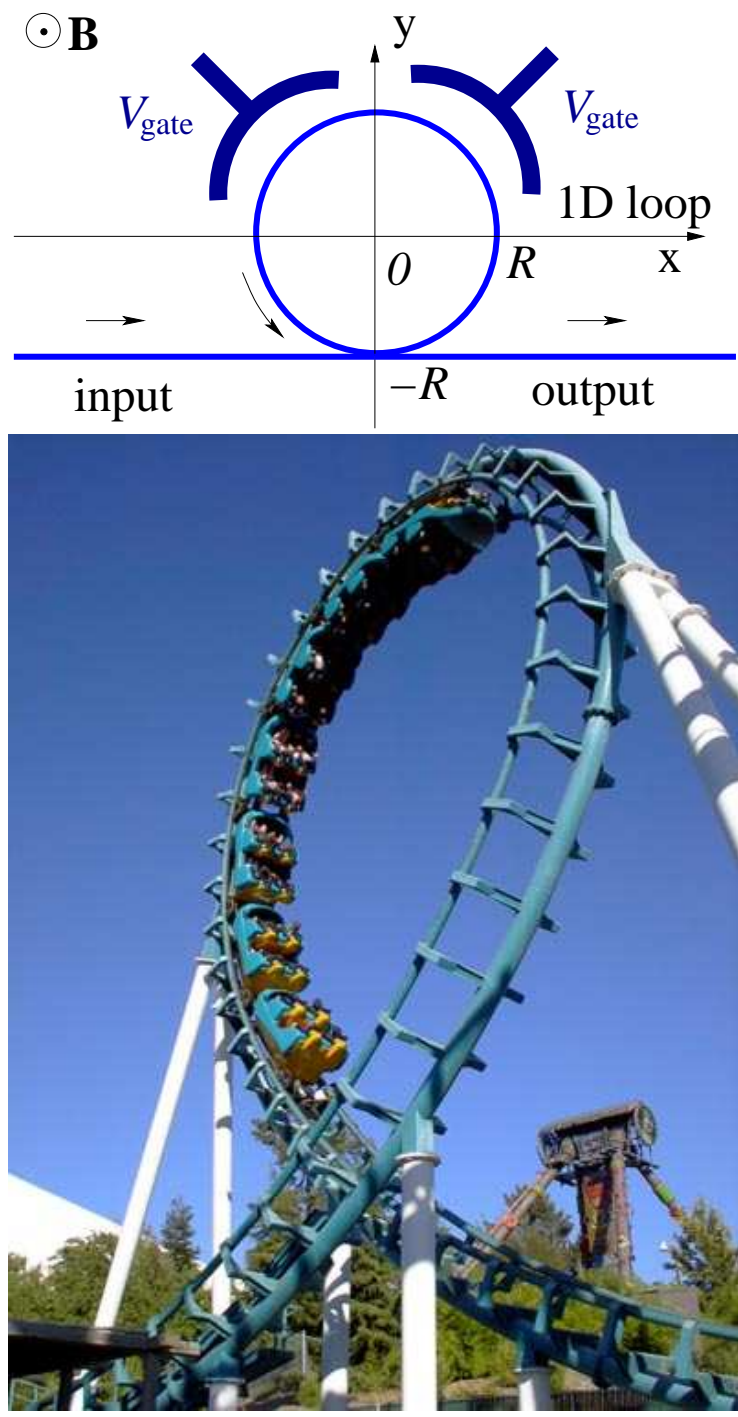
Figure 3.1: Geometry of the system. The photo below illustrates the important difference between the quantum ring connected to a tangential lead [36, 35] and the quantum loop studied here. Our setup is a kind of roller coaster for electrons: they do not collide at the crossing point!
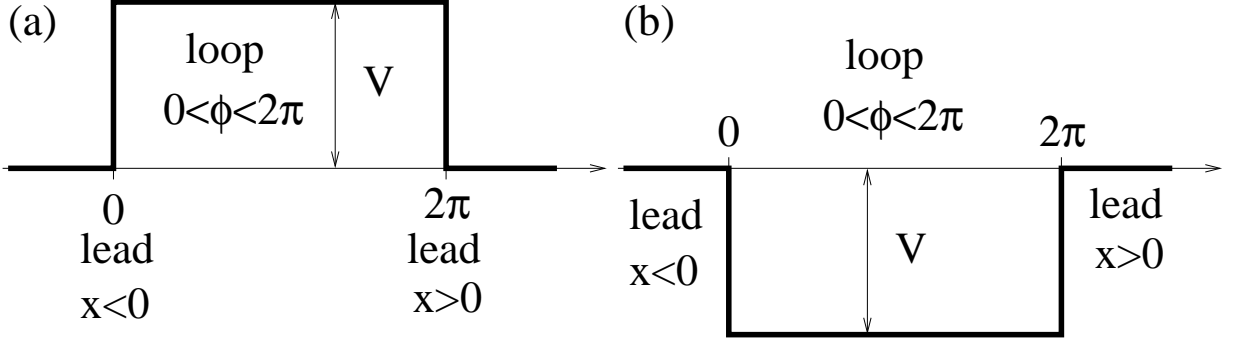
Figure 3.2: Two variants of the potential profile adopted in the solution. The bottom of the bands can be lifted (a) or pulled down (b) in the loop region by V.

the loop itself (which is actually the arc of 2π-length in our case) and output channel. The Hamiltonians describing the propagation of electrons in the input/output channels read

$$H_{\text{wire}} = \begin{pmatrix} \frac{\hbar^2}{2m^*}\hat{k}_x^2 + \varepsilon_Z & i\alpha\hat{k}_x \\ -i\alpha\hat{k}_x & \frac{\hbar^2}{2m^*}\hat{k}_x^2 - \varepsilon_Z \end{pmatrix}, \tag{3.1}$$

whereas the propagation through the loop of radius R is governed by the Hamiltonian

$$H_{\text{loop}} = \begin{pmatrix} \varepsilon_0\hat{q}_\varphi^2 + \varepsilon_Z + V & \frac{\alpha}{R}e^{-i\varphi}\left(\hat{q}_\varphi - \frac{1}{2}\right) \\ \frac{\alpha}{R}e^{i\varphi}\left(\hat{q}_\varphi + \frac{1}{2}\right) & \varepsilon_0\hat{q}_\varphi^2 - \varepsilon_Z + V \end{pmatrix}. \tag{3.2}$$

Here $\hat{k}_x = -i\frac{\partial}{\partial x} - \frac{\Phi}{\Phi_0}\frac{1}{R}$, $\hat{q}_\varphi = -i\frac{\partial}{\partial\varphi} - \frac{\Phi}{\Phi_0}$ are momentum and angular momentum operators respectively, $\Phi = \pi R^2 B_z$ is the magnetic flux, Φ_0 is the flux quantum, $\varepsilon_0 = \hbar^2/(2m^*R^2)$ is the size confinement energy with the effective electron mass m^*, $\varepsilon_Z = g^*\mu_B B_z/2$ is the Zeeman energy, and V denotes the energy shift determined by the gate voltage applied to the loop (see fig. 3.2 for the examples of the profile studied below).

We adopt the vector potential $\mathbf{A}$ to be tangential to the direction of the current. Thus, in the loop we choose $\mathbf{A}(x,y) = \frac{1}{2}B_z(x\mathbf{j} - y\mathbf{i})$, or, in cylindrical coordinates, $A_\varphi(\varphi) = \Phi/2\pi R$, whereas the vector potential in the input and output channels is determined by the continuity condition at the junction point with the loop itself ($x = 0$, $y = -R$); hence we have $A_x = \Phi/2\pi R$.

We denote the wave functions for each part as $\Psi_{\text{loop}}^{\pm}(\varphi)$ for the loop, $\Psi_{\text{in}}^{\pm}(x)$ and $\Psi_{\text{out}}^{\pm}(x)$ for input and output channels respectively. In order to find the wave function describing the whole system, we impose the boundary conditions that warrant the continuity of the wave function and its first derivative at the boundaries between the loop and input/output channels

$$\begin{cases} \Psi_{\text{in}}^+|_{x=0} + \Psi_{\text{in}}^-|_{x=0} = \Psi_{\text{loop}}^+|_{\varphi=-\pi/2} + \Psi_{\text{loop}}^-|_{\varphi=-\pi/2}, \\ \Psi_{\text{loop}}^+|_{\varphi=3\pi/2} + \Psi_{\text{loop}}^-|_{\varphi=3\pi/2} = \Psi_{\text{out}}^+|_{x=0} + \Psi_{\text{out}}^-|_{x=0}, \\ \nabla\Psi_{\text{in}}^+|_{x=0} + \nabla\Psi_{\text{in}}^-|_{x=0} = \nabla\Psi_{\text{loop}}^+|_{\varphi=-\pi/2} + \nabla\Psi_{\text{loop}}^-|_{\varphi=-\pi/2}, \\ \nabla\Psi_{\text{loop}}^+|_{\varphi=3\pi/2} + \nabla\Psi_{\text{loop}}^-|_{\varphi=3\pi/2} = \nabla\Psi_{\text{out}}^+|_{x=0} + \nabla\Psi_{\text{out}}^-|_{x=0}; \end{cases} \tag{3.3}$$

The operator ∇ is given by $\nabla = \frac{1}{R}\frac{d}{d\varphi}$ in the loop region, and $\nabla = \frac{d}{dx}$ in the input and output channels.

In the next section, we find the electron eigen states for the loop, input, output channels, and solve the system of equations (3.3). The solution gives us the transmission and reflection amplitudes (and, as consequence, the transmission/reflection probabilities) for each spin mode.

3.2 Solution of the problem

Let us start from the input channel. The Hamiltonian (3.1) acts in SU(2) spin space. The corresponding Schrödinger equation allows two solutions

$$\Psi_{\text{in}}^{+}(x) = e^{\frac{i\Phi}{\Phi_0 R}x}\begin{pmatrix} \cos\gamma^{+}\left(e^{ik^{+}x}+A^{+}e^{-ik^{+}x}\right) \\ -i\sin\gamma^{+}\left(e^{ik^{+}x}-A^{+}e^{-ik^{+}x}\right) \end{pmatrix},\tag{3.4}$$

$$\Psi_{\text{in}}^{-}(x) = e^{\frac{i\Phi}{\Phi_0 R}x}\begin{pmatrix} -i\sin\gamma^{-}\left(e^{ik^{-}x}-A^{-}e^{-ik^{-}x}\right) \\ \cos\gamma^{-}\left(e^{ik^{-}x}+A^{-}e^{-ik^{-}x}\right) \end{pmatrix},\tag{3.5}$$

where

$$\tan\gamma^{\pm} = -\frac{\varepsilon_Z}{k^{\pm}\alpha}+\sqrt{1+\left(\frac{\varepsilon_Z}{k^{\pm}\alpha}\right)^2},\tag{3.6}$$

and "$\pm$" are the spin indices.

Since the main contribution to the current is given by the electrons at the Fermi level, we consider the eigen states (3.4) and (3.5) at the fixed energy E_F. Thus, the wave vectors $k^{\pm}$ in (3.4) and (3.5) are the Fermi ones, and they satisfy the dispersion relations

$$E_F = \frac{\hbar^2 k^{\pm 2}}{2m^*}\pm\sqrt{\alpha^2 k^{\pm 2}+\varepsilon_Z^2}.\tag{3.7}$$

This equation has two solutions with respect to k for each spin index. These two solutions correspond to the Fermi wave vectors for electrons with opposite chirality. The absolute values of the Fermi wave vectors with a given spin index for the left- and right-moving electrons are equal in the straight channels.

Each line in (3.4) and (3.5) consists of two parts: the incident wave and the reflected one. The coefficients $A^{\pm}$ are the reflection amplitudes that have to be found imposing the boundary conditions (3.3). For the output channel the reflection amplitudes are assumed to be zero, and the corresponding spinors read

$$\Psi_{\text{out}}^{+}(x) = \begin{pmatrix} D^{+}\cos\gamma^{+}e^{i(k^{+}+\frac{\Phi}{\Phi_0 R})x} \\ -iD^{+}\sin\gamma^{+}e^{i(k^{+}+\frac{\Phi}{\Phi_0 R})x} \end{pmatrix},\tag{3.8}$$

$$\Psi_{\text{out}}^-(x) = \begin{pmatrix} -iD^- \sin\gamma^- e^{i(k^- + \frac{\Phi}{\Phi_0 R})x} \\ D^- \cos\gamma^- e^{i(k^- + \frac{\Phi}{\Phi_0 R})x} \end{pmatrix}. \tag{3.9}$$

Here $D^\pm$ are the transmission amplitudes.

The eigenfunctions of the Hamiltonian (3.2) are of the form

$$\Psi_{\text{loop}}^+(\varphi) = e^{i\frac{\Phi}{\Phi_0}\varphi} \begin{pmatrix} B^+ \cos\alpha^+ e^{i(q_R^+ - \frac{1}{2})\varphi} + C^+ \cos\beta^+ e^{-i(\frac{1}{2}+q_L^+)\varphi} \\ B^+ \sin\alpha^+ e^{i(\frac{1}{2}+q_R^+)\varphi} - C^+ \sin\beta^+ e^{-i(q_L^+ - \frac{1}{2})\varphi} \end{pmatrix}, \tag{3.10}$$

$$\Psi_{\text{loop}}^-(\varphi) = e^{i\frac{\Phi}{\Phi_0}\varphi} \begin{pmatrix} -B^- \sin\alpha^- e^{i(q_R^- - \frac{1}{2})\varphi} + C^- \sin\beta^- e^{-i(\frac{1}{2}+q_L^-)\varphi} \\ B^- \cos\alpha^- e^{i(\frac{1}{2}+q_R^-)\varphi} + C^- \cos\beta^- e^{-i(q_L^- - \frac{1}{2})\varphi} \end{pmatrix}, \tag{3.11}$$

where

$$\tan\alpha^\pm = \frac{\varepsilon_0 q_R^\pm - \varepsilon_Z}{q_R^\pm \alpha/R} + \sqrt{1 + \left(\frac{\varepsilon_Z - \varepsilon_0 q_R^\pm}{q_R^\pm \alpha/R}\right)^2}, \tag{3.12}$$

$$\tan\beta^\pm = -\frac{\varepsilon_0 q_L^\pm + \varepsilon_Z}{q_L^\pm \alpha/R} + \sqrt{1 + \left(\frac{\varepsilon_Z + \varepsilon_0 q_L^\pm}{q_L^\pm \alpha/R}\right)^2}, \tag{3.13}$$

and $q_{R,L}^\pm$ are the Fermi angular momenta in the curved part of the wire that are found from the conditions which explicitly include the height of the barrier V

$$E_F = V + \frac{\varepsilon_0}{4} + \varepsilon_0 q_R^{\pm 2} \pm \sqrt{\left(\frac{q_R^\pm \alpha}{R}\right)^2 + \left(q_R^\pm \varepsilon_0 - \varepsilon_Z\right)^2}, \tag{3.14}$$

$$E_F = V + \frac{\varepsilon_0}{4} + \varepsilon_0 q_L^{\pm 2} \pm \sqrt{\left(\frac{q_L^\pm \alpha}{R}\right)^2 + \left(q_L^\pm \varepsilon_0 + \varepsilon_Z\right)^2}. \tag{3.15}$$

It is interesting to note, that Fermi angular momenta for electrons with opposite chiralities ($q_L^\pm$ and $q_R^\pm$) are not equal to each other. This effect stems from the particular geometry of the system. Indeed, as soon as we assume $R \to \infty$ the relations (3.14) and (3.15) both become equal to (3.7), where $k_R^\pm = k_L^\pm$. Thus, the chiral asymmetry of Fermi angular momenta is essentially of geometrical origin as the Berry phase itself.

The imposing of the boundary conditions (3.3) on the wave functions (3.4), (3.5), (3.8) – (3.11) gives us a system of eight equations (7.1) – (7.8). (The equations can be found in Appendix A.) That system definitely has an analytical solution with respect to $A^\pm$, $B^\pm$, $C^\pm$ and $D^\pm$. However, the formulae for the amplitudes are extremely cumbersome. Therefore, we do not adduce them here.

3.3 Current densities in 1D wires with spin-orbit coupling

At this point it is pertinent to turn to the current density calculations. The conventional formula for the current density j flowing in a given mode $\Psi(x)$ reads [90]

$$\mathbf{j} = \frac{\hbar}{2m^*}\left[\Psi(x)\hat{k}_x^*\Psi^*(x) + \Psi^*(x)\hat{k}_x\Psi(x)\right]. \tag{3.16}$$

This formula is derived for a Hamiltonian of the form $H = \hat{p}^2/(2m^*) + V(x)$, where the spin and orbital degrees of freedom are separable. This is not the case in presence of spin-orbit interactions. In what follows, we derive the correct formula for the current density in one-dimensional wires with Rashba coupling described by the Hamiltonian (3.1).

Let $\Psi(x)$ be a spinor with the elements $\Psi_1(x)$ and $\Psi_2(x)$ so, that

$$\Psi(x) = \left(\begin{array}{c} \Psi_1(x) \\ \Psi_2(x) \end{array}\right). \tag{3.17}$$

On one hand, we have the continuity equation for the current flow

$$\frac{\partial}{\partial t}\int dx |\Psi|^2 = -\int dx\,\text{div}\mathbf{j}. \tag{3.18}$$

On the other hand, we have the time-dependent Schrödinger equation $i\hbar(\partial\Psi/\partial t) = H\Psi$ that gives us the relation

$$\frac{\partial}{\partial t}\int dx |\Psi|^2 = \frac{i}{\hbar}\int dx\,(\Psi H^*\Psi^* - \Psi^* H\Psi). \tag{3.19}$$

The right-hand side of (3.19) can be rewritten explicitely using (3.1)

$$\frac{i}{\hbar}\int dx\,(\Psi H_{\text{wire}}^*\Psi^* - \Psi^* H_{\text{wire}}\Psi) =$$

$$= \frac{i}{\hbar}\int dx\left[\Psi_1\left(\frac{\hbar^2\hat{k}_x^2}{2m^*}\Psi_1\right)^* - \Psi_1^*\left(\frac{\hbar^2\hat{k}_x^2}{2m^*}\Psi_1\right) + \Psi_1\left(i\alpha\hat{k}_x\Psi_2\right)^* - \Psi_1^*\left(i\alpha\hat{k}_x\Psi_2\right) + \right.$$

$$\left. +\Psi_2\left(-i\alpha\hat{k}_x\Psi_1\right)^* - \Psi_2^*\left(-i\alpha\hat{k}_x\Psi_1\right) + \Psi_2\left(\frac{\hbar^2\hat{k}_x^2}{2m^*}\Psi_2\right)^* - \Psi_2^*\left(\frac{\hbar^2\hat{k}_x^2}{2m^*}\Psi_2\right)\right]. \tag{3.20}$$

Note, that the Zeeman term vanishes in (3.20).

Using the equations (3.18) and (3.20) we can find div$\mathbf{j}$ straightforwardly,

$$-\text{div}\mathbf{j} = \frac{i\hbar}{2m^*}\left(-\Psi_1\frac{\partial^2\Psi_1^*}{\partial x^2} - \frac{2i}{R}\frac{\Phi}{\Phi_0}\Psi_1\frac{\partial\Psi_1^*}{\partial x} + \Psi_1^*\frac{\partial^2\Psi_1}{\partial x^2} - \frac{2i}{R}\frac{\Phi}{\Phi_0}\Psi_1^*\frac{\partial\Psi_1}{\partial x} - \right.$$

$$\left. -\Psi_2\frac{\partial^2\Psi_2^*}{\partial x^2} - \frac{2i}{R}\frac{\Phi}{\Phi_0}\Psi_2\frac{\partial\Psi_2^*}{\partial x} + \Psi_2^*\frac{\partial^2\Psi_2}{\partial x^2} - \frac{2i}{R}\frac{\Phi}{\Phi_0}\Psi_2^*\frac{\partial\Psi_2}{\partial x}\right) +$$

$$+\frac{i\alpha}{\hbar}\left(\Psi_1\frac{\partial\Psi_2^*}{\partial x}-\Psi_1^*\frac{\partial\Psi_2}{\partial x}-\Psi_2\frac{\partial\Psi_1^*}{\partial x}+\Psi_2^*\frac{\partial\Psi_1}{\partial x}\right). \tag{3.21}$$

Then, the desired formula for $\mathbf{j}$ reads

$$\mathbf{j}=\frac{\hbar}{2m^*}\left(\Psi_1\hat{k}_x^*\Psi_1^*+\Psi_1^*\hat{k}_x\Psi_1+\Psi_2\hat{k}_x^*\Psi_2^*+\Psi_2^*\hat{k}_x\Psi_2\right)-$$

$$-\frac{i\alpha}{\hbar}\left(\Psi_1\Psi_2^*-\Psi_1^*\Psi_2\right). \tag{3.22}$$

Using the general relation (3.22) one can easily find the input, reflected and transmitted current densities for our particular system. Note, that each current density is given as a sum of its two spin components $j=j^++j^-$, and each component can be found using the following formulas

$$j_{\text{in}}^{\pm}=\frac{\hbar}{m^*}\left[k^{\pm}\pm\frac{\alpha m^*}{\hbar^2}\sin(2\gamma^{\pm})\right], \tag{3.23}$$

$$j_{\text{refl}}^{\pm}=-\frac{\hbar}{m^*}|A^{\pm}|^2\left[k^{\pm}\pm\frac{\alpha m^*}{\hbar^2}\sin(2\gamma^{\pm})\right], \tag{3.24}$$

$$j_{\text{out}}^{\pm}=\frac{\hbar}{m^*}|D^{\pm}|^2\left[k^{\pm}\pm\frac{\alpha m^*}{\hbar^2}\sin(2\gamma^{\pm})\right]. \tag{3.25}$$

Here, we have used the elementary trigonometric formula $2\sin\gamma^{\pm}\cos\gamma^{\pm}=\sin2\gamma^{\pm}$.

3.4 Results and discussion

Now, we have everything ready to study the propagation of the initial states given by (3.4) and (3.5) through the loop. We define the transmission probability as

$$T=\frac{j_{\text{out}}}{j_{\text{in}}}, \tag{3.26}$$

while the reflection one reads

$$R=\frac{j_{\text{refl}}}{j_{\text{in}}}. \tag{3.27}$$

The plots of the transmission probability as a function of the external magnetic field are shown in fig. 3.3 (solid lines) for different radii of the loop. The additional dotted lines correspond to the transmission probabilities through the wire of length $L=2\pi R$ separated from the input and output channels by barriers of the same height as the loop is separated from its leads. The dependencies in fig. 3.3 exhibit the following characteristic features.

First, the transmission probability oscillates as a function of the external magnetic field B_z. The oscillating factors appear in the transmission probability, because of the interference between propagated states at the input and output of the loop. It is well known, that the transmission probability for the quantum particle propagating across a single rectangular potential barrier of
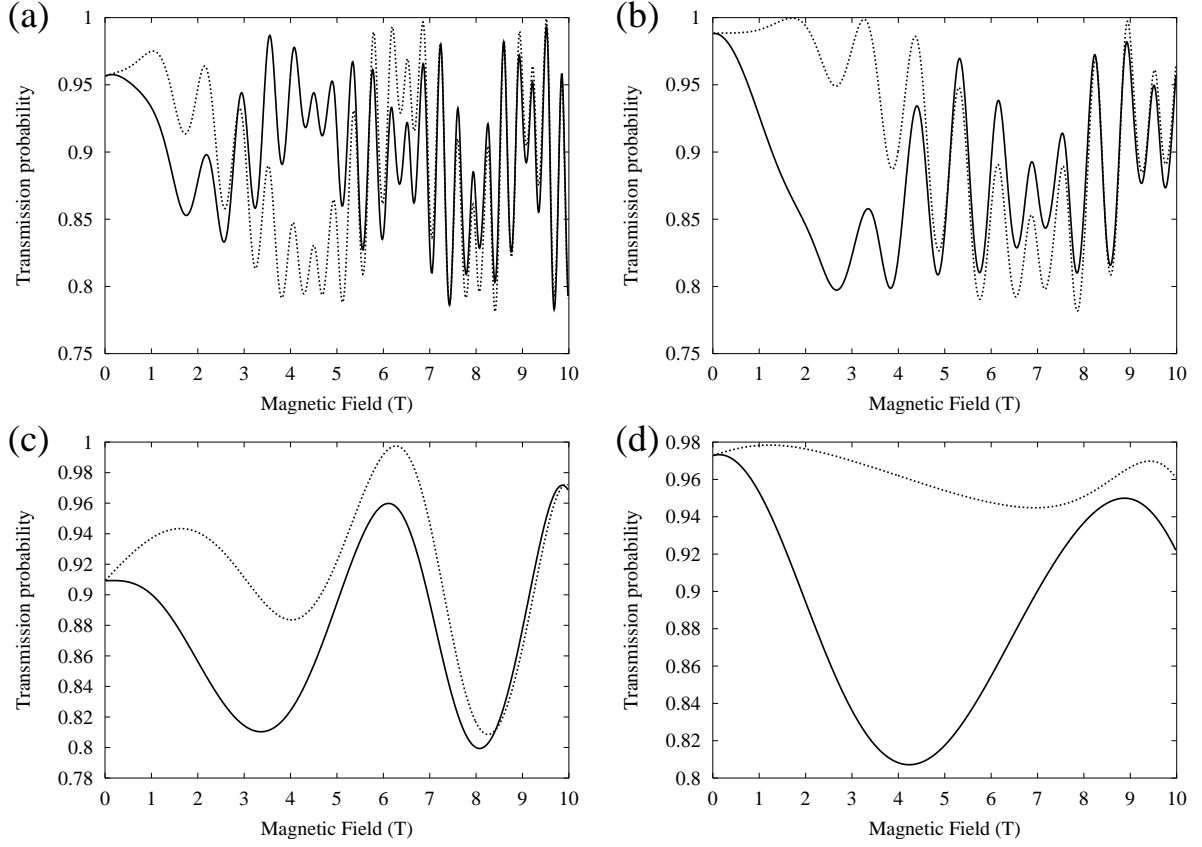
Figure 3.3: Transmission probabilities for the loop of radius R (solid lines) and corresponding straight wire of length $L = 2\pi R$ (dotted lines) versus external magnetic field. Each panel corresponds to different loop radii: (a) $R = 10^{-4}$cm, (b) $R = 5 \cdot 10^{-5}$cm, (c) $R = 10^{-5}$cm, and (d) $R = 5 \cdot 10^{-6}$cm. The barrier height V is taken equal to 18.75meV. The other parameters are taken relevant for InAs: $\alpha = 2 \cdot 10^{-11}$eVm, $m^* = 0.033 m_e$, $g^* = -12$, $E_F = 30$meV.

length L contains the oscillating factor $\sin(Lk)$, where k is the wave vector of the particle [90]. Our case is a bit more complicated since we have two spin-split modes with different wave vectors. Moreover, the absolute values of the Fermi angular momenta for the left- and right-moving electrons with the same spin index differ from each other. Therefore, we have many oscillating factors with different periods determined by q_R^+, q_L^+, q_R^-, q_L^- and their combinations. These angular momenta depend on the external magnetic field and, therefore, the oscillations $T(B_z)$ occur. We emphasize, that the fundamental origin of the oscillations depicted in fig. 3.3 is exactly the same as in the simple single-mode model [90]. In other words, our system is a kind of quantum interferometer with the characteristic length $2\pi R$.

Second, there is a strong difference between transmission probabilities for the loop and the straight wire at certain intermediate values of the magnetic field (see fig. 3.3), while at higher values and at $B_z = 0$ both curves just coincide. This is a particular manifestation of the Berry phase that we explain in what follows. First of all note, that the Berry phase is always zero in the
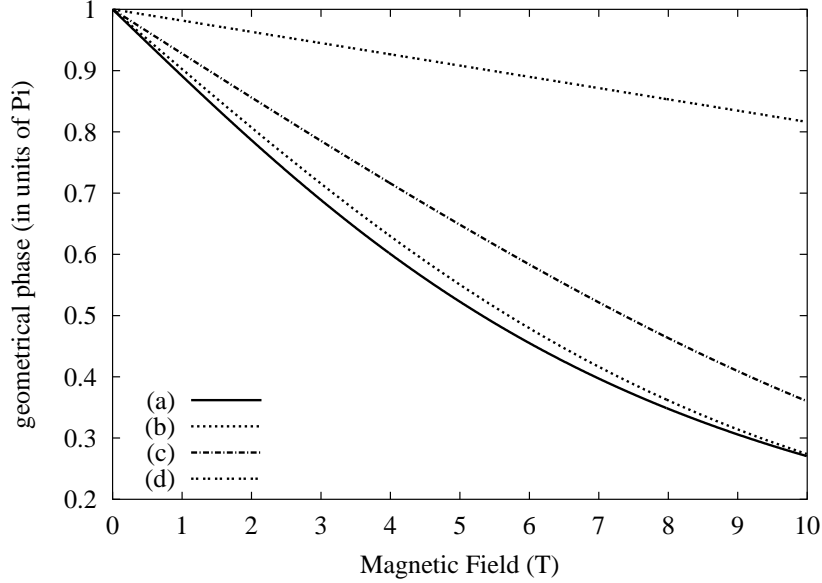
Figure 3.4: The geometrical phase as a function of the external magnetic field at different loop radii: (a) adiabatic approximation (2.45), (b) $R = 10^{-5}$cm, (c) $R = 5 \cdot 10^{-6}$cm, and (d) $R = 10^{-6}$cm. The barrier height V is taken equal to zero, and other parameters are taken relevant for InAs: $\alpha = 2 \cdot 10^{-11}$eVm, $m^* = 0.033 m_e$, $g^* = -12$, $E_F = 30$meV.

straight wire. In contrast to that simple case, an additional Berry phase dependent interference factor $\sin \phi_B$ occurs while an electron wave function propagates through the loop. The Berry phase (2.45) is negligible at $B_{ext} \equiv B_z \gg B_{in}$ and equal to π at $B_z = 0$ (see fig. 3.4). Therefore, the factor $\sin \phi_B$ does not show up in these cases. At certain intermediate values of B_z the difference between straight wire and loop geometry is essential. In particular, at certain special values of the external magnetic field the Berry phase is close to $\pi/2$ and the difference between transmission probabilities for the loop and the straight wire is maximal. We find it necessary to estimate such a magnetic field using the quasi-classical formula (2.45) and assuming parameters relevant for InAs: $\alpha = 2 \cdot 10^{-11}$eVm, $g^* = -12$, $k = 10^6$cm^{-1}. Then, the Berry phase value $\pi/2$ corresponds to $B_z = |B_{in}|/\sqrt{3}$ or, numerically, ~ 3T that is in good agreement with the plots.

The influence of the barrier height on the interference pattern is shown in figs. 3.5– 3.8. First of all, one can easily see, that the transmission probability for the loop can also exceed its characteristic value for the straight wire. Most importantly, however, the critical value of the magnetic fields (where the difference between transmission probabilities for the loop and straight wire is maximal) is very sensitive to the barrier height V. This is explained in what follows.

It is obvious, that the potential profile changes the Fermi momenta in the loop. Since the Berry phase explicitly depends on the characteristic wave vector of the particle (2.45), we have a possibility to change the Berry phase by tuning the potential profile. In detail, B_{in} is *proportional* to the wave vector of the particle, whereas the Fermi momentum for a given mode is larger for a deeper potential profile (i. e. for smaller or even negative V). Thus, the critical value of the
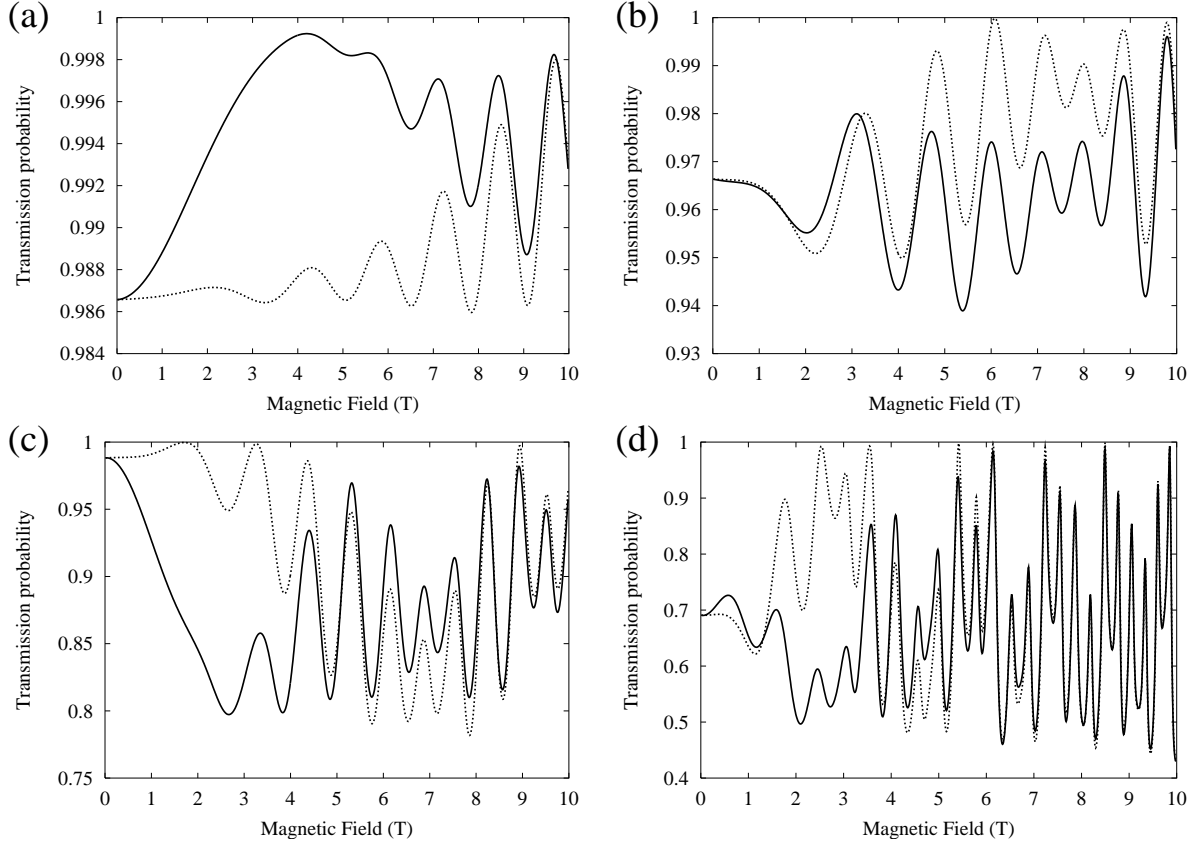
Figure 3.5: Transmission probabilities for the loop of radius $R = 5 \cdot 10^{-5}$cm (solid lines) and corresponding straight wire of length $L = 2\pi R$ (dotted lines) versus external magnetic field. Each panel corresponds to different heights of the barrier V: (a) $V = 6.25$meV, (b) $V = 12.5$meV, (c) $V = 18.75$meV, and (d) $V = 25$meV. The other parameters are the same as for fig. 3.3

external magnetic field $B_z = B_{in}/\sqrt{3}$ (which corresponds to $\phi_B = \pi/2$) is shifted to higher values when the electron bands are pulled down by V. Moreover, at certain negative values of V the Fermi wave vectors are so large, that the critical value $B_z = B_{in}/\sqrt{3}$ exceeds 10T, and, therefore, the point, where Berry's phase vanishes ($B_z \gg B_{in}$) leaves the reasonable range of magnetic fields depicted in fig. 3.7. Note, that this effect becomes even more pronounced in the non-adiabatic case (see fig. 3.8).

At the end of the discussion, let us make some important comments on the role of the loop radius in the effect studied. Indeed, the further questions arise when we compare the plots in figs. 3.3a, b, d and 3.3d, 3.5 and 3.6, 3.7 and 3.8. It is clearly seen, that the maximum of the difference between transmission probabilities of the loop and a straight wire is shifted to higher magnetic fields. However, the Berry phase does not depend on the radius of curvature. Nevertheless, we can explain the effect if we remember, that the formula (2.45) (and the Berry concept as well) is valid only for the adiabatic motion. The latter means, that $\alpha m^* R/\hbar^2$ must be lager than one, so that the electron spin precesses a few times while it is moving through the loop. This is not the
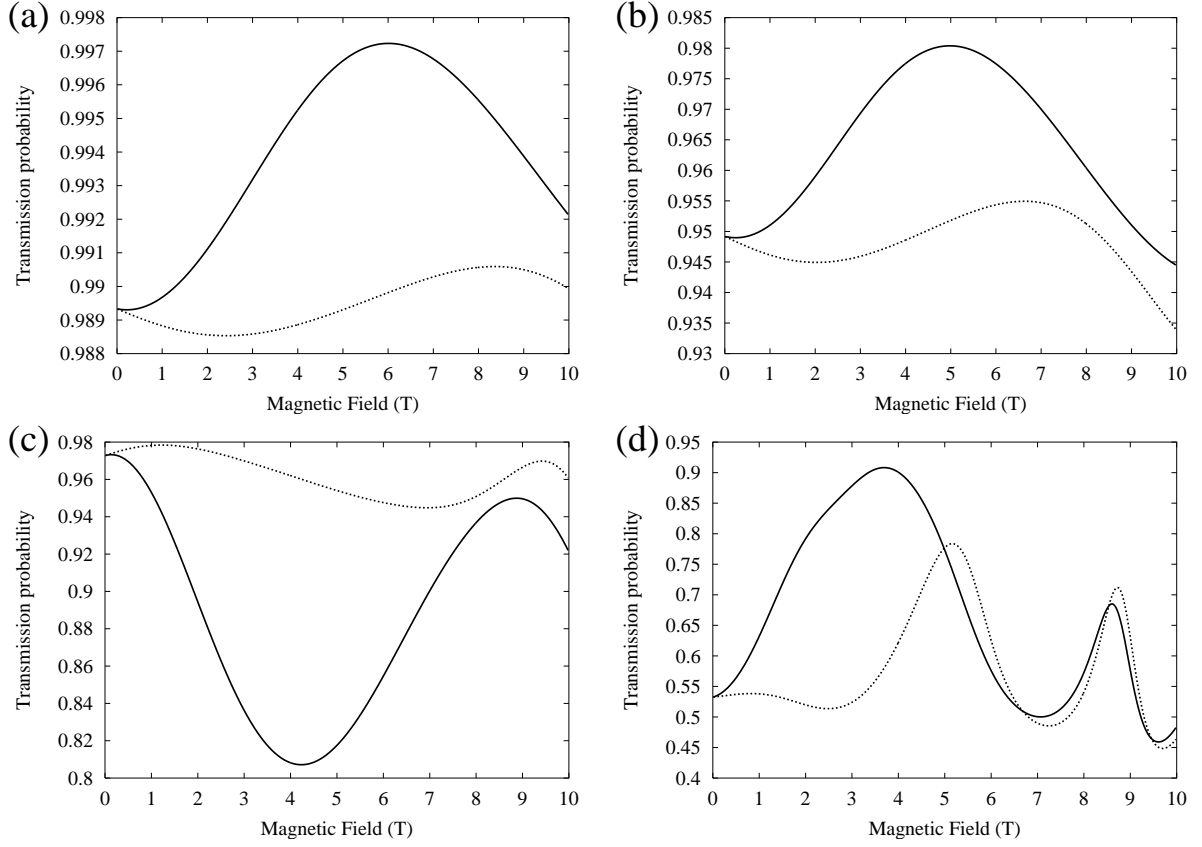
Figure 3.6: Transmission probabilities for the loop radius $R = 5 \cdot 10^{-6}$cm in the non-adiabatic regime (solid lines), and corresponding straight wire of length $L = 2\pi R$ (dotted lines) versus external magnetic field. Each panel corresponds to different heights of the barrier V: (a) $V = 6.25$meV, (b) $V = 12.5$meV, (c) $V = 18.75$meV, and (d) $V = 25$meV. The other parameters are the same as for fig. 3.3.

case depicted in figs. 3.3d, 3.6, 3.8, where $\alpha m^* R/\hbar^2 \sim 0.5$ and the spin evolution is definitely not adiabatic.

Note, that our general approach is valid for both adiabatic and non-adiabatic cases, because we use a direct solution of the Schrödinger equation. Therefore, we are able to see the Aharonov-Anandan geometric phase [17] effects in figs. 3.3d, 3.6, 3.8. This kind of geometrical phase is the non-adiabatic generalization of Berry's, and in our case it reads

$$\phi_{\text{top}} = \pi \left[1 \mp (q_L^{\pm} - q_R^{\pm}) \right]. \tag{3.28}$$

(Here, the index "top" means "topological".)

In the introduction given in Chapter 2, we have learnt, that the finite curvature of the one-dimensional wire with spin-orbit interactions increases the spin-splitting between dispersion curves along the momentum axis (recall fig. 2.4). We believe, that this is true in the presence of an external magnetic field as well. If the index "+" corresponds to the upper mode, then the difference $q_L^+ - q_R^+$ decreases, whereas $q_L^- - q_R^-$ increases as long as the spin-splitting becomes larger (for smaller radiuses of curvature). Thus, the geometric phase is radius dependent
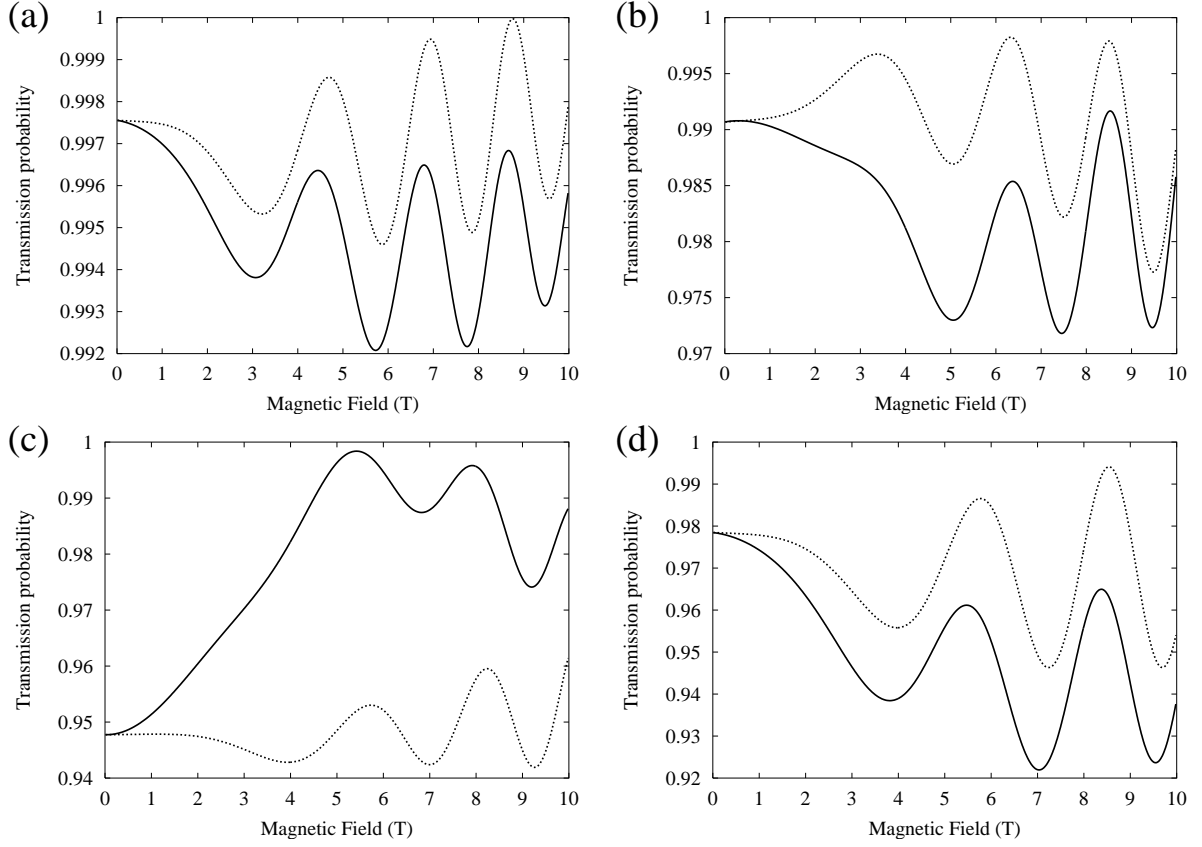
Figure 3.7: Transmission probabilities for the loop of radius $R = 5 \cdot 10^{-5}$cm in the adiabatic regime (solid lines) and corresponding straight wire of length $L = 2\pi R$ (dotted lines) versus external magnetic field. The parameters are the same as for fig. 3.5, but the height of the barrier is taken negative: (a) $V = -6.25$meV, (b) $V = -12.5$meV, (c) $V = -18.75$meV, and (d) $V = -25$meV.

in the non-adiabatic regime $\hbar^2/(2m^*\alpha R) \gg 1$. Of course, the expression (3.28) and its adiabatic analogue (2.45) give close results in the appropriate regime (see fig. 3.4).

In conclusion of this section, we have studied quantum transport in a mesoscopic loop with Rashba coupling and Zeeman splitting. Here, we have found that the Berry phase gives a well pronounced interference effect in form of a deviation of the transmission probability from its value for the straight wire of the same length $L = 2\pi R$ at some specific external magnetic fields. Moreover, we have investigated our system in the non-adiabatic regime and found, that the characteristic magnetic fields, which provide the strong deviation, are shifted to higher values. And finally, these specific values of the magnetic field are very sensitive to the potential profile in the loop.
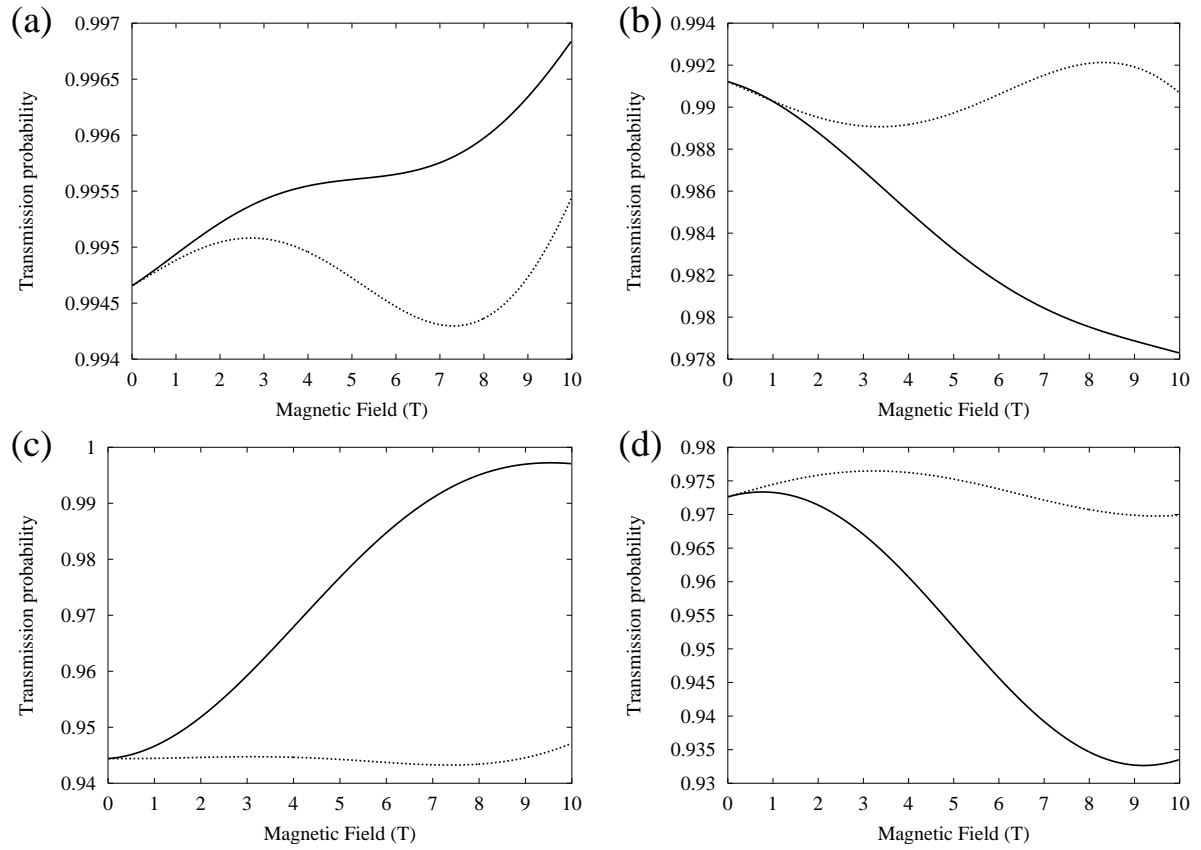
Figure 3.8: Transmission probabilities for the loop of radius $R = 5 \cdot 10^{-6}$cm in the non-adiabatic regime (solid lines) and corresponding straight wire of length $L = 2\pi R$ (dotted lines) versus external magnetic field. The other parameters are the same as for fig. 3.5, but the height of the barrier is taken negative: (a) $V = -6.25$meV, (b) $V = -12.5$meV, (c) $V = -18.75$meV, and (d) $V = -25$meV. Note, that the region of the magnetic fields, where $B_z \gg B_{\mathrm{in}}$ (and the difference between solid and dotted lines vanishes) is shifted to very high values.

4 Spin manipulation by means of curved one-dimensional wires

In this Chapter, we describe a semiconductor structure that can rotate and switch the electron spin without using ferromagnetic contacts, tunneling barriers, external radiation etc. The structure consists of a strongly curved one-dimensional ballistic wire with intrinsic spin-orbit interactions of Rashba type. Our calculations and analytical formulae show that the proposed device can redistribute the current densities between the two spin-split modes without backscattering and, thus, serve as a reflectionless and high-speed spin switcher. Using parameters relevant for InAs we investigate the projection of current density spin polarization on the spin-quantization axis as a function of the Rashba constant, external magnetic field, and radius of the wire's curvature.

4.1 The basic idea

In the introductory Chapter 2 we have discussed some of possible spin-filtering devices. The second necessary component of the desired spin field effect transistor is the spin-rotator (or spin-switch).

The schematic of the "conventional" spin-rotator based on the Rashba effect is depicted in fig. 4.1a. The straight quantum wire (or just a two-dimensional stripe) is divided into three regions. In the middle region of length L, the spin-orbit interactions are finite, whereas in the input and output channels the spin-orbit coupling is set to zero. In other words, the semiconductor region in which the Rashba effect occurs does not extend into the spin source and drain [91]. The angle of the spin rotation depends explicitly on the length of the stripe between the input and output contacts, namely

$$\Delta\vartheta = \frac{2m^*\alpha L}{\hbar^2},\tag{4.1}$$

where m^* is the effective electron mass, α is the Rashba constant. The spin-switching speed of this device (i. e. the minimal time necessary to rotate the spin for the angle of $\Delta\vartheta = \pi$) has been estimated in the Introduction. It reaches the value of 0.2 ps for InAs in the ballistic transport regime.

In spite of impressive advantages, the "conventional" scheme involves propagation of electrons across borders separating the media with different spin-orbit coupling strength. A reflection on the border is thus a necessary complement that diminishes the total current through the device and even might compromise the feasibility of the proposal. In this Chapter, we propose a scheme

of a *reflectionless* spin-rotator made of material with Rashba spin-orbit interaction such as InAs. We consider a *curved* wire consisting of a semicircle with radius R attached to the infinite straight one-dimensional channels, as shown in fig. 4.1b. The channels are made of the *same* material as the semicircle itself, thus, the electron backscattering is negligible. Moreover, because of the specific geometry of the system, the speed of response can even exceed the one for the "conventional" spin-rotator discussed above. The device is placed in a perpendicular magnetic field **B**, which can be used to control the spin-rotation (in addition to the Rashba constant tuned by the external electric field). Curved one-dimensional quantum channels in InAs [92] are expected to be used for the experimental check of the present proposal. The spin polarized electrons necessary for such experiments can be generated directly in InAs by circularly polarized light [49, 61]. Note, that the recombination of spin polarized charged carriers results in the emission of circularly polarized light. It is possible, therefore, to use optical methods for the detection of the electron spin-polarization as well.

On the face of it, the device depicted in fig. 4.1b is similar to the one investigated by Bulgakov and Sadreev [93]. However, there is an essential difference in approaches used here and in [93]. In that work, the authors assume *a priory* an adiabatic regime: the radius of the curvature is so large that the electrons do not feel the junction between the curved part of the wire and input/output channels. In contrast, we start from the very general solution of Schrödinger's equation for the *whole* system (i. e. input channel — semi-circle — output channel) and find that though the electron backscattering is still negligible, the redistribution between current densities with opposite spin indices can occur at certain comparatively small radii of curvature (that is forwardscattering in some sense).

Before we proceed the description of our model, it is necessary to mention the reference [94], where the geometrically induced potentials have been investigated in curved mesoscopic systems. In particular, flexing the quantum wire leads to a potential of the form

$$U_g = -\frac{\hbar^2}{8m^*R^2},$$ (4.2)

where R is the radius of curvature at the point of the wire's bend. We emphasize, that our approach includes the change of the geometrical potential automatically. However, the effect of U_g on the electron motion is negligible in real systems [92] (as well as in our model) since the geometrical potential is much smaller than the Fermi energy ($U_g/E_F \lesssim 10^{-3}$ for curved InAs wires [35, 36, 92]).

In order to describe the degree of the current density redistribution between modes with opposite spin indices we introduce the following quantity

$$P = \frac{j^+ - j^-}{j^+ + j^-},$$ (4.3)

where $j^{\pm}$ denote the current densities with a given spin orientation, and "$\pm$" are the spin indices. Note, that the usual definition for the spin polarization involves *densities* of particles with opposite spin orientation. However, definition (4.3) with *current densities* is more relevant for the
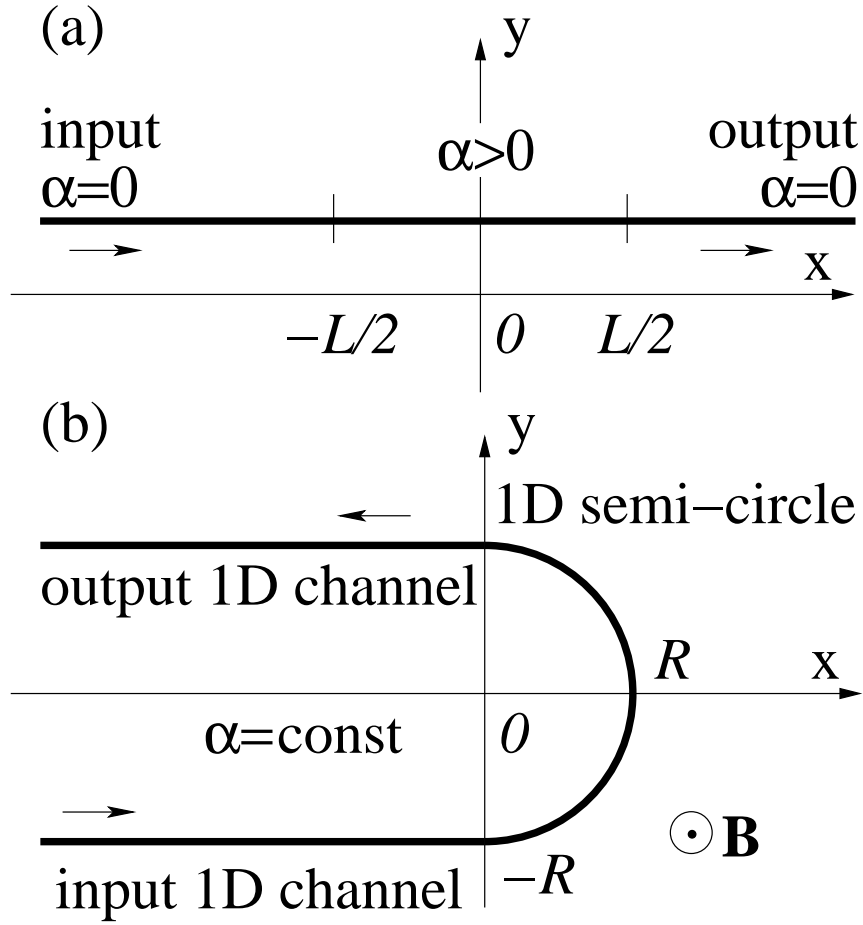
(a)

y

input
α=0

α>0

output
α=0

x

−L/2   0   L/2

(b)

y

1D semi−circle

output 1D channel

R   x

α=const   0

⊙ **B**

input 1D channel   −R

Figure 4.1: (a) Schematic of the "conventional" spin-rotator. In the central region of the wire the spin-orbit interaction is finite, whereas in the input and output channels the Rashba effect vanishes. (b) Schematic of the reflectionless and high-speed spin-rotator. The quantum wire is made of just one material so, that the Rashba constant in the curved part is the same as in the input and output channels.

transport measurements. It seems essential to emphasize that the quantity P is controllable experimentally since the currents j^+ and j^- can be generated and detected independently by means of absorption of two circularly polarized light beams with opposite helicity [49, 61].

If one prefers to control P by means of magnetized contacts then the situation is a bit more complicated. Indeed, the quantity P has the meaning of projection of the current density spin-polarization on the spin-quantization axis. The orientation of the spin-quantization axis is determined by the relation between the external magnetic field **B** and in-plane Zeeman-like magnetic field B_{in} generated by the Rashba spin-orbit interactions

$$B_{in} = \frac{2\alpha k_0}{g^* \mu_B}. \tag{4.4}$$

Here k_0 is the characteristic Fermi wave vector, whereas g^* and μ_B are the g-factor and the Bohr
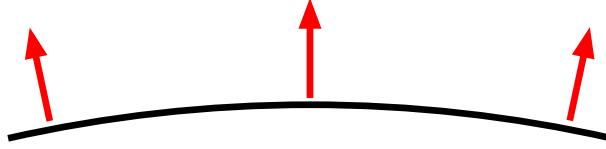
Figure 4.2: Spin dynamics in a slightly curved wire with spin-orbit coupling. The electron spin follows adiabatically the electron trajectory, and the angle between the direction of the motion and the spin does not change.

magneton respectively. The field B_{in} is orthogonal to the direction of the electron motion, therefore the spin-quantization axis lies in the yz plane (for the input and output channels). The angle γ_0 between the z axis and the spin-quantization can be estimated from the simple trigonometric formula

$$\tan\gamma_0 = \frac{B_{in}}{|\mathbf{B}|}. \tag{4.5}$$

If the external magnetic field $|\mathbf{B}| = B_z$ is much larger than the in-plane one, then the spin-quantization axis coincides with the z axis. In contrast, if the external magnetic field is absent then the spin-quantization axis is orthogonal to the direction of the electron motion at each point of its trajectory. In the following, we call the quantity P defined by (4.3) just spin-polarization.

The basic idea of the device depicted in fig. 4.1b can be explained as follows. The spin dynamics in a media with spin-orbit interactions depends essentially on the form of electron trajectory. If the trajectory changes adiabatically (i. e. the radius of the wire is quite large), then the angle between the direction of the motion and the spin remains constant in each point of a trajectory as it is shown in fig. 4.2. However, the electron spin in laboratory coordinates changes its orientation. In contrast, if 100% spin-polarized electron beam is reflected by an infinite barrier (as it is shown in fig. 4.3), then the angle between the direction of the motion and the spin changes. This regime is strongly non-adiabatic. Here, the electron spin does not change, however, its orientation in laboratory coordinates.

The transition between these two (adiabatic and non-adiabatic) regimes can give us some additional possibilities for spin manipulation in semiconductor structures. Both of these regimes can be realized in the proposed device depicted in fig. 4.1b. Indeed, if we assume the radius of the curved part in fig. 4.1b to be zero, then we arrive at the one-dimensional wire with an infinite barrier and the regime is non-adiabatic. In contrast, if the radius of the curved part is large enough, then we have the adiabatic regime depicted in fig. 4.2. The transition between these two regimes will be studied in this Chapter.

In the next sections, we study the output polarization defined by (4.3) in two different cases. First, we assume, that the electrons in the input wire are in their eigen states Ψ_{in}^+ and Ψ_{in}^- given by (3.4) and (3.5) respectively. Then, we study the current density redistribution between "+" and "−" modes at different parameters of the system: external magnetic field and radius of curvature. Moreover, we show, that the initial phase difference between Ψ_{in}^+ and Ψ_{in}^- plays a significant role for the output polarization. We call such a setup "spin rotator".
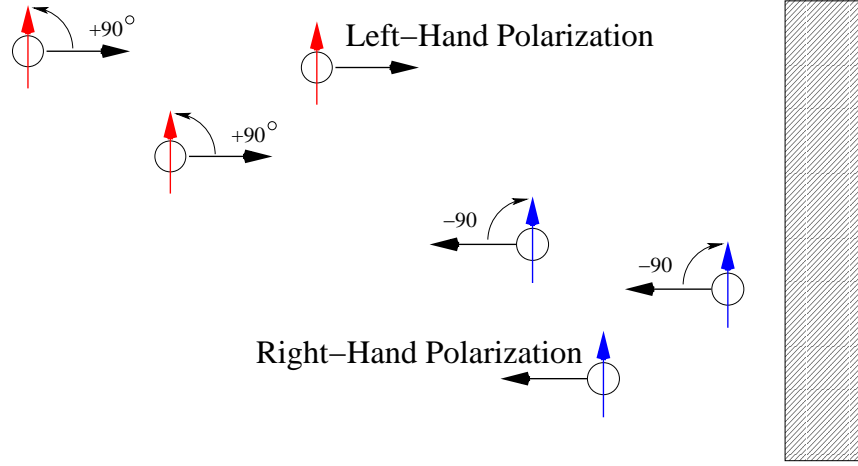
Figure 4.3: The reflection of left-hand spin-polarized electrons (i. e. the angle between the direction of the motion and the spin is $+90°$) from an infinite barrier in a media with spin-orbit interactions. The electrons do not have enough time to change the direction of their spins while the direction of motion is changed. Therefore, the left-hand polarization is changed to right-hand one (i. e. the angle between the direction of the motion and the spin becomes $-90°$). This figure is expected to give an intuitive explanation of what happens in fig. 4.1 if the radius of the curved part is infinitely small.

The second case corresponds to the setup that we call a "spin switch". The electrons in the input wire are assumed to be only in the eigen state Ψ_{in}^{+}, i. e. the electron beam is 100% spin-polarized. Then, we demonstrate the possibility to switch the spin polarization P to its opposite value by means of the device depicted in fig. 4.1b.

4.2 Curved 1D wire as a spin rotator

First, we calculate single particle spin-split states for the system shown in fig. 4.1b. To this end we use the same approach as in the previous Chapter. Again, we divide the wire into three parts: the input channel, the semi-circle (curved part of the quantum wire) and the output channel. We use cartesian coordinates to describe the input and output channels (the region $x < 0$ in fig. 4.1b) and the polar coordinates for the description of the curved part of the wire (the semi-circle). The Hamiltonians describing the propagation of electrons in the input/output wires are exactly the same as in the Chapter 3, whereas the propagation through the curved part of the wire is governed by the Hamiltonian

$$H_{\text{loop}} = \begin{pmatrix} \varepsilon_0 \hat{q}_\varphi^2 + \varepsilon_Z & \alpha e^{-i\varphi} \left(\hat{q}_\varphi - \frac{1}{2} \right) / R \\ \alpha e^{i\varphi} \left(\hat{q}_\varphi + \frac{1}{2} \right) / R & \varepsilon_0 \hat{q}_\varphi^2 - \varepsilon_Z \end{pmatrix}. \tag{4.6}$$

In contrast to (3.2), there is no additional barrier at the entrance into the curved part. This is the most important difference between the setup depicted in fig. 4.1b and the system discussed in the Chapter 3.

Similar to the previous Chapter, the vector potential $\mathbf{A}$ is assumed to be tangential to the direction of the current: $A_\varphi(\varphi) = \Phi/2\pi R$ in the curved part and $A_x = \Phi/2\pi R$ in the leads so, that the continuity conditions at the junction points $x = 0$, $y = \pm R$ are preserved.

We keep the notations introduced in the previous Chapter for the wave functions in the input/output channels and curved part of the wire: $\Psi_{\text{in}}^\pm(x)$, $\Psi_{\text{out}}^\pm(x)$ and $\Psi_{\text{loop}}^\pm(\varphi)$ respectively. The following boundary conditions warrant the continuity of the wave function and its first derivative on the boundaries between the three parts of the system

$$
\begin{cases}
\Psi_{\text{in}}^+(x)|_{x=0} + \Psi_{\text{in}}^-(x)|_{x=0} = \Psi_{\text{loop}}^+(\varphi)|_{\varphi=-\pi/2} + \Psi_{\text{loop}}^-(\varphi)|_{\varphi=-\pi/2}, \\
\Psi_{\text{loop}}^+(\varphi)|_{\varphi=\pi/2} + \Psi_{\text{loop}}^-(\varphi)|_{\varphi=\pi/2} = \Psi_{\text{out}}^+(x)|_{x=0} + \Psi_{\text{out}}^-(x)|_{x=0}|_{x=0}, \\
\nabla\Psi_{\text{in}}^+(x)|_{x=0} + \nabla\Psi_{\text{in}}^-(x)|_{x=0} = \nabla\Psi_{\text{loop}}^+(\varphi)|_{\varphi=-\pi/2} + \nabla\Psi_{\text{loop}}^-(\varphi)|_{\varphi=-\pi/2}, \\
\nabla\Psi_{\text{loop}}^+(\varphi)|_{\varphi=\pi/2} + \nabla\Psi_{\text{loop}}^-(\varphi)|_{\varphi=\pi/2} = \nabla\Psi_{\text{out}}^+(x)|_{x=0} + \nabla\Psi_{\text{out}}^-(x)|_{x=0}.
\end{cases}
\tag{4.7}
$$

The solution of Schrödinger's equations for Hamiltonians (3.1), (4.6) gives the desired wave functions for the input, output and curved parts of the system. For the input channel we have a similar solution as for the loop-like structure studied in the Chapter 3. However, in contrast to (3.4), (3.5), the initial phases $\theta^\pm$ of the incident waves are included explicitly for each mode

$$
\Psi_{\text{in}}^+(x) = e^{\frac{i\Phi}{\Phi_0 R}x}
\begin{pmatrix}
\cos\gamma^+ \left(e^{i\theta^+ + ik^+ x} + A^+ e^{-ik^+ x} \right) \\
-i\sin\gamma^+ \left(e^{i\theta^+ + ik^+ x} - A^+ e^{-ik^+ x} \right)
\end{pmatrix},
\tag{4.8}
$$

$$
\Psi_{\text{in}}^-(x) = e^{\frac{i\Phi}{\Phi_0 R}x}
\begin{pmatrix}
-i\sin\gamma^- \left(e^{i\theta^- + ik^- x} - A^- e^{-ik^- x} \right) \\
\cos\gamma^- \left(e^{i\theta^- + ik^- x} + A^- e^{-ik^- x} \right)
\end{pmatrix}.
\tag{4.9}
$$

For the output channel the eigen functions read

$$
\Psi_{\text{out}}^+(x) =
\begin{pmatrix}
D^+ \cos\gamma^+ e^{i(k^+ + \frac{\Phi}{\Phi_0 R})x} \\
iD^+ \sin\gamma^+ e^{i(k^+ + \frac{\Phi}{\Phi_0 R})x}
\end{pmatrix},
\tag{4.10}
$$

$$
\Psi_{\text{out}}^-(x) =
\begin{pmatrix}
iD^- \sin\gamma^- e^{i(k^- + \frac{\Phi}{\Phi_0 R})x} \\
D^- \cos\gamma^- e^{i(k^- + \frac{\Phi}{\Phi_0 R})x}
\end{pmatrix}.
\tag{4.11}
$$

Here, in contrast to (3.8) and (3.9), the sign of $\gamma^\pm$ is changed since the electron motion changes its direction to the opposite one. It is useful to write down the Fermi momenta explicitly in the form

$$
k^\pm = \sqrt{2m^*}\sqrt{\frac{\hbar^2 E_F + m^* \alpha^2 \pm \sqrt{2m^* E_F \hbar^2 \alpha^2 + m^{*2}\alpha^4 + \hbar^4 \varepsilon_Z^2}}{\hbar^4}}.
\tag{4.12}
$$

In the case of zero magnetic field ($\varepsilon_Z = 0$), the expression (4.12) reduces to

$$
k^\pm = \mp\frac{m^*\alpha}{\hbar^2} + k_0,
\tag{4.13}
$$

where $k_0 = \sqrt{(m^* \alpha / \hbar^2)^2 + 2m^* E_F / \hbar^2}$.

The eigenfunctions of the Hamiltonian (4.6) have the same form as for the loop described in the previous Chapter

$$\Psi_{\text{loop}}^+ (\varphi) = e^{i\frac{\Phi}{\Phi_0}\varphi} \begin{pmatrix} B^+ \cos\alpha^+ e^{i(q_R^+ - \frac{1}{2})\varphi} + C^+ \cos\beta^+ e^{-i(\frac{1}{2}+q_L^+)\varphi} \\ B^+ \sin\alpha^+ e^{i(\frac{1}{2}+q_R^+)\varphi} - C^+ \sin\beta^+ e^{-i(q_L^+ - \frac{1}{2})\varphi} \end{pmatrix}, \tag{4.14}$$

$$\Psi_{\text{loop}}^- (\varphi) = e^{i\frac{\Phi}{\Phi_0}\varphi} \begin{pmatrix} -B^- \sin\alpha^- e^{i(q_R^- - \frac{1}{2})\varphi} + C^- \sin\beta^- e^{-i(\frac{1}{2}+q_L^-)\varphi} \\ B^- \cos\alpha^- e^{i(\frac{1}{2}+q_R^-)\varphi} + C^- \cos\beta^- e^{-i(q_L^- - \frac{1}{2})\varphi} \end{pmatrix}. \tag{4.15}$$

However, the Fermi angular momenta in the curved part of the system $q_{R,L}^\pm$ do not contain the barrier height V. They can be found from the conditions

$$E_F = \frac{\varepsilon_0}{4} + \varepsilon_0 q_R^{\pm 2} \pm \sqrt{\left(\frac{q_R^\pm \alpha}{R}\right)^2 + (q_R^\pm \varepsilon_0 - \varepsilon_Z)^2}, \tag{4.16}$$

$$E_F = \frac{\varepsilon_0}{4} + \varepsilon_0 q_L^{\pm 2} \pm \sqrt{\left(\frac{q_L^\pm \alpha}{R}\right)^2 + (q_L^\pm \varepsilon_0 + \varepsilon_Z)^2}. \tag{4.17}$$

If the Zeeman effect is negligible, then the equations (4.16) allow an analytical solution with respect to $q_{R,L}^\pm$

$$q^\pm / R = \mp \frac{m^* \alpha}{\hbar^2} \sqrt{1 + \left(\frac{\hbar^2}{2\alpha m^* R}\right)^2} + k_0. \tag{4.18}$$

Note, that the chirality index is omitted in (4.18), since $q_R^\pm = q_L^\pm$.

Imposing the boundary conditions (4.7) on the wave functions (4.8) – (4.11), (4.14) – (4.15) we get a system of eight equations (7.9) – (7.16) given in Appendix A. If one has a solution of that system with respect to $A^\pm$, $B^\pm$, $C^\pm$, $D^\pm$, then using the formulae (3.23), (3.24) and (3.25) given in Chapter 3 one can easily find the input, reflected and output current densities. The general solution obtained by *Mathematica 5.0* shows, that the transmission probability defined as $T = (j_{\text{out}}^+ + j_{\text{out}}^-)/(j_{\text{in}}^+ + j_{\text{in}}^-)$ is equal to 1, and the reflection one $R = (j_{\text{refl}}^+ + j_{\text{refl}}^-)/(j_{\text{in}}^+ + j_{\text{in}}^-)$ is zero. This means that there is no particle backscattering. However, there is a current density redistribution between j_{out}^+ and j_{out}^-, which leads to some interesting effects.

To show that, let us find the analytical solution of equations (7.9) – (7.16) in two limiting cases. First, we assume zero external magnetic field ($\varepsilon_Z = 0$, $\Phi = 0$) and a deeply adiabatic regime for the spin precession $\hbar^2/(2m^* R\alpha) \ll 1$. In this case, one can adopt $\gamma^\pm = \alpha^\pm = \beta^\pm = \pi/4$, and the equations (7.9) – (7.16) take the much simpler form

$$\left(e^{i\theta^+} + A^+\right) - i\left(e^{i\theta^-} - A^-\right) =$$
$$= e^{i\pi/4}\left(B^+ e^{-i\pi q_R^+/2} + C^+ e^{i\pi q_L^+/2} - B^- e^{-i\pi q_R^-/2} + C^- e^{i\pi q_L^-/2}\right), \tag{4.19}$$

$$\left(e^{i\theta^-} + A^-\right) - i\left(e^{i\theta^+} - A^+\right) =$$
$$= e^{-i\pi/4}\left(B^- e^{-i\pi q_R^-/2} + C^- e^{i\pi q_L^-/2} + B^+ e^{-i\pi q_R^+/2} - C^+ e^{i\pi q_L^+/2}\right), \tag{4.20}$$

$$e^{-i\pi/4}\left(B^+e^{i\pi q_R^+/2}+C^+e^{-i\pi q_L^+/2}-B^-e^{i\pi q_R^-/2}+C^-e^{-i\pi q_L^-/2}\right)=D^++iD^-, \quad (4.21)$$

$$e^{i\pi/4}\left(B^-e^{i\pi q_R^-/2}+C^-e^{-i\pi q_L^-/2}+B^+e^{i\pi q_R^+/2}-C^+e^{-i\pi q_L^+/2}\right)=D^-+iD^+, \quad (4.22)$$

$$k^+\left(e^{i\theta^+}-A^+\right)-ik^-\left(e^{i\theta^-}+A^-\right)=\frac{e^{i\pi/4}}{R}\left[B^+\left(q_R^+-\frac{1}{2}\right)e^{-i\pi q_R^+/2}-\right.$$

$$\left.-C^+\left(\frac{1}{2}+q_L^+\right)e^{i\pi q_L^+/2}-B^-\left(q_R^--\frac{1}{2}\right)e^{-i\pi q_R^-/2}-C^-\left(\frac{1}{2}+q_L^-\right)e^{i\pi q_L^-/2}\right], \quad (4.23)$$

$$k^-\left(e^{i\theta^-}-A^-\right)-ik^+\left(e^{i\theta^+}+A^+\right)=\frac{e^{-i\pi/4}}{R}\left[B^-\left(\frac{1}{2}+q_R^-\right)e^{-i\pi q_R^-/2}+\right.$$

$$\left.+C^-\left(\frac{1}{2}-q_L^-\right)e^{i\pi q_L^-/2}+B^+\left(\frac{1}{2}+q_R^+\right)e^{-i\pi q_R^+/2}-C^+\left(\frac{1}{2}-q_L^+\right)e^{i\pi q_L^+/2}\right], \quad (4.24)$$

$$\frac{1}{R}e^{-i\pi/4}\left[B^+\left(q_R^+-\frac{1}{2}\right)e^{i\pi q_R^+/2}-C^+\left(\frac{1}{2}+q_L^+\right)e^{-i\pi q_L^+/2}-\right.$$

$$\left.-B^-\left(q_R^--\frac{1}{2}\right)e^{i\pi q_R^-/2}-C^-\left(\frac{1}{2}+q_L^-\right)e^{-i\pi q_L^-/2}\right]=D^+k^++iD^-k^-, \quad (4.25)$$

$$\frac{1}{R}e^{i\pi/4}\left[B^-\left(\frac{1}{2}+q_R^-\right)e^{i\pi q_R^-/2}+C^-\left(\frac{1}{2}-q_L^-\right)e^{-i\pi q_L^-/2}+\right.$$

$$\left.+B^+\left(\frac{1}{2}+q_R^+\right)e^{i\pi q_R^+/2}-C^+\left(\frac{1}{2}-q_L^+\right)e^{-i\pi q_L^+/2}\right]=D^-k^-+iD^+k^+. \quad (4.26)$$

Note, that $k^\pm=q_R^\pm/R=q_L^\pm/R$ as long as $\hbar^2/(2m^*R\alpha)\ll 1$, as it follows from the relations (4.13), (4.18) or from the plots in fig. 2.4. Therefore, the solution of (4.19) – (4.26) is rather trivial

$$A^+=0, \quad A^-=0, \quad B^+=e^{i\theta^+-i\pi/4+i\pi q_R^+/2}, \quad B^-=e^{i\theta^-+i\pi/4+i\pi q_R^-/2},$$
$$C^+=0, \quad C^-=0, \quad D^+=-ie^{i\theta^++i\pi q_R^+}, \quad D^-=ie^{i\theta^-+i\pi q_R^-};$$

$$(4.27)$$

and, thus, $|A^+|^2=|A^-|^2=0$, $|D^+|^2=|D^-|^2=1$. Then, the current densities read

$$j_{\text{out}}^\pm=\frac{\hbar}{m^*}\left(k^\pm\pm\frac{\alpha m^*}{\hbar^2}\right), \quad j_{\text{refl}}^\pm=0; \quad (4.28)$$

and the output polarization is

$$P_{\text{out}}=\frac{k^+-k^-+2\alpha m^*/\hbar^2}{k^++k^-}. \quad (4.29)$$

Recall, that $k^--k^+=2\alpha m^*/\hbar^2$ at $B_z=0$. Thus, $P_{\text{out}}=0$ for any α.

In contrast to that, if we assume a strongly non-adiabatic regime for the spin precession so, that $\hbar^2/(2m^*R\alpha)\gg 1$, then at zero external magnetic field we still have $\gamma^\pm=\pi/4$, but $\alpha^\pm=\pi/2$ and

$\beta^{\pm} = 0$. In this case, the system of equations (7.9) – (7.16) takes the form

$$\frac{1}{\sqrt{2}}\left(e^{i\theta^+}+A^+\right)-\frac{i}{\sqrt{2}}\left(e^{i\theta^-}-A^-\right)=e^{i\pi/4}\left(C^+e^{i\pi q_L^+/2}-B^-e^{-i\pi q_R^-/2}\right), \quad (4.30)$$

$$\frac{1}{\sqrt{2}}\left(e^{i\theta^-}+A^-\right)-\frac{i}{\sqrt{2}}\left(e^{i\theta^+}-A^+\right)=e^{-i\pi/4}\left(C^-e^{i\pi q_L^-/2}+B^+e^{-i\pi q_R^+/2}\right), \quad (4.31)$$

$$e^{-i\pi/4}\left(C^+e^{-i\pi q_L^+/2}-B^-e^{i\pi q_R^-/2}\right)=\frac{1}{\sqrt{2}}D^++\frac{i}{\sqrt{2}}D^-, \quad (4.32)$$

$$e^{i\pi/4}\left(C^-e^{-i\pi q_L^-/2}+B^+e^{i\pi q_R^+/2}\right)=\frac{1}{\sqrt{2}}D^-+\frac{i}{\sqrt{2}}D^+, \quad (4.33)$$

$$\frac{1}{\sqrt{2}}k^+\left(e^{i\theta^+}-A^+\right)-\frac{i}{\sqrt{2}}k^-\left(e^{i\theta^-}+A^-\right)=$$

$$=\frac{e^{i\pi/4}}{R}\left[-C^+\left(\frac{1}{2}+q_L^+\right)e^{i\pi q_L^+/2}-B^-\left(q_R^--\frac{1}{2}\right)e^{-i\pi q_R^-/2}\right], \quad (4.34)$$

$$\frac{1}{\sqrt{2}}k^-\left(e^{i\theta^-}-A^-\right)-\frac{i}{\sqrt{2}}k^+\left(e^{i\theta^+}+A^+\right)= \quad (4.35)$$

$$=\frac{e^{-i\pi/4}}{R}\left[C^-\left(\frac{1}{2}-q_L^-\right)e^{i\pi q_L^-/2}+B^+\left(\frac{1}{2}+q_R^+\right)e^{-i\pi q_R^+/2}\right], \quad (4.36)$$

$$\frac{1}{R}e^{-i\pi/4}\left[-C^+\left(\frac{1}{2}+q_L^+\right)e^{-i\pi q_L^+/2}-B^-\left(q_R^--\frac{1}{2}\right)e^{i\pi q_R^-/2}\right]=$$

$$=\frac{1}{\sqrt{2}}D^+k^++\frac{i}{\sqrt{2}}D^-k^-, \quad (4.37)$$

$$\frac{1}{R}e^{i\pi/4}\left[C^-\left(\frac{1}{2}-q_L^-\right)e^{-i\pi q_L^-/2}+B^+\left(\frac{1}{2}+q_R^+\right)e^{i\pi q_R^+/2}\right]=$$

$$=\frac{1}{\sqrt{2}}D^-k^-+\frac{i}{\sqrt{2}}D^+k^+. \quad (4.38)$$

The approximate solution (assuming that $q^{\pm}=\mp 1/2R+k_0$, $k^{\pm}=k_0$, i. e. the characteristic spin-orbit interaction energy is much smaller than the Fermi one) reads

$$A^+=0, \quad A^-=0,$$

$$B^+=\frac{1}{\sqrt{2}}\left(e^{i\theta^-}-ie^{i\theta^+}\right)e^{\frac{i\pi}{2}\left(\frac{1}{2}+q_R^+\right)}, \quad B^-=-\frac{1}{\sqrt{2}}\left(e^{i\theta^+}-ie^{i\theta^-}\right)e^{\frac{i\pi}{2}\left(q_R^--\frac{1}{2}\right)},$$

$$C^+=0, \quad C^-=0,$$

$$D^+=\frac{e^{i\theta^-}+ie^{i\theta^+}}{2i}e^{i\pi\left(q_R^--\frac{1}{2}\right)}+\frac{e^{i\theta^-}-ie^{i\theta^+}}{2i}e^{i\pi\left(q_R^++\frac{1}{2}\right)},$$

$$D^-=\frac{e^{i\theta^-}-ie^{i\theta^+}}{2}e^{i\pi\left(q_R^++\frac{1}{2}\right)}-\frac{e^{i\theta^-}+ie^{i\theta^+}}{2}e^{i\pi\left(q_R^--\frac{1}{2}\right)}.$$

$$(4.39)$$

Thus, $|D^{\pm}|^2=1\pm\cos\left(\theta^+-\theta^-\right)\sin\left[\pi\left(q_R^--q_R^+\right)\right]$, and the spin components of the output cur-

rent density read

$$j_{\text{out}}^{\pm} = \frac{\hbar k_0}{m^*} \left\{ 1 \pm \cos\left(\theta^+ - \theta^-\right) \sin\left[\pi\left(q_R^- - q_R^+\right)\right] \right\}. \tag{4.40}$$

The spin components of the reflection current density $j_{\text{refl}}^{\pm}$ are still equal to zero. Thus, $R = 0$ and $T = 1$, whereas the output polarization reads

$$P_{\text{out}} = \cos\left(\theta^+ - \theta^-\right) \sin\left[\pi\left(q_R^- - q_R^+\right)\right]. \tag{4.41}$$

The relation (4.41) shows, that in strongly curved one-dimensional wires a current density redistribution between two spin-split modes is achievable. The results of numerical calculations at $\theta^{\pm} = 0$ are summarized in figs. 4.4, 4.5. The dependences $P_{\text{out}}(R)$ and $P_{\text{out}}(B_z)$ are given by solid curves. The dotted lines correspond to the factor (4.41). The strong correlation between the spin polarization and the interference factor is clearly visible. Nevertheless, a few words of comment are necessary here.

First, the polarization is not zero at $B_z = 0$. One can see it from the figs. 4.4, 4.5 or directly from (4.41). Second, a plot of P_{out} as a function of B_z or R yields an oscillating curve. The oscillations have a natural explanation if one follows the evolution of the wave function as a particle propagates through the wire. Namely, after the passage through the curved part of the wire, the component of the input wave function Ψ_{in}^+ propagates as a linear combination of the modes Ψ_{loop}^+ and Ψ_{loop}^- with the wave vectors q_R^+ and q_R^- respectively [see the approximate solution (4.39)]. The same is true for the propagation of the state Ψ_{in}^-. Due to the interference between two propagating states at the output of the curved part, a factor $\sin\left[\pi\left(q_R^- - q_R^+\right)\right]$ appears in the output spin polarization, which shows up as the oscillations in $P_{\text{out}}(B)$ and $P_{\text{out}}(R)$. Note, that in contrast to the system discussed in Chapter 3 there is no barrier here, and the interference factor does not appear in the transmission probability T (which is equal to 1) but in the spin-polarization P.

Now we must say a few words about the influence of the initial phase difference $\Delta\theta = \theta^- - \theta^+$ on the abovementioned effect. In general, the electron states in the reservoirs are not coherent and, therefore, the output current densities $j_{\text{out}}^{\pm}$ have to be averaged over the distribution of random initial phases $\theta^{\pm}$. In order to model the degree of decoherence we use rectangular distributions of width w, $0 \leq \theta^{\pm} \leq w$ for $\theta^{\pm}$ (see fig. 4.6). The results are summarized in figs. 4.7, 4.8. One can easily see, that an initial decoherence hampers the polarization. A tiny polarization at strong magnetic fields for the completely decoherent case is due to the Zeeman effect only.

Finally, we find it necessary to focus on the distinct features of our system that lead to the effects shown above. Let us first prove that the curvature of the one-dimensional wire itself does not lead to the current density redistribution between two spin modes. To do that, we need to modify the definition of current density (3.22) for the case of the non-symmetric Hamiltonian (4.6). The equation (3.20) has to be rewritten as

$$\frac{iR}{\hbar} \int d\varphi \left(\Psi H_{\text{loop}}^* \Psi^* - \Psi^* H_{\text{loop}} \Psi \right) = \frac{iR}{\hbar} \int d\varphi \left[\Psi_1 \left(\varepsilon_0 \hat{k}_\varphi^2 \Psi_1 \right)^* - \Psi_1^* \left(\varepsilon_0 \hat{k}_\varphi^2 \Psi_1 \right) + \right.$$

$$\left. + \Psi_1 \left(\frac{\alpha}{R} e^{-i\varphi} \hat{k}_\varphi \Psi_2 \right)^* - \Psi_1^* \left(\frac{\alpha}{R} e^{-i\varphi} \hat{k}_\varphi \Psi_2 \right) + \Psi_2 \left(\varepsilon_0 \hat{k}_\varphi^2 \Psi_2 \right)^* - \Psi_2^* \left(\varepsilon_0 \hat{k}_\varphi^2 \Psi_2 \right) + \right.$$

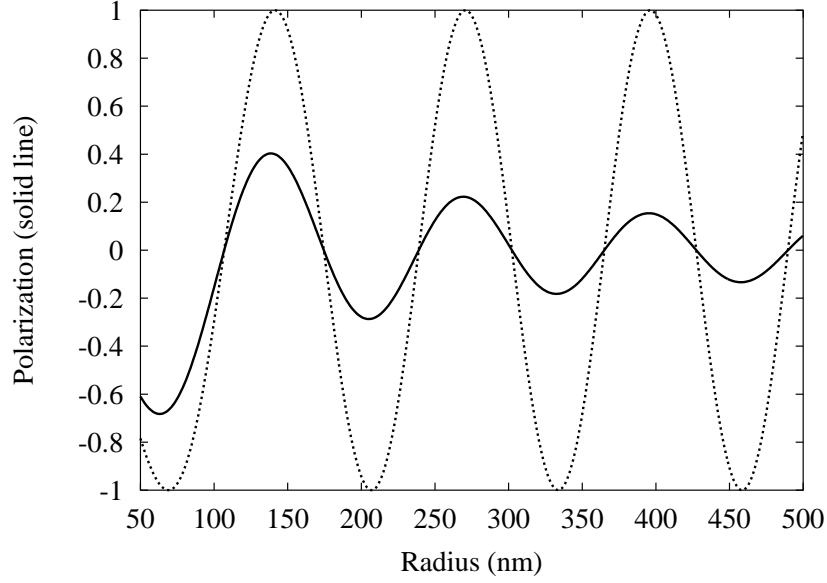Figure 4.4: Polarization (solid line) versus radius of the semi-circle at $B_z = 0$. The interference factor $\sin\left[\pi(q_R^- - q_R^+)\right]$ is depicted by the dashed line. The initial phases $\theta^\pm$ both are equal to zero, $P_{\mathrm{in}} = 0$, and the other parameters are taken relevant for InAs: $\alpha = 2 \cdot 10^{-11}\,\mathrm{eVm}$, $m^* = 0.033 m_e$, $g^* = -12$, $E_F = 30\,\mathrm{meV}$.

$$
+\Psi_2 \left(\frac{\alpha}{R}\mathrm{e}^{i\varphi}\hat{k}_\varphi\Psi_1\right)^* - \Psi_2^* \left(\frac{\alpha}{R}\mathrm{e}^{i\varphi}\hat{k}_\varphi\Psi_1\right) - \mathrm{e}^{i\varphi}\Psi_2^*\Psi_1 + \mathrm{e}^{-i\varphi}\Psi_1^*\Psi_2 \Bigg]. \tag{4.42}
$$

Note, that in contrast to (3.20) the additional $\mathrm{e}^{\pm i\varphi}$–dependent terms occur. The formula for current densities in a curved wire is, therefore, more complicated than the previous one for the straight channel (3.22). Using the continuity equation (3.18) we arrive (after some algebra) at the following relation for $\mathbf{j}$

$$
\mathbf{j} = \frac{R\varepsilon_0}{\hbar}\left(\Psi_1\hat{k}_\varphi^*\Psi_1^* + \Psi_1^*\hat{k}_\varphi\Psi_1 + \Psi_2\hat{k}_\varphi^*\Psi_2^* + \Psi_2^*\hat{k}_\varphi\Psi_2\right) +
$$

$$
+\frac{\alpha}{\hbar}\left(\Psi_1\Psi_2^*\mathrm{e}^{i\varphi} - \Psi_1^*\Psi_2\mathrm{e}^{-i\varphi}\right). \tag{4.43}
$$

Now, let us apply formula (4.43) to the spinors (4.14) and (4.15) which describe the spin-split states in the curved part of the wire. Straightforward calculations lead to the following formula for right-moving current densities

$$
j_{\mathrm{loop}}^\pm = |B^\pm|^2\frac{\hbar}{m^*}\left[\frac{q_R^\pm}{R} \pm \frac{m^*\alpha}{\hbar^2}\left(\sin 2\alpha^\pm - \frac{\hbar^2}{2R\alpha m^*}\cos 2\alpha^\pm\right)\right]. \tag{4.44}
$$

Equation (4.44) is still not very clear since it contains the Zeeman effect which can lead to a tiny polarization and, therefore, diminish the obviousness of the picture. Thus, we set $\varepsilon_Z = 0$
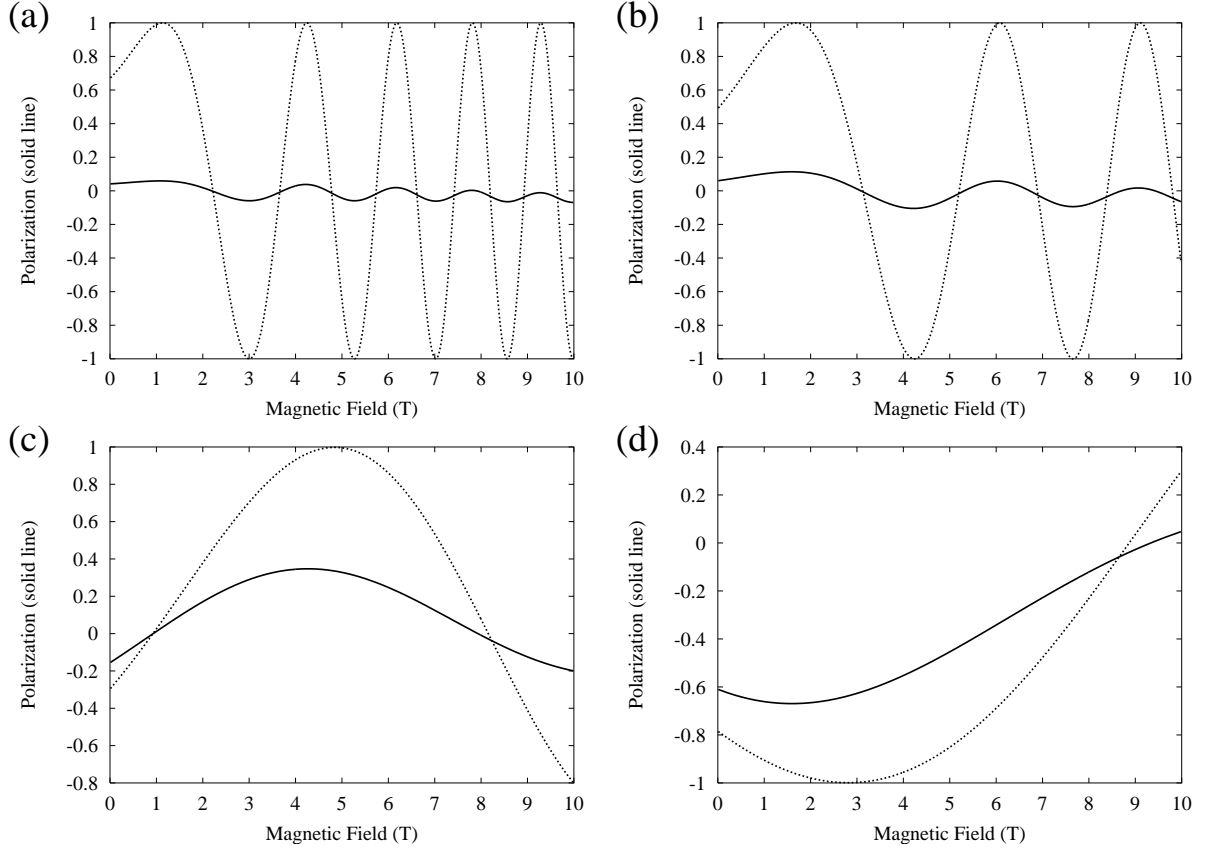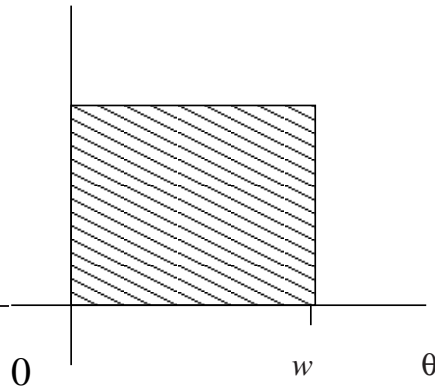
Figure 4.5: Polarization (solid lines) and interference factor $\sin\left[\pi(q_R^- - q_R^+)\right]$ (dashed lines) versus external magnetic field at different radii of the semi-circle: (a) $R = 10^{-4}$cm, (b) $R = 5 \cdot 10^{-5}$cm, (c) $R = 10^{-5}$cm, (d) $R = 5 \cdot 10^{-6}$cm. The input current is spin-unpolarized. The initial phases $\theta^\pm$ both are equal to zero, and the other parameters are taken relevant for InAs: $\alpha = 2 \cdot 10^{-11}$eVm, $m^* = 0.033m_e$, $g^* = -12$, $E_F = 30$meV.

Figure 4.6: The rectangular distribution for $\theta^\pm$ used for decoherence simulations.
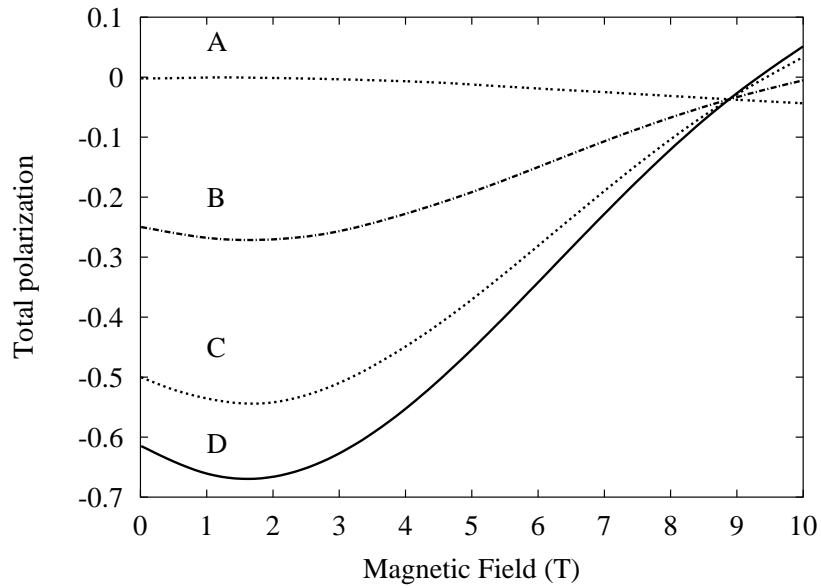
Figure 4.7: Total polarization vs. magnetic field for different distribution width $w = \max\{\theta^{\pm}\}$ that corresponds to the different degree of decoherence. Curve (A) $w = 2\pi$ (completely decoherent states), (B) $w = \pi$, (C) $w = \pi/2$, (D) $w = 0$ (completely coherent states). The radius of the semi-circle is taken as $5 \cdot 10^{-6}$ cm, the other parameters are the same as for previous figures.
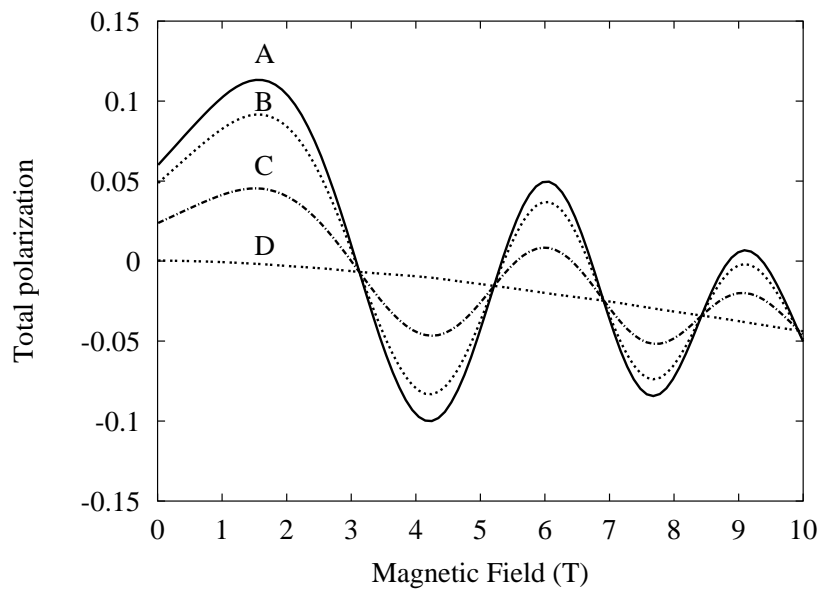

Figure 4.8: Total polarization vs. magnetic field for different distribution width $w = \max\{\theta^{\pm}\}$. The radius of the semi-circle is taken ten times smaller ($5 \cdot 10^{-5}$cm) than for the previous figure. Curve (A) $w = 0$ (completely coherent states), (B) $w = \pi/2$, (C) $w = \pi$, (D) $w = 2\pi$ (completely decoherent states).

and study the interplay of spin-orbit coupling and non-zero curvature without additional Zeeman spin-splitting. As soon as $\varepsilon_Z = 0$, we have immediately from (3.12)

$$\tan 2\alpha^+ = \tan 2\alpha^- = -\frac{2\alpha m^* R}{\hbar^2}. \tag{4.45}$$

Then, using the general trigonometric relation

$$a\sin\alpha + b\cos\alpha = \sqrt{a^2 + b^2}\sin\left(\alpha + \text{arctg}\frac{b}{a}\right), \tag{4.46}$$

(where $a > 0$) we arrive at the next formula for $j_{\text{loop}}^{\pm}$ for $B_z = 0$

$$j_{\text{loop}}^{\pm} = |B^{\pm}|^2 \frac{\hbar}{m^*}\left\{\frac{q_R^{\pm}}{R} \pm \frac{m^*\alpha}{\hbar^2}\sqrt{1 + \left(\frac{\hbar^2}{2m^*\alpha R}\right)^2}\sin\left[2\alpha^{\pm} + \text{arctg}\left(\cot 2\alpha^{\pm}\right)\right]\right\}. \tag{4.47}$$

Notice, it is easy to check that $\sin\left[2\alpha^{\pm} + \text{arctg}\left(\cot 2\alpha^{\pm}\right)\right] = 1$. Now, adopting the relations (4.18) for $q_R^{\pm}$, we get

$$j_{\text{loop}}^{\pm} = |B^{\pm}|^2 \frac{\hbar k_0}{m^*}, \tag{4.48}$$

and

$$P_{\text{loop}} = \frac{|B^+|^2 - |B^-|^2}{|B^+|^2 + |B^-|^2}. \tag{4.49}$$

Note, that P_{loop} depends only on the transmission amplitudes $B^{\pm}$, i. e. on the properties of the junction between the regions with different curvature. Let us find $|B^{\pm}|^2$ explicitly from (4.39). Straightforward calculations lead to $|B^{\pm}|^2 = 1 \pm \sin\left(\theta^+ - \theta^-\right)$ and the polarization reads

$$P_{\text{loop}} = \sin\left(\theta^+ - \theta^-\right). \tag{4.50}$$

As one can see from this formula, the current density polarization in the curved part of the system depends only on the phase difference of the initial states. Thus, these initial states must be specially prepared in order to observe the factor (4.50) in the polarization measurements. If the phase difference $\theta^+ - \theta^-$ is not fixed in the electron beam (or just equal to zero), then the observed polarization is zero.

We would like to emphasize, that the current density redistribution between the two spin-split modes in the curved part of the wire does not stem from the finite curvature itself. In contrast, the *change* of curvature gives rise to the difference between the amplitudes $|B^+|^2$ and $|B^-|^2$ (or $|D^+|^2$ and $|D^-|^2$) and, therefore, leads to the current density redistribution between the two spin-split modes. Indeed, consider the electron momenta at the Fermi level for the straight and curved regions of the wire in the simplest case of zero external magnetic field. The momenta $k^{\pm}$ and $q^{\pm}/R$ are given by (4.13) and (4.18) respectively. The essential difference between the electron momenta for the straight wire and the loop lies in the radius dependent term $\hbar^2/(2\alpha m^* R)$ in $q^{\pm}/R$. Notice, that $k^{\pm} = q^{\pm}/R$ if $R = \infty$ (no wire bending). In contrast, q^+/R *decreases* (as
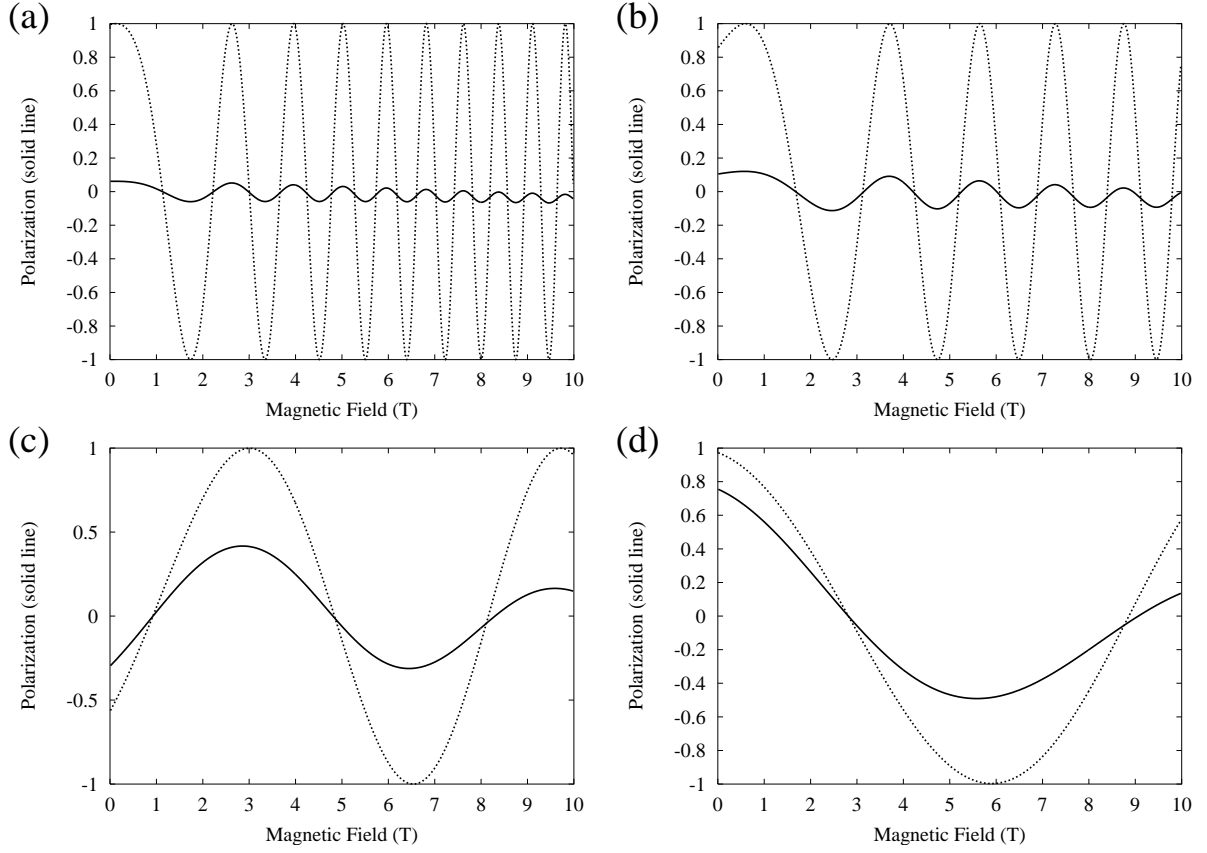
Figure 4.9: The output polarization using the geometry of a *complete* loop shown in fig. 3.1: polarization (solid line) and the interference factor $\sin\left[2\pi\left(q_R^- - q_R^+\right)\right]$ (dashed line) versus magnetic field. The radius of the loop is taken as (a) 10^{-4}cm, (b) $5\cdot10^{-5}$cm, (c) 10^{-5}cm and (d) $5\cdot10^{-6}$cm. The parameters are taken relevant for InAs, the height of the barrier is zero.

compared with k^+) and q^-/R *increases* (as compared with k^-) as long as the loop goes towards a kink of the wire at $R \to 0$. For all that, the Fermi velocity $v_F = \hbar^2 k_0/m^*$ keeps the same value in any part of the system, and the electron momentum changes in the curved part of the wire in such a way, that *forward* scattering from one spin-split mode to another occurs. The latter leads to the interference between them and shows up as the current density redistribution between j_{out}^+ and j_{out}^-. One can think about the wire bending as a changing of the initial Rashba parameter α to $\alpha\sqrt{1 + \left[\hbar^2/(2\alpha m^* R)\right]^2}$ in the loop region. Note, however, that in contrast to the actual change of α, the change of the wire's curvature does not affect the electron density of states and results directly in the difference between q^+ and q^- so, that there is no problem with reflection. This is a very particular property of the system: there is no barrier at the junction between the straight and curved parts of the wire, but the Fermi momenta jump, and, thus, the current density redistribution between the spin-split modes takes place.

At the end of this section we would like to note, that a similar effect can be found in one-dimensional wires bent into a loop as well. Such a quantum loop has been studied in the previous

Chapter and shown in fig. 3.1. The output polarization of such a system at $P_{\text{in}} = 0$ is depicted in fig. 4.9.

The results obtained suggest that curved one-dimensional ballistic quantum wires with intrinsic spin-orbit interactions can be utilized in spintronic devices as reflectionless spin rotators. The phase coherence of electron states is, however, necessary.

4.3 Curved 1D wire as a spin switch

In this section we propose to use a strongly curved 1D wire discussed above as a spin switch. In contrast to the previous case, the phase coherence of electron states is not necessary here. Now, the initial state $\Psi_{\text{in}}^+(x)$ in the input wire is given by

$$\Psi_{\text{in}}^+(x) = e^{\frac{i\Phi}{\Phi_0 R}x} \left(\begin{array}{c} \cos\gamma^+ \left(e^{i\theta^+ + ik^+x} + A^+ e^{-ik^+x} \right) \\ -i\sin\gamma^+ \left(e^{i\theta^+ + ik^+x} - A^+ e^{-ik^+x} \right) \end{array} \right), \tag{4.51}$$

whereas the incident wave is absent in the spinor $\Psi_{\text{in}}^-(x)$

$$\Psi_{\text{in}}^-(x) = e^{\frac{i\Phi}{\Phi_0 R}x} \left(\begin{array}{c} i\sin\gamma^- A^- e^{-ik^-x} \\ \cos\gamma^- A^- e^{-ik^-x} \end{array} \right). \tag{4.52}$$

Thus, the input spin polarization P_{in} is assumed to be 1, i. e. the incident electron beam is 100% left-hand polarized (at $B_z = 0$).

The wave functions $\Psi_{\text{loop}}^\pm(\varphi)$ and $\Psi_{\text{out}}^\pm(x)$ describing the electron propagation through the curved and output parts of the the system are the same as in the previous case. The system of equations (7.17) – (7.24) describing the propagation of the state (4.51) through the curved wire is given in Appendix A.

The general solution of the system of equations (7.17) – (7.24) obtained by *Mathematica 5.0* is used for plotting the curves in figs. 4.10 – 4.12. This solution demonstrates zero backscattering ($R = 0$ and $T = 1$), while the polarization curves exhibit the following interesting features: First, the plots of $P_{\text{out}}(B_z)$ and $P_{\text{out}}(R)$ yield oscillating curves. Second, the efficiency of the spin-switching depends strongly on the direction of the external magnetic field. Third, although the polarization can be switched to its opposite value at $B_z = 0$, a relatively small radius of the wire's curvature is necessary. In order to explain the features listed above, we solve the system (7.17) – (7.24) in two cases again: the deeply adiabatic $\hbar^2/(2m^*R\alpha) \ll 1$ and the strongly non-adiabatic $\hbar^2/(2m^*R\alpha) \gg 1$ limits.

The first limit is, however, not really interesting. As in the previous section, no current density redistribution between the two spin-split modes occurs here, i. e. $|D^+|^2 = 1$ and $|D^-|^2 = 0$. Intuitively it is clear, that the curved wire does not differ too much from the straight one as long as $\hbar^2/(2m^*R\alpha) \ll 1$. Therefore, the polarization keeps its +100% initial value while the current flows through the system.
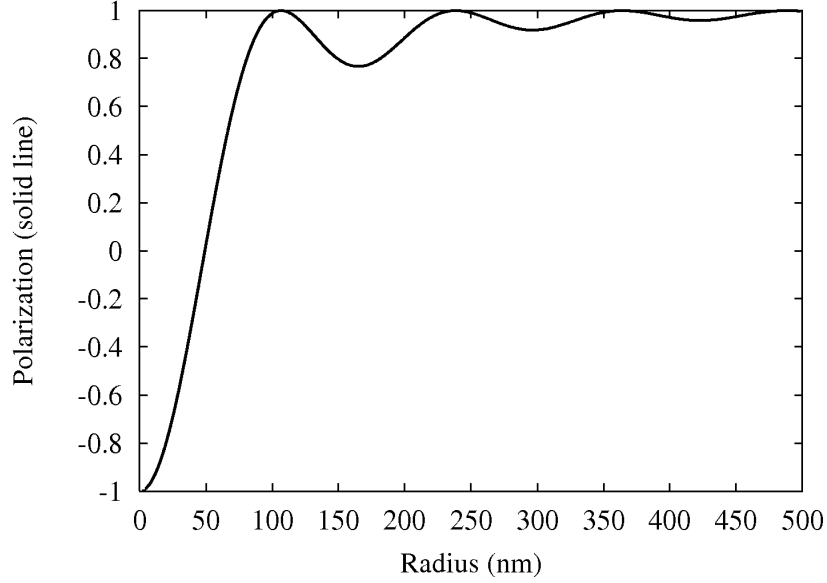
Figure 4.10: The curved wire as a spin switch: Polarization versus radius of the semi-circle at zero magnetic field. The initial polarization is $+100\%$. The parameters are taken relevant for *InAs*: $\alpha = 2 \cdot 10^{-11}$ eVm, $m^* = 0.033 m_e$, $g^* = -12$, $E_F = 30$ meV.

In the opposite, strongly non-adiabatic limit, the situation changes drastically. Indeed, the system of equations (7.17) – (7.24) at $\alpha^\pm = \pi/2$, $\beta^\pm = 0$ and zero magnetic field reads

$$\frac{1}{\sqrt{2}}\left(e^{i\theta^+} + A^+\right) + \frac{i}{\sqrt{2}}A^- = C^+ e^{-\frac{i\pi}{2}\left(-q_L^+ - \frac{1}{2}\right)} - B^- e^{-\frac{i\pi}{2}\left(q_R^- - \frac{1}{2}\right)}, \qquad (4.53)$$

$$\frac{1}{\sqrt{2}}A^- - \frac{i}{\sqrt{2}}\left(e^{i\theta^+} - A^+\right) = C^- e^{-\frac{i\pi}{2}\left(\frac{1}{2} - q_L^-\right)} + B^+ e^{-\frac{i\pi}{2}\left(\frac{1}{2} + q_R^+\right)}, \qquad (4.54)$$

$$C^+ e^{\frac{i\pi}{2}\left(-q_L^+ - \frac{1}{2}\right)} - B^- e^{\frac{i\pi}{2}\left(q_R^- - \frac{1}{2}\right)} = \frac{1}{\sqrt{2}}D^+ + \frac{i}{\sqrt{2}}D^-, \qquad (4.55)$$

$$C^- e^{\frac{i\pi}{2}\left(-q_L^- + \frac{1}{2}\right)} + B^+ e^{\frac{i\pi}{2}\left(q_R^+ + \frac{1}{2}\right)} = \frac{1}{\sqrt{2}}D^- + \frac{i}{\sqrt{2}}D^+, \qquad (4.56)$$

$$\frac{1}{\sqrt{2}}k^+\left(e^{i\theta^+} - A^+\right) - \frac{i}{\sqrt{2}}k^- A^- =$$

$$= \frac{e^{i\pi/4}}{R}\left[-C^+\left(\frac{1}{2} + q_L^+\right)e^{i\pi q_L^+/2} - B^-\left(q_R^- - \frac{1}{2}\right)e^{-i\pi q_R^-/2}\right], \qquad (4.57)$$

$$-\frac{1}{\sqrt{2}}k^- A^- - \frac{i}{\sqrt{2}}k^+\left(e^{i\theta^+} + A^+\right) =$$

$$= \frac{e^{-i\pi/4}}{R}\left[C^-\left(\frac{1}{2} - q_L^-\right)e^{i\pi q_L^-/2} + B^+\left(\frac{1}{2} + q_R^+\right)e^{-i\pi q_R^+/2}\right], \qquad (4.58)$$
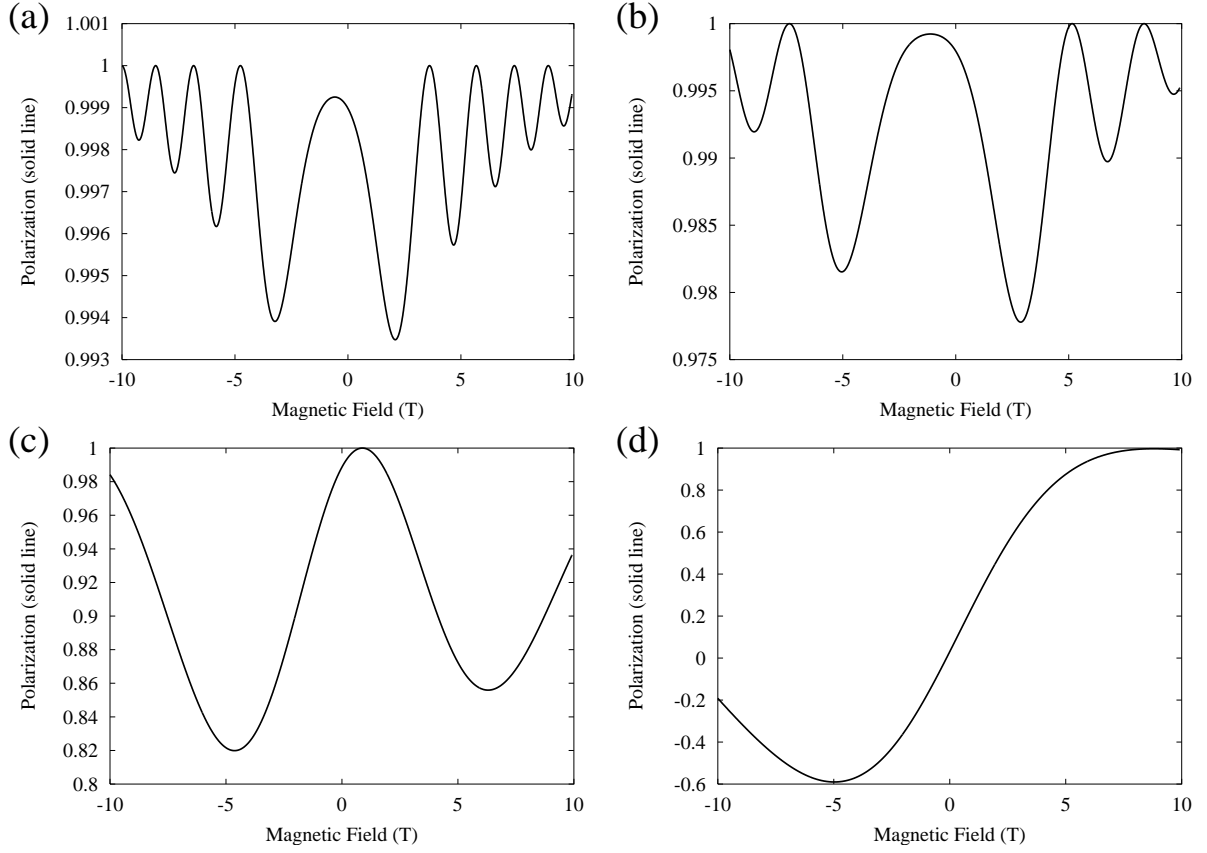
68

Figure 4.11: Spin switching by propagation through a strongly curved wire placed in a magnetic field perpendicular to the loop plane. Polarization P_{out} versus magnetic field. The initial polarization is taken $+100\%$. Radius of the semicircle: (a) 10^{-4}cm, (b) $5 \cdot 10^{-5}$cm, (c) 10^{-5}cm and (d) $5 \cdot 10^{-6}$cm. The other parameters are the same as for the previous figure (non-adiabatic regime).

$$\frac{1}{R}\mathrm{e}^{-i\pi/4}\left[-C^+\left(\frac{1}{2}+q_L^+\right)\mathrm{e}^{-i\pi q_L^+/2}-B^-\left(q_R^--\frac{1}{2}\right)\mathrm{e}^{i\pi q_R^-/2}\right]=$$
$$=\frac{1}{\sqrt{2}}D^+k^++\frac{i}{\sqrt{2}}D^-k^-, \tag{4.59}$$

$$\frac{1}{R}\mathrm{e}^{i\pi/4}\left[C^-\left(\frac{1}{2}-q_L^-\right)\mathrm{e}^{-i\pi q_L^-/2}+B^+\left(\frac{1}{2}+q_R^+\right)\mathrm{e}^{i\pi q_R^+/2}\right]=$$
$$=\frac{1}{\sqrt{2}}D^-k^-+\frac{i}{\sqrt{2}}D^+k^+. \tag{4.60}$$

The approximate solution of this system reads

$$A^+=0,\quad A^-=0,$$
$$B^+=-\frac{i}{\sqrt{2}}\mathrm{e}^{i\theta^++\frac{i\pi}{2}\left(\frac{1}{2}+q_R^+\right)},\quad B^-=-\frac{1}{\sqrt{2}}\mathrm{e}^{i\theta^++\frac{i\pi}{2}\left(q_R^--\frac{1}{2}\right)},$$
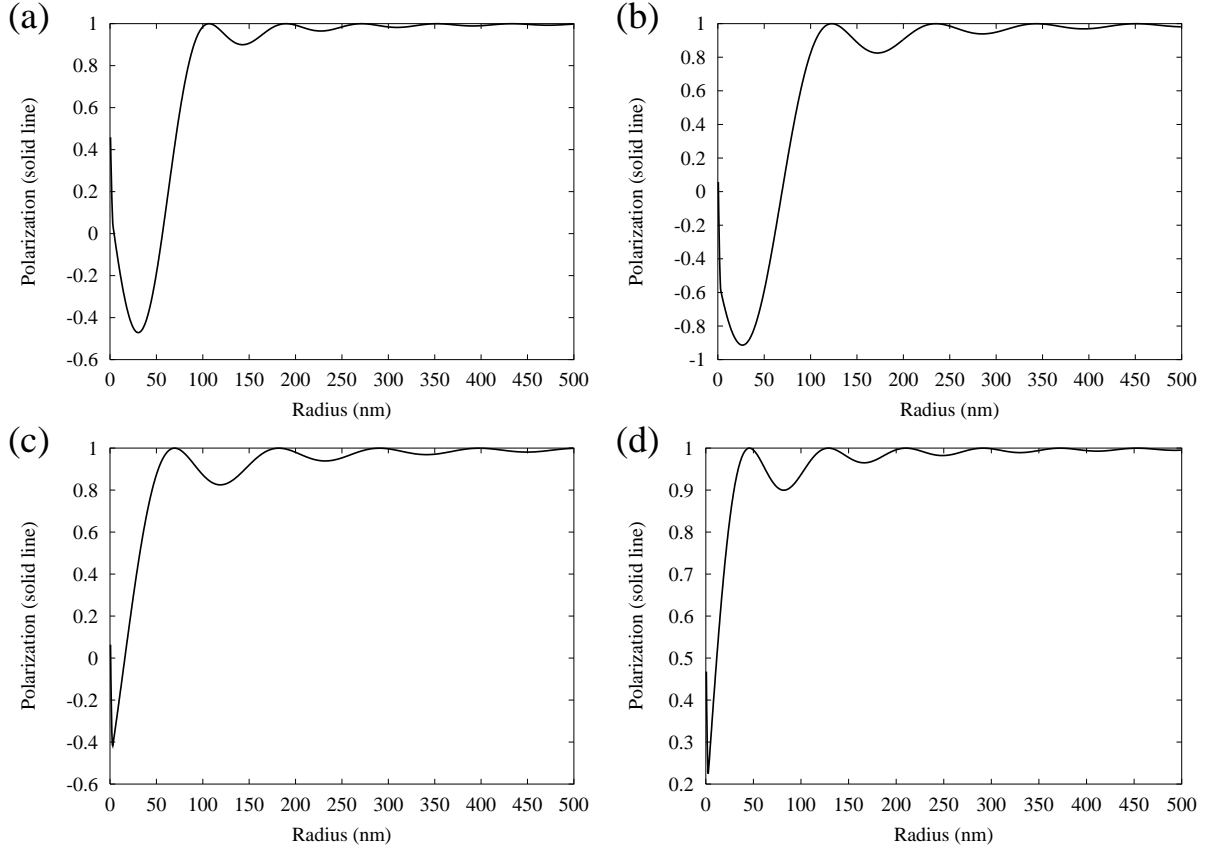
$$\tag{4.61}$$

Figure 4.12: Spin switching by means of a strongly curved wire placed in a magnetic field perpendicular to the semicircle plane. Polarization P_{out} versus radius of the semi-circle. The initial polarization is taken +100%. The external magnetic field is taken as: (a) -10T, (b) -5T, (c) $+5$T and (d) $+10$T. The other parameters are the same as for the previous figures. Note, that polarization is very sensitive to the sign of the magnetic field.

$$C^+ = 0, \quad C^- = 0,$$
$$D^+ = \frac{1}{2} e^{i\theta^+} \left[e^{i\pi\left(q_R^- - \frac{1}{2}\right)} - e^{i\pi\left(q_R^+ + \frac{1}{2}\right)} \right], \quad D^- = \frac{1}{2i} e^{i\theta^+} \left[e^{i\pi\left(q_R^- - \frac{1}{2}\right)} + e^{i\pi\left(q_R^+ + \frac{1}{2}\right)} \right].$$

$$(4.62)$$

(Here, we assume the same approximations as in the previous section for (4.62), namely: $q^{\pm} = \mp 1/2R + k_0$, $k^{\pm} = k_0$.) Then,

$$|D^{\pm}|^2 = \frac{1}{2} \pm \frac{1}{2} \cos\left[\pi \left(q_R^+ - q_R^- \right) \right],$$

and the spin components of the output current density read

$$j_{\text{out}}^{\pm} = \frac{\hbar k_0}{2m^*} \left\{ 1 \pm \cos\left[\pi \left(q_R^- - q_R^+ \right) \right] \right\}.$$
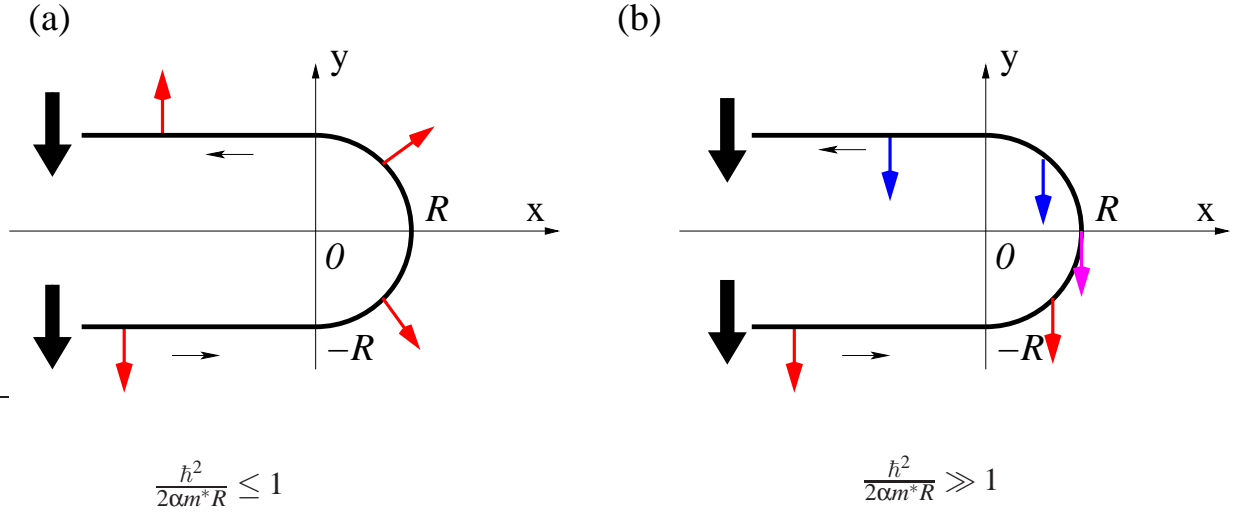
$$(4.63)$$

Figure 4.13: Schematics of the spin field effect transistor based on strongly curved one-dimensional wires with spin-orbit coupling. The thick arrows depict the spin orientation in the polariser and analyser. (a) The system is closed. (b) The system is opened.

Thus, in the strongly non-adiabatic regime current density redistribution occurs, and the polarization is

$$P_{\text{out}} = \cos\left[\pi\left(q_R^- - q_R^+\right)\right]. \tag{4.64}$$

Note, that if the radius of the curvature is *exactly* equal to zero, then the difference between the Fermi angular momenta reads

$$q_R^- - q_R^+ = \left.\frac{2m^*R\alpha}{\hbar^2}\sqrt{1 + \left(\frac{\hbar^2}{2\alpha m^*R}\right)^2}\right|_{R=0} = 1. \tag{4.65}$$

Thus, the output polarization $P_{\text{out}} = -1$, whereas the initial one was $P_{\text{in}} = +1$. Therefore, the polarization is switched to its opposite value as expected for the case of zero radius. (The explanation of this effect was given in the introductory section of this Chapter.)

The difference between the Fermi angular momenta q_R^- and q_R^+ depends not only on the Rashba coupling and radius of the semi-circle, but on the Zeeman splitting as well. Therefore, the critical values of $q_R^- - q_R^+$, when the polarization P_{out} changes the sign, are tunable by means of the external magnetic field. Unfortunately, we do not have analytical formulae for $q_{R,L}^\pm$ at non-zero magnetic fields, but one can see the effect in figs. 4.11, 4.12. The most interesting of them are the figs. 4.11d, 4.12b where almost -100% output spin polarization is achieved at non-zero radius of the curvature.

Such a spin-switch can be used in spin-valves or spin field effect transistors similar to the ones described in Chapter 2, figs. 2.8, 2.9. To complete the spin field effect transistor we assume a spin polarizer and a spin analyzer at the ends of the input and output channels. For the sake of simplicity, let the spin polarizer and spin analyzer be transparent for the same spin orientation
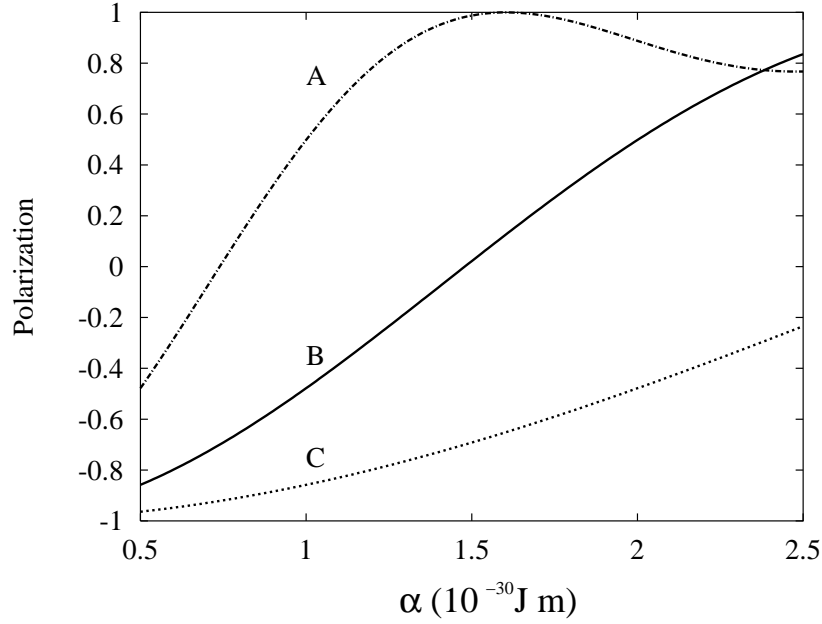
Figure 4.14: Polarization P_{out} versus Rashba constant α at zero external magnetic field. The input polarization is $P_{\text{in}} = 1$, $m^* = 0.033m_e$, $E_F = 30$meV, and the radius of curvature is (A) $R = 2 \cdot 10^{-5}$cm, (B) $R = 10^{-5}$cm, (c) $R = 5 \cdot 10^{-6}$cm. Such values of α and R are achievable experimentally in InAs [8, 11, 92].

as it is shown in fig. 4.13. The basic principle of the device proposed is similar to the "conventional" one. The transistor is closed as long as the transport regime is adiabatic $\hbar^2/(2\alpha m^* R) \leq 1$, and the electron spin changes its orientation with respect to the spin-orientation in the contacts (fig. 4.13a). In contrast, the spin-switching occurs as soon as the electron spin does not have enough time to follow the electron trajectory (the non-adiabatic regime, fig. 4.13b). Thus, the spin-valve is opened when $\hbar^2/(2\alpha m^* R) \gg 1$. The relation $\hbar^2/(2\alpha m^* R)$ can be tuned by the gate-voltage dependent Rashba constant α as it is discussed in [8, 11]. The plots of $P_{\text{out}}(\alpha, P_{\text{in}} = 1)$ are shown in fig. 4.14 for different radii of curvature. The values of α are taken in accordance with the experimental situation in InAs [8, 11].

In contrast to the "conventional" spin-rotators made of straight semiconductor stripes, the device proposed is expected to operate faster since it works in the non-adiabatic regime. Indeed, the switching speed is determined by the time needed for an electron to propagate through the curved part of the system which can be very short as long as our device is in the non-adiabatic regime $\hbar^2/(2\alpha m^* R) \gg 1$. Thus, the switching time can be even smaller than the one estimated in the Introduction for, let us say, a "conventional" spintronic device in the adiabatic regime.

In conclusion of this Chapter, we propose a semiconductor structure that can switch the electron spin direction without using ferromagnetic contacts, tunneling barriers, external radiation etc. Moreover, the alteration can be governed by external electric or magnetic fields. The results obtained suggest that curved 1D ballistic quantum wires with intrinsic spin-orbit interactions can be

utilized in spintronic devices as reflectionless spin switchers. Calculations based on typical parameters for InAs show that the desired regime is accessible for current experimental techniques [92]. Note, that the initial left- or right-hand spin-polarized electron beam in InAs quantum wires can be obtained by applying circularly polarized radiation [49, 61].

5 The properties of the asymmetric Tomonaga-Luttinger liquid

In this Chapter, we describe a particular one-dimensional system, where the Fermi velocities (as well as the densities of states) for left- and right-moving electrons are not equal to each other. Such a system can be formed in an isolated quantum loop with spin-orbit coupling placed into a magnetic field perpendicular to the loop plane. The Tomonaga-Luttinger model is applied in order to describe the influence of electron-electron interactions on the chiral asymmetry of the density of states. We find, that electron-electron interactions lead to an alignment of the density of states for the left- and right- moving electrons. In addition, the possible manifestation of the chiral asymmetry in ballistic transport phenomena is discussed.

5.1 Interplay between Rashba and Zeeman effect in curved one-dimensional wires

It is well known, that the electron spectrum in 1D systems without spin-orbit interactions and Zeeman effect demonstrates spatial inversion symmetry $E^\sigma(k) = E^\sigma(-k)$ as well as time inversion symmetry $E^\sigma(k) = E^{-\sigma}(-k)$. (Here σ and k are the spin and orbital quantum numbers respectively.) The spin-orbit coupling as well as Zeeman effect splits every electron spin-degenerate energy band into two branches corresponding to the spin-up and spin-down projections on a certain axis. In detail, the Rashba effect shifts the dispersion curves along the momentum axis (let us say, spin-up band is moving to the right and spin-down one to the left), whereas the Zeeman term splits them along the energy axis. As a consequence, the spatial and time inversion symmentry can be broken.

Actually, the space and time inversion asymmetry in the dispersion law stems from three factors: (i) the presence of spin-orbit interactions, which break the spatial inversion symmetry, (ii) the Zeeman effect, which breaks the time inversion symmetry, and (iii) a non-zero curvature of the wire, which makes possible the manifestation of both space and time inversion asymmetry in the electron spectrum.

Indeed, let us have a precise look on the dispersion law for the electrons in a curved 1D wire with Rashba spin-orbit coupling placed in a magnetic field perpendicular to the plane as it is depicted in fig. 2.2b. If the radius of curvature is constant and equal to R, then the energy spectrum reads

$$\frac{E^\pm(q)}{\varepsilon_0} = q^2 + \frac{1}{4} \pm \sqrt{\frac{\alpha^2}{\varepsilon_0^2 R^2} q^2 + \left(q - \frac{\varepsilon_Z}{\varepsilon_0}\right)^2}, \tag{5.1}$$

where $q \in (-\infty, \infty)$ is the angular momentum, ε_Z is the Zeeman energy, and $\varepsilon_0 = \hbar^2/(2m^*R^2)$. The dispersion law (5.1) has a peculiar property:

$$E^\sigma(q) \neq E^\sigma(-q), \quad E^\sigma(q) \neq E^{-\sigma}(-q), \tag{5.2}$$

i. e. both spatial and time inversion symmetries are broken.

If the Zeeman effect is absent then the dispersion law takes the form

$$\frac{E^\pm(q)}{\varepsilon_0} = \left(q \pm \frac{1}{2} \sqrt{\frac{\alpha^2}{\varepsilon_0^2 R^2} + 1} \right)^2 - \frac{\alpha^2}{4\varepsilon_0^2 R^2}. \tag{5.3}$$

Here, $E^\sigma(q) = E^{-\sigma}(-q)$ and $E^\sigma(q) \neq E^\sigma(-q)$, i. e. the spatial inversion symmetry is broken, while the time inversion symmetry is kept. Note, that the spectrum (5.3) coincides with the dispersion law for a straight 1D quantum wire (of the length $2\pi R$) at $\alpha/\varepsilon_0 R >> 1$. In the opposite case of vanishing Rashba coupling and non-zero Zeeman splitting the spectrum is

$$\frac{E^\pm(q)}{\varepsilon_0} = q^2 \pm \frac{\varepsilon_Z}{\varepsilon_0}. \tag{5.4}$$

Here the spatial inversion symmetry is kept, while the time inversion symmetry is broken.

Note, that the notations $\pm$ in the formulae (5.3) and (5.4) correspond to spin projections "up" and "down" on different axis, namely, on the radial axis for (5.3) and on the polar one for (5.4). Moreover, due to the coupling between the Rashba and Zeeman effects a rotation of the spin quantization axis occurs and, therefore, the sign $\pm$ in (5.1) does not have the sense of spin projections on z or r axes.

If we have both Zeeman effect and Rashba spin-orbit coupling, but the wire is not curved, then the spatial inversion symmetry is recovered, as it can be seen from the spectrum

$$E^\pm(k) = \frac{\hbar^2 k^2}{2m^*} \pm \sqrt{\alpha^2 k^2 + \varepsilon_Z^2}. \tag{5.5}$$

Thus, it is only if all the three abovementioned conditions are fulfilled that both time and spatial inversion symmetries are broken.

The time and spatial inversion asymmetry gives rise to some interesting effects. First, the Fermi momenta for right- and left-moving electrons of the same branch are not equal anymore. Such an asymmetry leads, in particular, to the Aharonov-Anandan phase discussed in the Chapter 3. Second, the Fermi velocities are different for electrons with opposite chiralities (see fig. 5.1), which leads to a chiral asymmetry of the density of states. This peculiarity of curved 1D wires with Zeeman effect and Rashba coupling will be studied in the present Chapter.

5.2 Solution of the asymmetric Tomonaga-Luttinger model

The one-partical solution of Schrödinger's equation for a quantum loop shows, that the Fermi velocities (and, therefore, the densities of states) for left- and right-moving electrons are not equal.
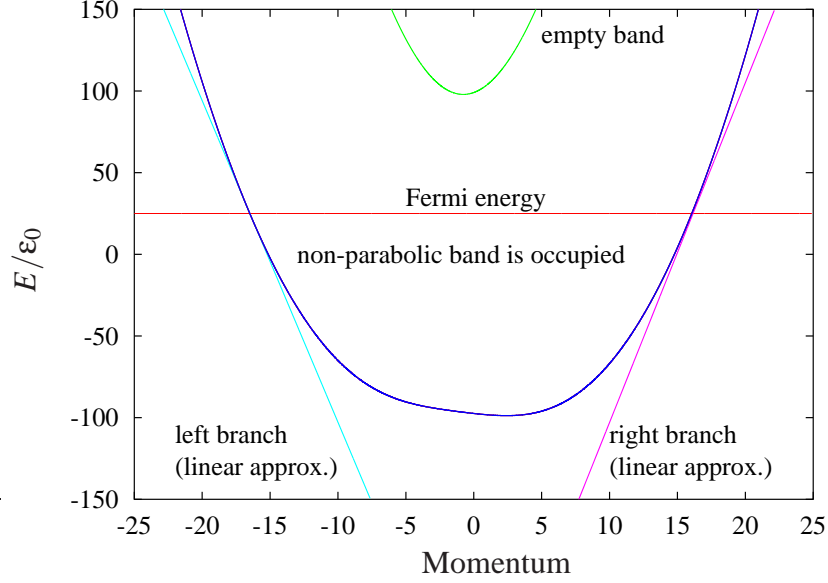
Figure 5.1: Dispersion law for free electrons in a 1D loop with Rashba coupling, placed into a perpendicular magnetic field. The asymmetry of the parabola is clearly visible. The straight lines on the left and right sides are the linear approximations of the dispersion curves close to Fermi the points. The parameters are taken relevant for InAs: $\alpha = 2 \cdot 10^{-11}$ eVm, $m^* = 0.033 m_e$, $g^* = -12$. The radius of the loop is $5 \cdot 10^{-5}$cm, external magnetic field is 1.3T, and the Fermi level is chosen so, that only a single subband is occupied.

The question is what happens with the density of states if the electron-electron interactions are switched on? We give the answer in the framework of the Tomonaga-Luttinger model, assuming that only a single subband is occupied as it is shown in fig. 5.1.

We begin by linearizing the dispersion law for the lowest band close to the Fermi points as it is depicted in fig. 5.1. The expansion reads

$$E_{L/R}^{-}(q) = E_F \mp \frac{\hbar v_{L/R}^{-}}{R}\left(q - q_{L/R}^{-}\right). \tag{5.6}$$

The Fermi velocities can be found from

$$v_{L/R}^{-} = \frac{\varepsilon_0 R}{\hbar}\left[2q_{L/R}^{-} - \frac{q_{L/R}^{-} + \frac{\alpha^2}{\varepsilon_0^2 R^2}q_{L/R}^{-} \pm \varepsilon_Z/\varepsilon_0}{\sqrt{\left(\frac{\alpha q_{L/R}^{-}}{\varepsilon_0 R}\right)^2 + \left(q_{L/R}^{-} \pm \varepsilon_Z/\varepsilon_0\right)^2}}\right]. \tag{5.7}$$

The Fermi angular momenta $q_{L/R}^{-}$ are the roots of equations (4.16), (4.17) taken with the index "$-$". Unfortunately, these equations do not allow reasonable analytical solutions with respect to q at $\varepsilon_Z \neq 0$. However, a numerical treatment is applicable, and the Fermi velocities (5.7)
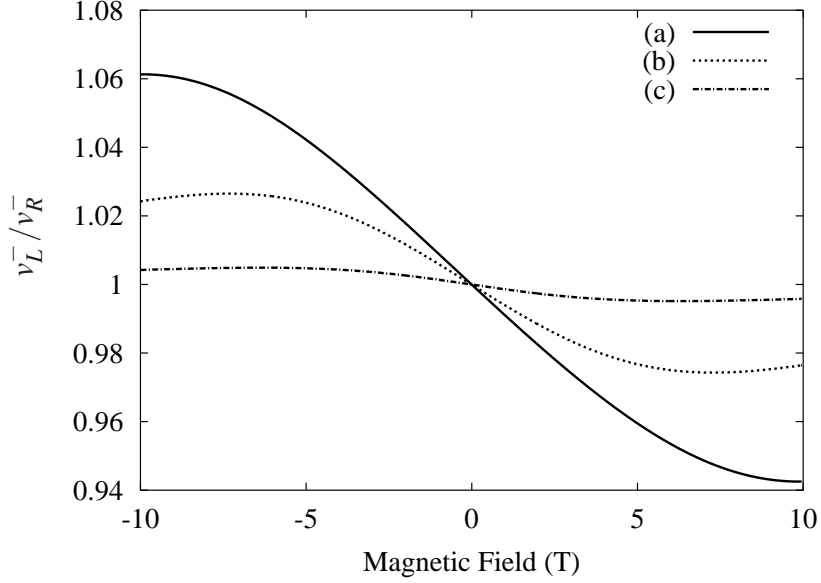
Figure 5.2: The influence of the external magnetic field and the curvature of the wire on the chiral asymmetry of the density of states. The relation between the Fermi velocities for left- and right-moving electrons v_L/v_R is chosen as a degree of the asymmetry. The parameters are taken relevant for InAs: $\alpha = 2 \cdot 10^{-11}$ eVm, $m^* = 0.033 m_e$, $g^* = -12$, $E_F = 30$meV. The radius of the curvature is (a) $R = 5 \cdot 10^{-6}$cm, (b) $R = 1 \cdot 10^{-5}$cm, (c) $R = 5 \cdot 10^{-5}$cm.

can easily be found. As a degree of their chiral asymmetry we use the relation between v_L^- and v_R^-. The dependences of v_L^-/v_R^- on the magnetic field for different radii of the loop are given in fig. 5.2. The Fermi level is taken to be equal 30meV. However, in contrast to the situation depicted in fig. 5.1, both spin-split subbands are occupied at this Fermi energy. In fig. 5.3, the Fermi energy is taken ten times smaller so, that it is possible to empty the upper band in fig. 5.1 by means of Zeeman splitting. Note, that the chiral asymmetry is even stronger in this case.

Let us turn to the electron-electron interactions. The Tomonaga-Luttinger model suggests the following Hamiltonian for the description of electron-electron interactions in the system with chiral asymmetry

$$H = H_{\text{kin}} + H_{\text{int}}, \tag{5.8}$$

where

$$H_{\text{kin}} = \int \frac{dx}{2\pi} \left[\psi_L^\dagger(x) \left(i\hbar v_L^- \frac{\partial}{\partial x} \right) \psi_L(x) + \psi_R^\dagger(x) \left(-i\hbar v_R^- \frac{\partial}{\partial x} \right) \psi_R(x) \right], \tag{5.9}$$

$$H_{\text{int}} = \int \frac{dx}{2\pi} \left(g_2 \psi_L^\dagger(x)\psi_L(x)\psi_R^\dagger(x)\psi_R(x) + \right.$$

$$\left. + \frac{1}{2} g_4 \left\{ \left[\psi_L^\dagger(x)\psi_L(x) \right]^2 + \left[\psi_R^\dagger(x)\psi_R(x) \right]^2 \right\} \right). \tag{5.10}$$

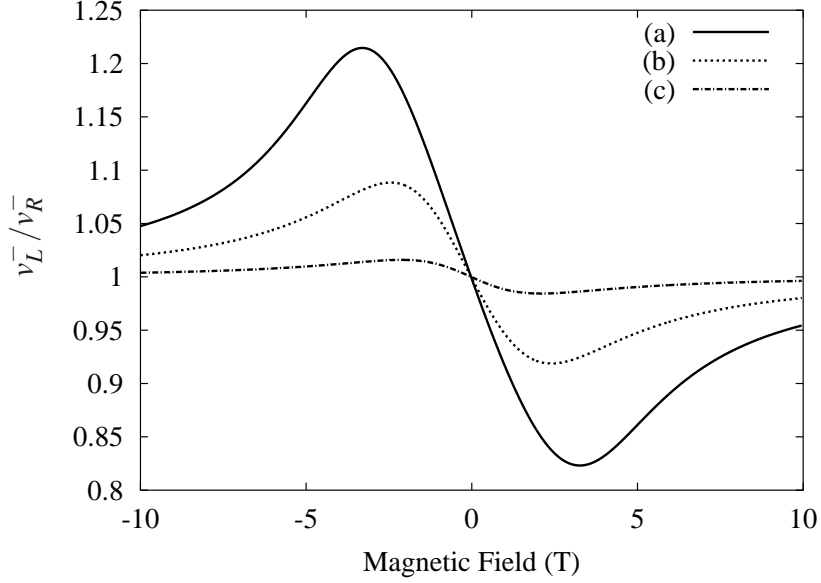Figure 5.3: The same as for fig. 5.2, but the Fermi energy is taken more relevant for the situation depicted in fig. 5.1, i. e. $E_F = 3$meV. The radius of the curvature is (a) $R = 5 \cdot 10^{-6}$cm, (b) $R = 1 \cdot 10^{-5}$cm, (c) $R = 5 \cdot 10^{-5}$cm. The other parameters are the same as for fig. 5.2.

Here $\psi_L(x)$, $\psi_R(x)$ are the fermion fields for left- and right-moving electrons respectively, $g_{2,4}$ are interaction constants, and x is the coordinate along the wire. The Fermi velocities v_L^- and v_R^- are taken as their absolute values. They are assumed to be described by (5.7). The electron energy is counted from its Fermi value.

Note, that in contrast to the introductory Chapter 2, the parameters g_2 and g_4 have dimension of energy/length here. Indeed, if we omit the exchange term in [84], then the interaction constants are

$$g_4 = V_1(0), \tag{5.11}$$

for electrons with the same chirality

$$g_2 = V_1(0) - \frac{V_1(-q_L^- + q_R^-)}{2}, \tag{5.12}$$

for electrons with opposite chiralities. Here $V_1(q)$ is the Fourier transform of a given interelectron potential. (Coulomb, in the simplest case.)

Using the bosonization identity [95], the Hamiltonian (5.8) can be written in a bosonized form often encountered in the literature (see Chapter 2), namely

$$H = \frac{1}{2} \int \frac{dx}{2\pi} \left(\begin{array}{cc} \frac{\partial \phi_L(x)}{\partial x}, & \frac{\partial \phi_R(x)}{\partial x} \end{array} \right) \left(\begin{array}{cc} \hbar v_L^- + g_4 & g_2 \\ g_2 & \hbar v_R^- + g_4 \end{array} \right) \left(\begin{array}{c} \frac{\partial \phi_L(x)}{\partial x} \\ \frac{\partial \phi_R(x)}{\partial x} \end{array} \right). \tag{5.13}$$

Here $\phi_L(x)$ and $\phi_R(x)$ are bosonic fields, and the terms with quadratic number operators $N_{L,R}^2$ are omitted.

The standard way to diagonalize the Hamiltonian of any interacting system in the framework of the Tomonaga-Luttinger model is to introduce so-called "dual fields". The standard couple of "dual fields" is defined as the difference and sum between boson fields with opposite chiralities (see Chapter 2). However, the application of this standard approach is not so trivial here because of the different Fermi velocities for right- and left-moving electrons. The "dual fields" are not really dual here, since the chiral symmetry is completely broken.

In order to solve the problem, we introduce additional fictitious bosonic fields $\phi'_R(x)$ and $\phi'_L(x)$ in a way which does not change the dynamics of the system. Then the Hamiltonian (5.13) can be rewritten as

$$H \rightarrow H + H' =$$

$$\frac{1}{2} \int \frac{dx}{2\pi} \begin{pmatrix} \partial\phi_R(x)/\partial x \\ \partial\phi_L(x)/\partial x \\ \partial\phi'_R(x)/\partial x \\ \partial\phi'_L(x)/\partial x \end{pmatrix}^T \begin{pmatrix} \hbar v_R^- + g_4 & g_2 & 0 & 0 \\ g_2 & \hbar v_L^- + g_4 & 0 & 0 \\ 0 & 0 & \hbar v_L^- + g_4 & g_2 \\ 0 & 0 & g_2 & \hbar v_R^- + g_4 \end{pmatrix} \begin{pmatrix} \partial\phi_R(x)/\partial x \\ \partial\phi_L(x)/\partial x \\ \partial\phi'_R(x)/\partial x \\ \partial\phi'_L(x)/\partial x \end{pmatrix},$$

(5.14)

Note, that these additional bosonic fields $\phi'_L(x)$ and $\phi'_R(x)$ extend the basis 2×2 to 4×4, whereas the given symmetry between them allows us to introduce *two couples* of "dual fields" correctly.

In order to simplify the subsequent calculations, we rewrite this Hamiltonian ones more in the dimensionless form

$$H =$$

$$\frac{\hbar v_R^-}{2} \int \frac{dx}{2\pi} \begin{pmatrix} \partial\phi_R(x)/\partial x \\ \partial\phi_L(x)/\partial x \\ \partial\phi'_R(x)/\partial x \\ \partial\phi'_L(x)/\partial x \end{pmatrix}^T \begin{pmatrix} 1 + g_4 & g_2 & 0 & 0 \\ g_2 & g + g_4 & 0 & 0 \\ 0 & 0 & g + g_4 & g_2 \\ 0 & 0 & g_2 & 1 + g_4 \end{pmatrix} \begin{pmatrix} \partial\phi_R(x)/\partial x \\ \partial\phi_L(x)/\partial x \\ \partial\phi'_R(x)/\partial x \\ \partial\phi'_L(x)/\partial x \end{pmatrix}.$$

(5.15)

Here we redefined the interaction constants $g_{2,4} \rightarrow g_{2,4}/\hbar v_R^-$ to be dimensionless. The constant $g = v_L^-/v_R^-$ is assumed to be a measure of the dispersion law asymmetry.

Using the fact of chiral symmetry between the "original" and "fictitious" branches we define the couples of "dual fields" (Φ_1, Θ_1) and (Φ_2, Θ_2) in the following way

$$\frac{\partial\phi_R(x)}{\partial x} = \frac{1}{\sqrt{2}} \left(\frac{\partial\Phi_1}{\partial x} - \frac{\partial\Theta_1}{\partial x} \right), \quad \frac{\partial\phi'_L(x)}{\partial x} = \frac{1}{\sqrt{2}} \left(\frac{\partial\Phi_1}{\partial x} + \frac{\partial\Theta_1}{\partial x} \right);$$

$$\frac{\partial\phi'_R(x)}{\partial x} = \frac{1}{\sqrt{2}} \left(\frac{\partial\Phi_2}{\partial x} - \frac{\partial\Theta_2}{\partial x} \right), \quad \frac{\partial\phi_L(x)}{\partial x} = \frac{1}{\sqrt{2}} \left(\frac{\partial\Phi_2}{\partial x} + \frac{\partial\Theta_2}{\partial x} \right).$$

(5.16)

Substituting (5.16) into the Hamiltonian (5.15) we have

$$H = \frac{\hbar v_R^-}{2} \int \frac{dx}{2\pi} \left[(\partial_x \Phi^T) M_\Phi (\partial_x \Phi) + (\partial_x \Theta^T) M_\Theta (\partial_x \Theta) \right],$$

(5.17)

where

$$M_\Phi = \begin{pmatrix} 1 + g_4 & g_2 \\ g_2 & g + g_4 \end{pmatrix},$$

(5.18)

$$M_\Theta = \begin{pmatrix} 1+g_4 & -g_2 \\ -g_2 & g+g_4 \end{pmatrix}, \tag{5.19}$$

and $\Phi = (\Phi_1, \Phi_2)^T$, $\Theta = (\Theta_1, \Theta_2)^T$.

First of all, we diagonalize the matrix M_Φ in the standard way. Its eigenvalues $\lambda_{1,2}$ can be found from

$$(1+g_4-\lambda)(g+g_4-\lambda) - g_2^2 = 0, \tag{5.20}$$

and they are

$$\lambda_{1,2} = \frac{1+g}{2} + g_4 \mp \frac{1}{2}\sqrt{(1-g)^2 + 4g_2^2}. \tag{5.21}$$

The corresponding transformation matrix reads

$$P_\Phi = \begin{pmatrix} -\sqrt{\frac{g_2}{\sqrt{D}}} & -\sqrt{\frac{g_2}{\sqrt{D}}} \\ \frac{1-g+\sqrt{D}}{2\sqrt{g_2\sqrt{D}}} & \frac{1-g-\sqrt{D}}{2\sqrt{g_2\sqrt{D}}} \end{pmatrix}, \tag{5.22}$$

and the inverse one is

$$P_\Phi^{-1} = \begin{pmatrix} \frac{1-g-\sqrt{D}}{2\sqrt{g_2\sqrt{D}}} & \sqrt{\frac{g_2}{\sqrt{D}}} \\ \frac{g-1-\sqrt{D}}{2\sqrt{g_2\sqrt{D}}} & -\sqrt{\frac{g_2}{\sqrt{D}}} \end{pmatrix}, \tag{5.23}$$

where $D = (1-g)^2 + 4g_2^2$.

In the next step we first rescale the basis so, that

$$\widetilde{M}_\Phi = \Lambda_\Phi^{-1} P_\Phi^{-1} M_\Phi P_\Phi \Lambda_\Phi^{-1} \tag{5.24}$$

is the unit matrix, and, secondly, preserve the duality of the fields Φ_i and Θ_i so, that

$$\widetilde{M}_\Theta = \Lambda_\Phi P_\Phi^{-1} M_\Theta P_\Phi \Lambda_\Phi. \tag{5.25}$$

The matrices Λ_Φ and Λ_Φ^{-1} are given by

$$\Lambda_\Phi = \begin{pmatrix} \sqrt{\lambda_1} & 0 \\ 0 & \sqrt{\lambda_2} \end{pmatrix}, \qquad \Lambda_\Phi^{-1} = \begin{pmatrix} 1/\sqrt{\lambda_1} & 0 \\ 0 & 1/\sqrt{\lambda_2} \end{pmatrix}. \tag{5.26}$$

The elements of the matrix

$$\widetilde{M}_\Theta = \begin{pmatrix} a & b \\ c & d \end{pmatrix} \tag{5.27}$$

can be found after some simple algebra

$$a = \lambda_1 \left[\frac{1+g}{2} + g_4 - \frac{(1-g)^2 - 4g_2^2}{2\sqrt{D}} \right],$$

$$b = \sqrt{\lambda_1 \lambda_2} \left[(1-g) - \frac{(1-g)^2}{\sqrt{D}} \right],$$

$$c = \sqrt{\lambda_1 \lambda_2} \left[(1-g) + \frac{(1-g)^2}{\sqrt{D}} \right],$$

$$d = \lambda_2 \left[\frac{1+g}{2} + g_4 + \frac{(1-g)^2 - 4g_2^2}{2\sqrt{D}} \right].$$

Note, that a further unitary transformations can not change the matrix $\widetilde{M}_\Phi$ (which is equal to the unit one I_2). For this reason we can diagonalize $\widetilde{M}_\Theta$ and do not care of $\widetilde{M}_\Phi$. The eigen values of $\widetilde{M}_\Theta$ can be easily found from the obvious equation

$$(a - \varepsilon)(d - \varepsilon) - bc = 0, \tag{5.28}$$

and they are

$$\varepsilon_{1,2} = \frac{a + d \pm \sqrt{(a-d)^2 + 4bc}}{2}. \tag{5.29}$$

The corresponding transformation matrix reads

$$P_\Theta = \begin{pmatrix} \sqrt{\frac{b}{\sqrt{D_2}}} & -\sqrt{\frac{b}{\sqrt{D_2}}} \\ \frac{d-a+\sqrt{D_2}}{2\sqrt{b\sqrt{D_2}}} & \frac{a-d+\sqrt{D_2}}{2\sqrt{b\sqrt{D_2}}} \end{pmatrix}, \tag{5.30}$$

and the inverse P_Θ^{-1} is

$$P_\Theta^{-1} = \begin{pmatrix} \frac{a-d+\sqrt{D_2}}{2\sqrt{b\sqrt{D_2}}} & \sqrt{\frac{b}{\sqrt{D_2}}} \\ \frac{a-d-\sqrt{D_2}}{2\sqrt{b\sqrt{D_2}}} & \sqrt{\frac{b}{\sqrt{D_2}}} \end{pmatrix}, \tag{5.31}$$

where $D_2 = (a-d)^2 + 4bc$.

Finally, we have diagonalized both $\widetilde{M}_\Phi$ and $\widetilde{M}_\Theta$ matrices. But the form of the Hamiltonian is still non-canonical. To arrive at the canonical form, we have to rescale again both $\widetilde{M}_\Phi$ and $\widetilde{M}_\Theta$ by using the matrices

$$\Lambda_\varepsilon = \begin{pmatrix} (\varepsilon_1)^{1/4} & 0 \\ 0 & (\varepsilon_2)^{1/4} \end{pmatrix}, \qquad \Lambda_\varepsilon^{-1} = \begin{pmatrix} (\varepsilon_1)^{-1/4} & 0 \\ 0 & (\varepsilon_2)^{-1/4} \end{pmatrix}. \tag{5.32}$$

The desired form of M_Φ and M_Θ can be obtained by the following transformations (which preserve, as usual, the duality of the fields Φ_i and Θ_i)

$$M_\Phi^{\text{canonical}} = \Lambda_\varepsilon P_\Theta^{-1} \Lambda_\Phi^{-1} P_\Phi^{-1} M_\Phi P_\Phi \Lambda_\Phi^{-1} P_\Theta \Lambda_\varepsilon, \tag{5.33}$$

$$M_\Theta^{\text{canonical}} = \Lambda_\varepsilon^{-1} P_\Theta^{-1} \Lambda_\Phi P_\Phi^{-1} M_\Theta P_\Phi \Lambda_\Phi P_\Theta \Lambda_\varepsilon^{-1}, \tag{5.34}$$

and

$$M_\Phi^{\text{canonical}} = M_\Theta^{\text{canonical}} = \begin{pmatrix} \sqrt{\varepsilon_1} & 0 \\ 0 & \sqrt{\varepsilon_2} \end{pmatrix}. \tag{5.35}$$

For the following notation it is convenient to introduce the matrices

$$S_\Phi = P_\Phi \Lambda_\Phi^{-1} P_\Theta \Lambda_\varepsilon, \qquad S_\Phi^{-1} = \Lambda_\varepsilon P_\Theta^{-1} \Lambda_\Phi^{-1} P_\Phi^{-1}, \tag{5.36}$$

$$S_\Theta = P_\Phi \Lambda_\Phi P_\Theta \Lambda_\varepsilon^{-1}, \qquad S_\Theta^{-1} = \Lambda_\varepsilon^{-1} P_\Theta^{-1} \Lambda_\Phi P_\Phi^{-1}. \tag{5.37}$$

Their elements are given in Appendix B.

The Hamiltonian (5.17) takes now the canonical form, namely

$$H = \frac{\hbar u_1}{2} \int \frac{dx}{2\pi} \left(\partial_x \eta_1^2 + \partial_x \xi_1^2 \right) + \frac{\hbar u_2}{2} \int \frac{dx}{2\pi} \left(\partial_x \eta_2^2 + \partial_x \xi_2^2 \right), \tag{5.38}$$

where the new dual fields $\eta = (\eta_1, \eta_2)$, $\xi = (\xi_1, \xi_2)$ are related to the original ones by transformations $\Phi = \eta S_\Phi^{-1}$, $\Phi^T = S_\Phi \eta^T$, $\Theta = \xi S_\Theta^{-1}$, $\Theta^T = S_\Theta \xi^T$, and new renormalized velocities can be found in two ways. The first is rather direct $u_1 = v_R^- \sqrt{\varepsilon_1}$ and $u_2 = v_R^- \sqrt{\varepsilon_2}$, whereas the second one uses the elements of matrices S_Φ and S_Θ as following

$$\frac{u_1}{v_R^-} = (S_{\Phi,\Theta}^{11})^{-1} M_{\Phi,\Theta}^{11} (S_{\Phi,\Theta}^{11}) + (S_{\Phi,\Theta}^{11})^{-1} M_{\Phi,\Theta}^{12} (S_{\Phi,\Theta}^{21}) +$$

$$(S_{\Phi,\Theta}^{12})^{-1} M_{\Phi,\Theta}^{21} (S_{\Phi,\Theta}^{11}) + (S_{\Phi,\Theta}^{12})^{-1} M_{\Phi,\Theta}^{22} (S_{\Phi,\Theta}^{21}), \tag{5.39}$$

$$\frac{u_2}{v_R^-} = (S_{\Phi,\Theta}^{21})^{-1} M_{\Phi,\Theta}^{11} (S_{\Phi,\Theta}^{21}) + (S_{\Phi,\Theta}^{21})^{-1} M_{\Phi,\Theta}^{12} (S_{\Phi,\Theta}^{22}) +$$

$$(S_{\Phi,\Theta}^{22})^{-1} M_{\Phi,\Theta}^{21} (S_{\Phi,\Theta}^{12}) + (S_{\Phi,\Theta}^{22})^{-1} M_{\Phi,\Theta}^{22} (S_{\Phi,\Theta}^{22}). \tag{5.40}$$

The velocities can also be written explicitely in the form

$$u_{1,2} = v_R^- \left\{ \frac{1+g^2}{2} + g_4 (1 + g + g_4) - g_2^2 \right.$$

$$\left. \pm (1-g) \sqrt{ \frac{[(1+g)/2 + g_4]^2 (1-g)^2}{(1-g)^2 + 4g_2^2} + \left[g + g_4(1+g+g_4) - g_2^2 \right] \left[1 - \frac{(1-g)^2}{(1-g)^2 + 4g_2^2} \right] } \right\}^{\frac{1}{2}}. \tag{5.41}$$

At the end of this section, we consider two limiting cases. The first one is the case of weak electron-electron interactions. It is interesting to note here, that in the case of negligible backscattering ($g_2 = 0$) the plasmon velocities have extremely simple dependences on the interaction constant, namely

$$u_1 = v_R^- (1 + g_4), \quad u_2 = v_R^- (g + g_4). \tag{5.42}$$

As soon as both g_2 and g_4 are equal to zero, the non-interacting result is recovered, i. e. $u_1 = v_R^-$ and $u_2 = v_L^-$.

In the opposite limit, the electron-electron interactions are assumed to be strong enough so, that $g_{2,4} \gg 1$. Then, it is possible to make the following estimations

$$\lambda_{1,2} \approx g_4 \mp g_2, \tag{5.43}$$

$$P_\Phi = \begin{pmatrix} -\frac{1}{\sqrt{2}} & -\frac{1}{\sqrt{2}} \\ \frac{1}{\sqrt{2}} & -\frac{1}{\sqrt{2}} \end{pmatrix}, \tag{5.44}$$

$$P_\Phi^{-1} = \begin{pmatrix} -\frac{1}{\sqrt{2}} & \frac{1}{\sqrt{2}} \\ -\frac{1}{\sqrt{2}} & -\frac{1}{\sqrt{2}} \end{pmatrix}. \tag{5.45}$$

Then

$$a = g_4^2 - g_2^2 = d, \tag{5.46}$$

$$b = (1-g)\sqrt{g_4^2 - g_2^2} = c, \tag{5.47}$$

and

$$S_\Phi^{11} = -\frac{(\varepsilon_1)^{\frac{1}{4}}}{2}\left(\frac{1}{\sqrt{\lambda_1}} + \frac{1}{\sqrt{\lambda_2}}\right) = (S_\Phi^{11})^{-1}, \quad S_\Phi^{12} = \frac{(\varepsilon_2)^{\frac{1}{4}}}{2}\left(\frac{1}{\sqrt{\lambda_1}} - \frac{1}{\sqrt{\lambda_2}}\right) = (S_\Phi^{21})^{-1},$$

$$S_\Phi^{21} = \frac{(\varepsilon_1)^{\frac{1}{4}}}{2}\left(\frac{1}{\sqrt{\lambda_1}} - \frac{1}{\sqrt{\lambda_2}}\right) = (S_\Phi^{12})^{-1}, \quad S_\Phi^{22} = -\frac{(\varepsilon_2)^{\frac{1}{4}}}{2}\left(\frac{1}{\sqrt{\lambda_1}} + \frac{1}{\sqrt{\lambda_2}}\right) = (S_\Phi^{22})^{-1},$$

$$S_\Theta^{11} = -\frac{1}{(2\varepsilon_1)^{\frac{1}{4}}}\left(\sqrt{\lambda_1} + \sqrt{\lambda_2}\right) = (S_\Theta^{11})^{-1}, \quad S_\Theta^{12} = \frac{1}{(2\varepsilon_2)^{\frac{1}{4}}}\left(\sqrt{\lambda_1} - \sqrt{\lambda_2}\right) = (S_\Theta^{21})^{-1},$$

$$S_\Theta^{21} = \frac{1}{(2\varepsilon_1)^{\frac{1}{4}}}\left(\sqrt{\lambda_1} - \sqrt{\lambda_2}\right) = (S_\Theta^{12})^{-1}, \quad S_\Theta^{22} = -\frac{1}{(2\varepsilon_2)^{\frac{1}{4}}}\left(\sqrt{\lambda_1} + \sqrt{\lambda_2}\right) = (S_\Theta^{22})^{-1},$$

where $\varepsilon_{1,2} = g_4^2 - g_2^2 \pm (1-g)\sqrt{g_4^2 - g_2^2}$.

Recall, that the plasmon velocities are determined by $\varepsilon_{1,2}$ as $u_{1,2} = v_R^-\sqrt{\varepsilon_{1,2}}$. Therefore, if the electron-electron interactions are so strong, that

$$\varepsilon_{1,2} \simeq g_4^2 - g_2^2, \tag{5.48}$$

then both plasmon velocities are just equal. Moreover, the elements of matrices S_Φ and S_Θ satisfy the following relations

$$S_{\Theta,\Phi}^{ii} = S_{\Theta,\Phi}^{jj} \quad S_{\Theta,\Phi}^{ij} = S_{\Theta,\Phi}^{ji}. \tag{5.49}$$

5.3 Electron-electron interactions and chiral asymmetry of the density of states

In this section, we study the influence of the electron-electron interactions on the chiral density of states. The latter can be derived via retarded Green's functions as it has been done for the symmetric case in the introductory Chapter 2. The basic formulae are (2.68), (2.69) and (2.70). Thus, we must find the following two-point bosonic correlation functions

$$\langle \phi_R(x,\tau)\phi_R(0,0)\rangle = \langle \phi_L'(x,\tau)\phi_L'(0,0)\rangle =$$
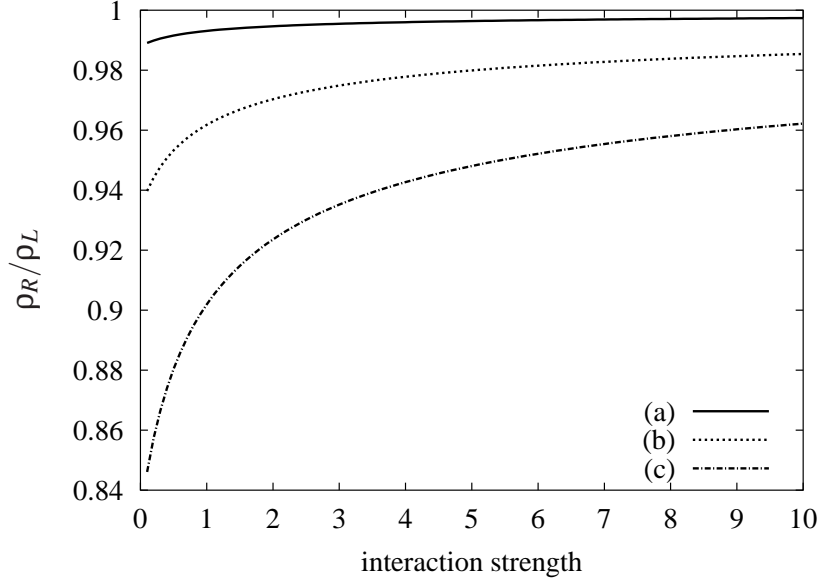
Figure 5.4: The alignment of the density of states for left- and right- moving electrons in the curved wire subject to electron-electron interactions. The constants g_2 and g_4 are assumed to be equal. In order to create the initial asymmetry, the external magnetic field of 4T is applied. The Fermi energy is taken to be equal to 3meV. The other parameters are taken relevant for InAs: $\alpha = 2 \cdot 10^{-11}$ eVm, $m^* = 0.033 m_e$, $g^* = -12$. Different curves correspond to different radius of the curvature: (a) $R = 5 \cdot 10^{-5}$cm, (b) $R = 10^{-5}$cm, (c) $R = 5 \cdot 10^{-6}$cm.

$$\frac{1}{2} \left[\langle \eta_1(x,\tau)\eta_1(0,0) \rangle \left(S_\Phi^{11} \right)^{-1} S_\Phi^{11} + \langle \eta_2(x,\tau)\eta_2(0,0) \rangle \left(S_\Phi^{21} \right)^{-1} S_\Phi^{12} \right.$$

$$\left. + \langle \xi_1(x,\tau)\xi_1(0,0) \rangle \left(S_\Theta^{11} \right)^{-1} S_\Theta^{11} + \langle \xi_2(x,\tau)\xi_2(0,0) \rangle \left(S_\Theta^{21} \right)^{-1} S_\Theta^{12} \right], \tag{5.50}$$

$$\langle \phi_R'(x,\tau)\phi_R'(0,0) \rangle = \langle \phi_L(x,\tau)\phi_L(0,0) \rangle =$$

$$\frac{1}{2} \left[\langle \eta_1(x,\tau)\eta_1(0,0) \rangle \left(S_\Phi^{12} \right)^{-1} S_\Phi^{21} + \langle \eta_2(x,\tau)\eta_2(0,0) \rangle \left(S_\Phi^{22} \right)^{-1} S_\Phi^{22} \right.$$

$$\left. + \langle \xi_1(x,\tau)\xi_1(0,0) \rangle \left(S_\Theta^{12} \right)^{-1} S_\Theta^{21} + \langle \xi_2(x,\tau)\xi_2(0,0) \rangle \left(S_\Theta^{22} \right)^{-1} S_\Theta^{22} \right]. \tag{5.51}$$

The correlators of the fictitious bosonic fields $\langle \phi_L'(x,\tau)\phi_L'(0,0) \rangle$ and $\langle \phi_R'(x,\tau)\phi_R'(0,0) \rangle$ are given only for the sake of completeness, we do not need them for the correlation functions of the "real" fermionic fields.

The fields η_i and ξ_i are canonical, i. e. they describe free bosons. For this reason, the two-point correlation functions of them are given by formulae similar to (2.71), namely

$$\langle \eta_i(x,\tau)\eta_i(0,0) \rangle = \langle \xi_i(x,\tau)\xi_i(0,0) \rangle = -\ln \left[\frac{2\pi}{L} \left(\text{sign}_\tau u_i \tau + i\,\text{sign}_\tau x + a \right) \right], \tag{5.52}$$

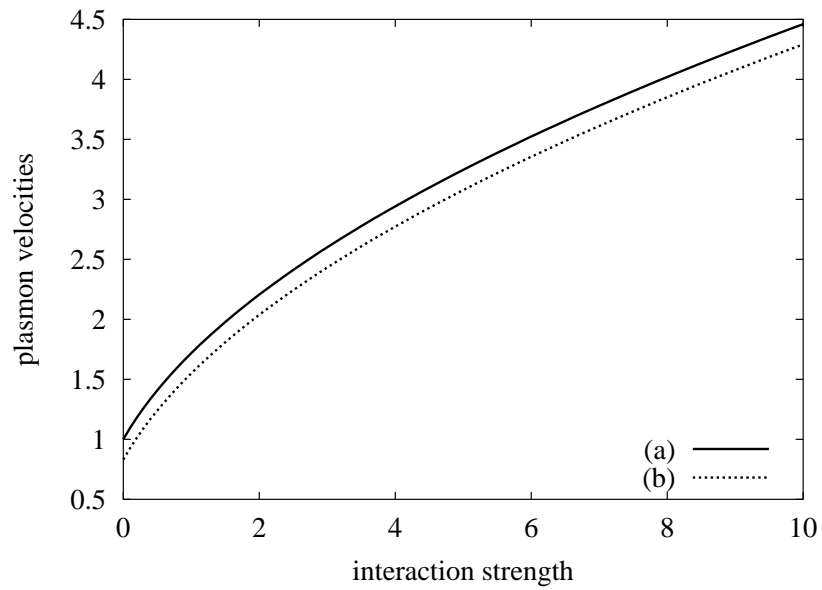where u_i are given by (5.39) and (5.40).

Figure 5.5: Plasmon velocities in units of v_R^- versus interaction constant. Curve (a) corresponds to the velocity u_1, and (b) — u_2. The parameters of the system are exactly the same as in fig. 5.4.
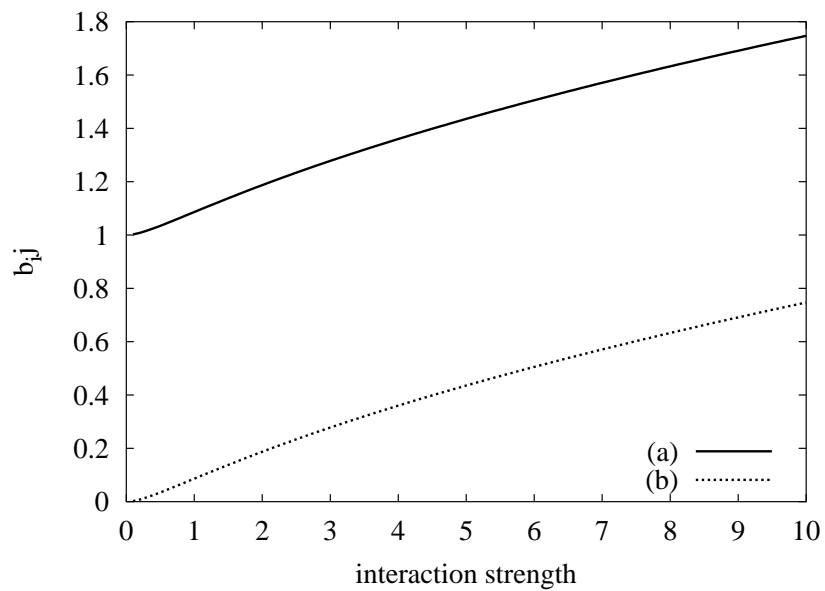

Figure 5.6: Coefficients b_{ij} versus interaction constant. Curve (a) corresponds to b_{11}, and (b) — b_{12}. The parameters of the system are exactly the same as in fig. 5.4.

In the following let us use the notation

$$b_{11} = \frac{1}{2}\left[(S_\Phi^{11})^{-1}S_\Phi^{11} + (S_\Theta^{11})^{-1}S_\Theta^{11}\right], \qquad b_{12} = \frac{1}{2}\left[(S_\Phi^{21})^{-1}S_\Phi^{12} + (S_\Theta^{21})^{-1}S_\Theta^{12}\right], \qquad (5.53)$$

$$b_{21} = \frac{1}{2}\left[(S_\Phi^{12})^{-1}S_\Phi^{21} + (S_\Theta^{12})^{-1}S_\Theta^{21}\right], \qquad b_{22} = \frac{1}{2}\left[(S_\Phi^{22})^{-1}S_\Phi^{22} + (S_\Theta^{22})^{-1}S_\Theta^{22}\right]. \qquad (5.54)$$

Substituting the bosonic correlators (5.50) and (5.51) into the fundamental formula (2.70), we obtain the desired correlation functions for fermionic fields

$$\left\langle \mathcal{T}\psi_R(x,\tau)\psi_R^\dagger(0,0)\right\rangle = \frac{\mathrm{sign}_\tau\, a^{b_{11}+b_{12}-1}}{(\mathrm{sign}_\tau u_1\tau + i\mathrm{sign}_\tau x + a)^{b_{11}}(\mathrm{sign}_\tau u_2\tau + i\mathrm{sign}_\tau x + a)^{b_{12}}}, \qquad (5.55)$$

$$\left\langle \mathcal{T}\psi_L(x,\tau)\psi_L^\dagger(0,0)\right\rangle = \frac{\mathrm{sign}_\tau\, a^{b_{21}+b_{22}-1}}{(\mathrm{sign}_\tau u_1\tau + i\mathrm{sign}_\tau x + a)^{b_{21}}(\mathrm{sign}_\tau u_2\tau + i\mathrm{sign}_\tau x + a)^{b_{22}}}. \qquad (5.56)$$

Then, the retarded real-time Green functions for left- and right-moving particles read

$$G_R^{\mathrm{ret}}(x=0,t) = \frac{a^{b_{11}+b_{12}-1}}{iu_1^{b_{11}}u_2^{b_{12}}}\left\{[i(t-i0)]^{-b_{11}-b_{12}} - [i(t+i0)]^{-b_{11}-b_{12}}\right\}\Theta(t), \qquad (5.57)$$

$$G_L^{\mathrm{ret}}(x=0,t) = \frac{a^{b_{21}+b_{22}-1}}{iu_1^{b_{21}}u_2^{b_{22}}}\left\{[i(t-i0)]^{-b_{21}-b_{22}} - [i(t+i0)]^{-b_{21}-b_{22}}\right\}\Theta(t). \qquad (5.58)$$

Now, the density of states can be derived straightforwardly by substituting the relations (5.57) and (5.58) into formula (2.68). The integral over t can be taken using the definition of the Γ-function, while the path of integration is depicted in fig. 2.16. After some algebra we arrive at the final formulae for the density of states

$$\rho_R^{\mathrm{DoS}}(\omega) = \frac{1}{2\pi\hbar}\frac{(a\omega)^{b_{11}+b_{12}-1}}{u_1^{b_{11}}u_2^{b_{12}}}\sin\left[\pi(b_{11}+b_{12})\right]\Gamma(1-b_{11}-b_{12}), \qquad (5.59)$$

$$\rho_L^{\mathrm{DoS}}(\omega) = \frac{1}{2\pi\hbar}\frac{(a\omega)^{b_{21}+b_{22}-1}}{u_1^{b_{21}}u_2^{b_{22}}}\sin\left[\pi(b_{21}+b_{22})\right]\Gamma(1-b_{21}-b_{22}). \qquad (5.60)$$

The relation $\rho_R^{\mathrm{DoS}}/\rho_L^{\mathrm{DoS}}$ is shown in fig. 5.4 as a function of the electron-electron interaction strength parameterized by $g_4 = g_2$. The corresponding behavior of the plasmon velocities and coefficients b_{ij} is depicted in figs. 5.5 and 5.6 respectively. One can easily see, that electron-electron interactions lead to an alignment of the chiral densities of states. This is the main result of this section. Note, that the effect is not very sensitive to the relation between g_4 and g_2. That is why we have adopted the simplest one $g_2 = g_4$.

As in the previous section, we study the expressions (5.59) and (5.60) in two limits: (i) weak and (ii) strong electron-electron interactions. The first case is rather simple. Indeed, if $g_2 = 0$

then $b_{12} = b_{21} = 0$, $b_{11} = b_{22} = 1$, and the plasmon velocities are given by (5.42). The density of states reads

$$\rho_R^{\text{DoS}} = \frac{1}{2\pi\hbar}\frac{1}{u_1}, \quad \rho_L^{\text{DoS}} = \frac{1}{2\pi\hbar}\frac{1}{u_2}. \tag{5.61}$$

Let us make a comment on the relations (5.61). Although g_4 is still not zero, the standard Fermi liquid property $\rho^{\text{DoS}} \neq 0$ at $\omega = 0$ is already recovered. However, the alignment of the density of states by means of interactions does not vanish yet, since $\rho_R^{\text{DoS}}/\rho_L^{\text{DoS}} = (g + g_4)/(1 + g_4) \to 1$ as long as $g_4 \to \infty$. Of course, if g_4 is equal to zero as well, then $u_1 = v_R^-$, $u_2 = v_L^-$ and

$$\rho_R^{\text{DoS}}/\rho_L^{\text{DoS}} = v_L/v_R. \tag{5.62}$$

Let us consider the opposite case of strong electron-electron interactions. Note, that at $g_{2,4} \gg 1$ the following estimates for b_{ij} are valid

$$b_{11} = \frac{1}{2}\left(1 + \frac{g_4}{\sqrt{g_4^2 - g_2^2}}\right) = b_{22}, \tag{5.63}$$

$$b_{12} = \frac{1}{2}\left(\frac{g_4}{\sqrt{g_4^2 - g_2^2}} - 1\right) = b_{21}, \tag{5.64}$$

and, as consequence,

$$b_{11} + b_{12} = b_{22} + b_{21} = \frac{g_4}{\sqrt{g_4^2 - g_2^2}}, \tag{5.65}$$

$$b_{11} - b_{21} = b_{22} - b_{12} = 1. \tag{5.66}$$

Therefore, the relation between the densities of states with opposite chirality reads

$$\frac{\rho_R^{\text{DoS}}}{\rho_L^{\text{DoS}}} = \frac{u_2^{b_{22}-b_{12}}}{u_1^{b_{11}-b_{21}}} \equiv \frac{u_2}{u_1}. \tag{5.67}$$

As we have found in the previous section, the relation u_2/u_1 goes to 1 as long as the electron-electron interactions increase [see the estimation (5.48)]. Thus, we have proven analytically, that strong electron-electron interactions remedy the chiral symmetry of a Tomonaga-Luttinger liquid.

It is interesting to note, that the plasmon density of states is always equal to zero at the Fermi level for both left- and right- moving electrons. [This case corresponds to $\omega = 0$ in (5.59) and (5.60).] Therefore, the plasmon density of states at the Fermi level is always chirally symmetric ($\rho_R^{\text{DoS}} = \rho_L^{\text{DoS}} = 0$). In the vicinity of the Fermi level the dependence of the plasmon density of states on the energy $\hbar\omega$ is determined by two factors. First, the electron-electron interactions increase the plasmon excitation energy, and, therefore, the plasmon density of states is negligible (and chirally symmetric!) at larger energy interval in the vicinity of the Fermi level. Second, the interaction between left- and right-moving electrons leads to the energy exchange between them and, therefore, to the alignment of their density of states. In other words, the plasmons with opposite chiralities start to talk with each other in a certain sense, and, thus, the abovementioned alignment takes place.

5.4 Chiral asymmetry and Landauer–Büttiker formalism

There is a large variety of transport theories in solid states physics developed for the description of the electron motion in different regimes: general Keldysh formalism, Kubo formula for linear responce (small bias voltage), Landauer-Büttiker formalism for coherent transport with elastic scattering, quasiclassical Boltzman equation, and Drude theory for the diffusive regime. The chiral asymmetry of the density of states could bring something new into the description of electron transport. In this section, we study the influence of the abovementioned chiral asymmetry on the Landauer-Büttiker formula [37, 38, 39, 96].

The latter has actually two modifications. In detail, the dc conductance of a 1D system at zero temperature equals either $G = 2G_0 T$ or $G = 2G_0 T/(1-T)$, depending on whether the system is connected to perfect 1D conductors (where the phase randomizing is absent) or to classical wires (non-coherent baths) respectively. (Here $G_0 = e^2/2\pi\hbar$ is the conductance quantum, T is the transmission probability, and the factor 2 occurs because of the spin degeneracy.) Both formulae do not contain the density of states, therefore, they are not influenced by its chiral asymmetry. In the case of non-zero temperature the situation changes drastically.

The conductance of a system with perfect 1D leads reads

$$G = 2G_0 \int dE \frac{-df}{dE} T(E),$$
(5.68)

whereas

$$G = 2G_0 \int dE \frac{-df}{dE} T(E) \frac{\int dE \frac{\partial n}{\partial E}\left(-\frac{df}{dE}\right)}{\int dE \frac{\partial n}{\partial E} R(E)\left(-\frac{df}{dE}\right)},$$
(5.69)

as soon as reservoirs are connected [39]. Here, $R(E) = 1 - T(E)$ is the reflection probability, $\partial n/\partial E$ is the density of states in the 1D leads, and $f(E)$ is the Fermi–Dirac distribution (in the equilibrium) given by

$$f(E) = \frac{1}{e^{\frac{E-E_F}{T}} + 1}.$$
(5.70)

Note, that formula (5.69) contains the density of states explicitly. That is why we find it interesting to generalize the conductance expression (5.69) to 1D systems which lack the chiral symmetry in the density of states.

The scheme proposed is depicted in fig. 5.7. The sample is connected to perfect and identical 1D leads where the density of states for left-moving electrons $\partial n_L/\partial E$ is not equal to $\partial n_R/\partial E$ for the right-moving ones. The leads are connected to electron reservoirs with chemical potentials μ_1 and μ_2 (see fig. 5.7). The sample is characterized by the transmission and reflection coefficients $T(E)$ and $R(E)$. Thus, we could apply the Landauer-Büttiker formalism for the description of electron transport through this system.

Let us find the conductance of the system given in fig. 5.7. We follow the Büttiker–Imry–Landauer–Pinhas derivation of the conductance formula [39]. The current emitted by the left
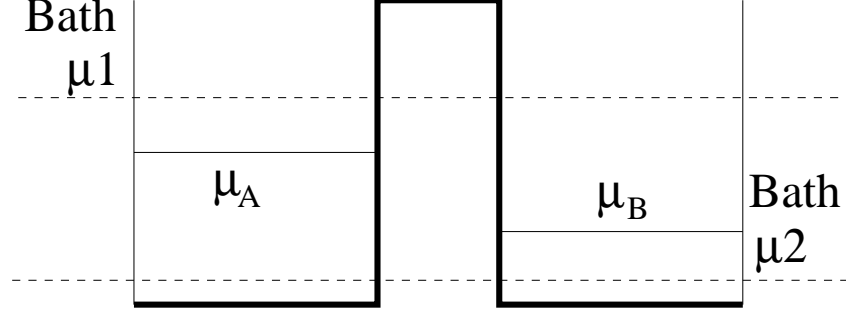
Figure 5.7: The system under consideration. The obstacle is connected to two incoherent reservoirs (baths) by ideal 1D conductors where the densities of states for right- and left-moving electrons are not equal. The reservoir 1 emits electrons up to the chemical potentials μ_1, and the reservoir 2 emits electrons up to the chemical potentials μ_2, whereas μ_A and μ_B are the chemical potentials in the perfectly conducting leads between reservoirs and the obstacle. The voltage drop across the sample is, therefore, $eV = \mu_A - \mu_B$. A flow of particles hits the barrier from the left. (Since μ_1 is assumed to be larger than μ_2.)

reservoir in the energy range between μ_1 and μ_2 is

$$I = \frac{e}{2\pi\hbar} \int dE \left(\frac{-df}{dE} \right) T(E) \Delta\mu, \tag{5.71}$$

where $\Delta\mu = \mu_1 - \mu_2$. Note, that in our system we have no spin degeneracy, therefore, the factor 2 does not enter (5.71). As the next step, we have to determine the relation between the difference in the chemical potentials μ_1, μ_2 and the voltage drop across the sample (i. e. the obstacle).

The carriers in the leads can be characterized by the chemical potentials μ_A and μ_B (see fig. 5.7). Their respective levels are determined by the condition of half-filling [39]. This condition assumes that the number of occupied states above μ_A (μ_B) is equal to the number of empty states below μ_A (μ_B). Now, let us find the relation between the chemical potentials in the leads (μ_A, μ_B) and in the reservoirs (μ_1, μ_2).

Below the energy μ_2 all states are fully occupied and we need to consider the energy range from μ_2 to μ_1 only. The total numbers of states in this range is

$$N_{\text{total}} = \int dE \left(\frac{-df}{dE} \right) \left(\frac{\partial n_R}{\partial E} + \frac{\partial n_L}{\partial E} \right) \Delta\mu. \tag{5.72}$$

Consider now the perfect wire on the right-hand side in fig. 5.7. Since carriers have a transmission probability T, the number of occupied states in the energy range between μ_1 and μ_B is

$$N_{\text{occup}}^{\text{RHS}} = \int dE \left(\frac{-df}{dE} \right) T(E) \frac{\partial n_R}{\partial E} (\mu_1 - \mu_B), \tag{5.73}$$

and the number of unoccupied states between μ_B and μ_2 is

$$N_{\text{empty}}^{\text{RHS}} = \int dE \left(\frac{-df}{dE} \right) \left(\frac{\partial n_R}{\partial E} + \frac{\partial n_L}{\partial E} - T(E) \frac{\partial n_R}{\partial E} \right) (\mu_B - \mu_2). \tag{5.74}$$

Thus, the chemical potential μ_B to the right of the sample is determined by the equation

$$N_{\text{empty}}^{\text{RHS}} = N_{\text{occup}}^{\text{RHS}}, \tag{5.75}$$

and reads

$$\mu_B = \frac{\mu_1 \int dE \left(\frac{-df}{dE} \right) T(E) \frac{\partial n_R}{\partial E} + \mu_2 \int dE \left(\frac{-df}{dE} \right) \left(R(E) \frac{\partial n_R}{\partial E} + \frac{\partial n_L}{\partial E} \right)}{\int dE \left(\frac{-df}{dE} \right) \left(\frac{\partial n_R}{\partial E} + \frac{\partial n_L}{\partial E} \right)}. \tag{5.76}$$

To the left of the barrier we have both incident carriers and reflected carriers. The number of occupied states between μ_1 and μ_A is

$$N_{\text{occup}}^{\text{LHS}} = \int dE \left(\frac{-df}{dE} \right) \left(\frac{\partial n_R}{\partial E} + R(E) \frac{\partial n_L}{\partial E} \right) (\mu_1 - \mu_A), \tag{5.77}$$

and the number of unoccupied states between μ_A and μ_2 is

$$N_{\text{empty}}^{\text{LHS}} = \int dE \left(\frac{-df}{dE} \right) \left(\frac{\partial n_R}{\partial E} + \frac{\partial n_L}{\partial E} - \frac{\partial n_R}{\partial E} - R(E) \frac{\partial n_L}{\partial E} \right) (\mu_A - \mu_2). \tag{5.78}$$

Therefore, the chemical potential μ_A to the left of the sample is determined by

$$N_{\text{empty}}^{\text{LHS}} = N_{\text{occup}}^{\text{LHS}}, \tag{5.79}$$

and reads

$$\mu_A = \frac{\mu_1 \int dE \left(\frac{-df}{dE} \right) \left(\frac{\partial n_R}{\partial E} + R(E) \frac{\partial n_L}{\partial E} \right) + \mu_2 \int dE \left(\frac{-df}{dE} \right) T(E) \frac{\partial n_L}{\partial E}}{\int dE \left(\frac{-df}{dE} \right) \left(\frac{\partial n_R}{\partial E} + \frac{\partial n_L}{\partial E} \right)}. \tag{5.80}$$

Charge neutrality does not allow different densities to the left and to the right of the sample over the distances large compared to the screening length [39]. Thus, the conduction-band bottoms of the perfect wires are displaced against each other by a potential difference

$$eV = \mu_A - \mu_B. \tag{5.81}$$

Therefore, the equations (5.76), (5.80) and (5.81) can be used to determine the relation between the chemical potentials μ_1 and μ_2 and the voltage across the sample. The result of this calculation yields

$$eV = \Delta\mu \frac{\int dE \left(\frac{-df}{dE} \right) R(E) \left(\frac{\partial n_R}{\partial E} + \frac{\partial n_L}{\partial E} \right)}{\int dE \left(\frac{-df}{dE} \right) \left(\frac{\partial n_R}{\partial E} + \frac{\partial n_L}{\partial E} \right)}. \tag{5.82}$$

Thus, the total current between the reservoirs reads

$$I = G_0 \int dE \frac{-df}{dE} T(E) \frac{\int dE \left(\frac{\partial n_R}{\partial E} + \frac{\partial n_L}{\partial E}\right)\left(-\frac{df}{dE}\right)}{\int dE \left(\frac{\partial n_R}{\partial E} + \frac{\partial n_L}{\partial E}\right) R(E)\left(-\frac{df}{dE}\right)} V \qquad (5.83)$$

The conductance of the sample can be easily obtained from this formula using the relation $G = I/V$.

We find it necessary to emphasize that formula (5.83) describes electron transport between two *reservoirs*. If we exclude the reservoirs from our consideration then the voltage drop occurs only at the sample, and $\Delta\mu$ in (5.71) is just equal to eV.

The current (5.83) explicitly depends on the density of states. However, the chiral densities of states $\partial n_L/\partial E$ and $\partial n_R/\partial E$ are incorporated in (5.83) as a sum. The current from the left reservoir to the right one (as it is shown in fig. 5.7) is still equal to the current at the inversal bias voltage, where $\mu_1 < \mu_2$, and the current flows from the *right* to the left. Thus, transport measurements are not very effective for the detection of the chiral asymmetry of the density of states.

Nevertheless, there are definitely some other possibilities to detect the chiral asymmetry of density of states. One of them could be optical measurements [97, 98]. (See the theoretical work [99] as well.) Indeed, the optical absorption in a quantum well is proportional to the density of states. Therefore, we believe, that the observation of the chiral asymmetry is possible in optical measurements using the current experimental technique. However, this goes beyond the scope of the thesis.

6 Conclusions

In this thesis we analyzed some important characteristics of one-dimensional quantum wires with Rashba spin-orbit coupling, especially related to their non-zero curvature.

The major points covered by this thesis may be summarized as follows

- We studied the conductance of a quantum loop made of an one-dimensional wire with Rashba spin-orbit interactions and found that

  - the conductance dependences on the external magnetic field perpendicular to the loop plane can demonstrate a manifestation of the geometrical spin-orbit Berry phase

  - in order to extract the manifestation of the geometrical phase, the comparison with the conductance of a straight wire is, however, necessary

  - the solution obtained suggests its application to the non-adiabatic regime (small loop radius) as well.

- We studied electron transport in a strongly curved one-dimensional wire with Rashba spin-orbit coupling and found the following

  - the system demonstrates current density redistribution between two spin-split modes

  - a strongly curved wire with Rashba spin-orbit coupling can change the spin-polarization of the input electron beam to the opposite one, and, thus, serve as a reflectionless spin-switch.

- We studied the chiral asymmetry of the electron density of states induced by Rashba coupling and Zeeman effect in a curved one-dimensional wire

  - the Tomonaga-Luttinger model has been solved for the lowest non-parabolic Zeeman-split band (the upper bands are assumed to be unoccupied) where the Fermi velocities for left- and right-moving electrons are not equal

  - it has been found that strong electron-electron interactions remedy the chiral symmetry of the density of states

  - the Landauer-Büttiker formalism has been generalized to systems with a chiral asymmetry of the density of states.

In our opinion, the main outcome of this thesis is related to the strongly curved 1D wires with Rashba spin-orbit coupling: namely, such wires can serve in the capacity of reflectionless and high-speed spin-switchers. Indeed, the switching speed is determined by the time needed for an

electron to propagate through the curved part of the system which is very short as long as our device is in the non-adiabatic regime $\hbar^2/(2\alpha m^* R) \gg 1$. Thus, the switching time can be even smaller than one estimated in the Chapter 1 for, let us say, "conventional" spintronic devices in the adiabatic regime.

We believe that the situations treated in this thesis confirm once more how diverse the phenomena related to the Rashba spin-orbit coupling can be. In order to study the great variety of effects we combined spin-orbit interactions in 1D quantum wires with their non-zero curvature, Zeeman splitting and, at the end, with electron-electron interactions. Our main expectation is that the interplay between Rashba spin-orbit coupling and non-trivial geometry of the system can find especially fruitful applications in spintronics.

7 Appendices

7.1 Appendix A

The following system of eight equations describes the electron motion in the quantum loop (see the Chapter 3 for details)

$$(1+A_1)\cos\gamma^+ - i(1-A_2)\sin\gamma^- = e^{-\frac{i\pi}{2}\left(\frac{\Phi}{\Phi_0}-\frac{1}{2}\right)}\left(B_1\cos\alpha^+ e^{-i\pi q_R^+/2} +\right.$$

$$\left. +C_1\cos\beta^+ e^{i\pi q_L^+/2} - B_2\sin\alpha^- e^{-i\pi q_R^-/2} + C_2\sin\beta^- e^{i\pi q_L^-/2}\right),\tag{7.1}$$

$$(1+A_2)\cos\gamma^- - i(1-A_1)\sin\gamma^+ = e^{-\frac{i\pi}{2}\left(\frac{\Phi}{\Phi_0}+\frac{1}{2}\right)}\left(B_2\cos\alpha^- e^{-i\pi q_R^-/2} +\right.$$

$$\left. +C_2\cos\beta^- e^{i\pi q_L^-/2} + B_1\sin\alpha^+ e^{-i\pi q_R^+/2} - C_1\sin\beta^+ e^{i\pi q_L^+/2}\right),\tag{7.2}$$

$$e^{\frac{3i\pi}{2}\left(\frac{\Phi}{\Phi_0}-\frac{1}{2}\right)}\left(B_1\cos\alpha^+ e^{3i\pi q_R^+/2} + C_1\cos\beta^+ e^{-3i\pi q_L^+/2} -\right.$$

$$\left. -B_2\sin\alpha^- e^{3i\pi q_R^-/2} + C_2\sin\beta^- e^{-3i\pi q_L^-/2}\right) = D_1\cos\gamma^+ - iD_2\sin\gamma^-,\tag{7.3}$$

$$e^{\frac{3i\pi}{2}\left(\frac{\Phi}{\Phi_0}+\frac{1}{2}\right)}\left(B_2\cos\alpha^- e^{3i\pi q_R^-/2} + C_2\cos\beta^- e^{-3i\pi q_L^-/2} +\right.$$

$$\left. +B_1\sin\alpha^+ e^{3i\pi q_R^+/2} - C_1\sin\beta^+ e^{-3i\pi q_L^+/2}\right) = D_2\cos\gamma^- - iD_1\sin\gamma^+,\tag{7.4}$$

$$\left[k^+ + \frac{\Phi}{R\Phi_0} + A_1\left(-k^+ + \frac{\Phi}{R\Phi_0}\right)\right]\cos\gamma^+ - i\left[k^- + \frac{\Phi}{R\Phi_0} - A_2\left(-k^- + \frac{\Phi}{R\Phi_0}\right)\right]\sin\gamma^- =$$

$$= \frac{1}{R}e^{-\frac{i\pi}{2}\left(\frac{\Phi}{\Phi_0}-\frac{1}{2}\right)}\left[B_1\left(\frac{\Phi}{\Phi_0} + q_R^+ - \frac{1}{2}\right)\cos\alpha^+ e^{-i\pi q_R^+/2} + C_1\left(\frac{\Phi}{\Phi_0} - \frac{1}{2} - q_L^+\right)\cos\beta^+ e^{i\pi q_L^+/2} -\right.$$

$$\left. -B_2\left(\frac{\Phi}{\Phi_0} - \frac{1}{2} + q_R^-\right)\sin\alpha^- e^{-i\pi q_R^-/2} + C_2\left(\frac{\Phi}{\Phi_0} - \frac{1}{2} - q_L^-\right)\sin\beta^- e^{i\pi q_L^-/2}\right],\tag{7.5}$$

$$\left[k^- + \frac{\Phi}{R\Phi_0} + A_2\left(-k^- + \frac{\Phi}{R\Phi_0}\right)\right]\cos\gamma^- - i\left[k^+ + \frac{\Phi}{R\Phi_0} - A_1\left(-k^+ + \frac{\Phi}{R\Phi_0}\right)\right]\sin\gamma^+ =$$

$$= \frac{1}{R}e^{-\frac{i\pi}{2}\left(\frac{\Phi}{\Phi_0}+\frac{1}{2}\right)}\left[B_2\left(\frac{1}{2} + q_R^- + \frac{\Phi}{\Phi_0}\right)\cos\alpha^- e^{-i\pi q_R^-/2} + C_2\left(\frac{1}{2} - q_L^- + \frac{\Phi}{\Phi_0}\right)\cos\beta^- e^{i\pi q_L^-/2} +\right.$$

$$\left. +B_1\left(\frac{1}{2} + q_R^+ + \frac{\Phi}{\Phi_0}\right)\sin\alpha^+ e^{-i\pi q_R^+/2} - C_1\left(\frac{1}{2} - q_L^+ + \frac{\Phi}{\Phi_0}\right)\sin\beta^+ e^{i\pi q_L^+/2}\right],\tag{7.6}$$

$$\frac{1}{R}e^{\frac{3i\pi}{2}\left(\frac{\Phi}{\Phi_0}-\frac{1}{2}\right)}\left[B_1\left(\frac{\Phi}{\Phi_0}-\frac{1}{2}+q_R^+\right)\cos\alpha^+ e^{3i\pi q_R^+/2}+C_1\left(\frac{\Phi}{\Phi_0}-\frac{1}{2}-q_L^+\right)\cos\beta^+ e^{-3i\pi q_L^+/2}-\right.$$

$$\left.-B_2\left(\frac{\Phi}{\Phi_0}-\frac{1}{2}+q_R^-\right)\sin\alpha^- e^{3i\pi q_R^-/2}+C_2\left(\frac{\Phi}{\Phi_0}-\frac{1}{2}-q_L^-\right)\sin\beta^- e^{-3i\pi q_L^-/2}\right]=$$

$$=D_1\left(k^++\frac{\Phi}{R\Phi_0}\right)\cos\gamma^+ -iD_2\left(k^-+\frac{\Phi}{R\Phi_0}\right)\sin\gamma^-,\tag{7.7}$$

$$\frac{1}{R}e^{\frac{3i\pi}{2}\left(\frac{\Phi}{\Phi_0}+\frac{1}{2}\right)}\left[B_2\left(\frac{1}{2}+q_R^-+\frac{\Phi}{\Phi_0}\right)\cos\alpha^- e^{3i\pi q_R^-/2}+C_2\left(\frac{1}{2}-q_L^-+\frac{\Phi}{\Phi_0}\right)\cos\beta^- e^{-3i\pi q_L^-/2}+\right.$$

$$\left.+B_1\left(\frac{1}{2}+q_R^++\frac{\Phi}{\Phi_0}\right)\sin\alpha^+ e^{3i\pi q_R^+/2}-C_1\left(\frac{1}{2}-q_L^++\frac{\Phi}{\Phi_0}\right)\sin\beta^+ e^{-3i\pi q_L^+/2}\right]=$$

$$=D_2\left(k^-+\frac{\Phi}{R\Phi_0}\right)\cos\gamma^- -iD_1\left(k^++\frac{\Phi}{R\Phi_0}\right)\sin\gamma^+.\tag{7.8}$$

The system of equations describing the electron motion in the curved, half-loop shaped one-dimensional wire, reads

$$\left(e^{i\theta^+}+A^+\right)\cos\gamma^+ -i\left(e^{i\theta^-}-A^-\right)\sin\gamma^- = e^{-\frac{i\pi}{2}\left(\frac{\Phi}{\Phi_0}-\frac{1}{2}\right)}\left(B^+\cos\alpha^+ e^{-i\pi q_R^+/2}+\right.$$

$$\left.+C^+\cos\beta^+ e^{i\pi q_L^+/2}-B^-\sin\alpha^- e^{-i\pi q_R^-/2}+C^-\sin\beta^- e^{i\pi q_L^-/2}\right),\tag{7.9}$$

$$\left(e^{i\theta^-}+A^-\right)\cos\gamma^- -i\left(e^{i\theta^+}-A^+\right)\sin\gamma^+ = e^{-\frac{i\pi}{2}\left(\frac{\Phi}{\Phi_0}+\frac{1}{2}\right)}\left(B^-\cos\alpha^- e^{-i\pi q_R^-/2}+\right.$$

$$\left.+C^-\cos\beta^- e^{i\pi q_L^-/2}+B^+\sin\alpha^+ e^{-i\pi q_R^+/2}-C^+\sin\beta^+ e^{i\pi q_L^+/2}\right),\tag{7.10}$$

$$e^{\frac{i\pi}{2}\left(\frac{\Phi}{\Phi_0}-\frac{1}{2}\right)}\left(B^+\cos\alpha^+ e^{i\pi q_R^+/2}+C^+\cos\beta^+ e^{-i\pi q_L^+/2}-\right.$$

$$\left.-B^-\sin\alpha^- e^{i\pi q_R^-/2}+C^-\sin\beta^- e^{-i\pi q_L^-/2}\right)=D^+\cos\gamma^+ +iD^-\sin\gamma^-,\tag{7.11}$$

$$e^{\frac{i\pi}{2}\left(\frac{\Phi}{\Phi_0}+\frac{1}{2}\right)}\left(B^-\cos\alpha^- e^{i\pi q_R^-/2}+C^-\cos\beta^- e^{-i\pi q_L^-/2}+\right.$$

$$\left.+B^+\sin\alpha^+ e^{i\pi q_R^+/2}-C^+\sin\beta^+ e^{-i\pi q_L^+/2}\right)=D^-\cos\gamma^- +iD^+\sin\gamma^+,\tag{7.12}$$

$$\left[\left(k^++\frac{\Phi}{R\Phi_0}\right)e^{i\theta^+}+A^+\left(\frac{\Phi}{R\Phi_0}-k^+\right)\right]\cos\gamma^+ -$$

$$-i\left[\left(k^-+\frac{\Phi}{R\Phi_0}\right)e^{i\theta^-}-A^-\left(\frac{\Phi}{R\Phi_0}-k^-\right)\right]\sin\gamma^- =$$

$$=\frac{1}{R}e^{-\frac{i\pi}{2}\left(\frac{\Phi}{\Phi_0}-\frac{1}{2}\right)}\left[B^+\left(\frac{\Phi}{\Phi_0}+q_R^+-\frac{1}{2}\right)\cos\alpha^+ e^{-i\pi q_R^+/2}+C^+\left(\frac{\Phi}{\Phi_0}-\frac{1}{2}-q_L^+\right)\cos\beta^+ e^{i\pi q_L^+/2}-\right.$$

$$\left.-B^-\left(\frac{\Phi}{\Phi_0}-\frac{1}{2}+q_R^-\right)\sin\alpha^- e^{-i\pi q_R^-/2}+C^-\left(\frac{\Phi}{\Phi_0}-\frac{1}{2}-q_L^-\right)\sin\beta^- e^{i\pi q_L^-/2}\right],\tag{7.13}$$

$$\left[\left(k^-+\frac{\Phi}{R\Phi_0}\right)e^{i\theta^-}+A^-\left(\frac{\Phi}{R\Phi_0}-k^-\right)\right]\cos\gamma^--$$

$$-i\left[\left(k^++\frac{\Phi}{R\Phi_0}\right)e^{i\theta^+}-A^+\left(\frac{\Phi}{R\Phi_0}-k^+\right)\right]\sin\gamma^+=$$

$$=\frac{1}{R}e^{-\frac{i\pi}{2}\left(\frac{\Phi}{\Phi_0}+\frac{1}{2}\right)}\left[B^-\left(\frac{1}{2}+q_R^-+\frac{\Phi}{\Phi_0}\right)\cos\alpha^-\,e^{-i\pi q_R^-/2}+C^-\left(\frac{1}{2}-q_L^-+\frac{\Phi}{\Phi_0}\right)\cos\beta^-\,e^{i\pi q_L^-/2}+\right.$$

$$\left.+B^+\left(\frac{1}{2}+q_R^++\frac{\Phi}{\Phi_0}\right)\sin\alpha^+\,e^{-i\pi q_R^+/2}-C^+\left(\frac{1}{2}-q_L^++\frac{\Phi}{\Phi_0}\right)\sin\beta^+\,e^{i\pi q_L^+/2}\right], \tag{7.14}$$

$$\frac{1}{R}e^{\frac{i\pi}{2}\left(\frac{\Phi}{\Phi_0}-\frac{1}{2}\right)}\left[B^+\left(\frac{\Phi}{\Phi_0}-\frac{1}{2}+q_R^+\right)\cos\alpha^+\,e^{i\pi q_R^+/2}+C^+\left(\frac{\Phi}{\Phi_0}-\frac{1}{2}-q_L^+\right)\cos\beta^+\,e^{-i\pi q_L^+/2}-\right.$$

$$\left.-B^-\left(\frac{\Phi}{\Phi_0}-\frac{1}{2}+q_R^-\right)\sin\alpha^-\,e^{i\pi q_R^-/2}+C^-\left(\frac{\Phi}{\Phi_0}-\frac{1}{2}-q_L^-\right)\sin\beta^-\,e^{-i\pi q_L^-/2}\right]=$$

$$=D^+\left(k^++\frac{\Phi}{R\Phi_0}\right)\cos\gamma^++iD^-\left(k^-+\frac{\Phi}{R\Phi_0}\right)\sin\gamma^-, \tag{7.15}$$

$$\frac{1}{R}e^{\frac{i\pi}{2}\left(\frac{\Phi}{\Phi_0}+\frac{1}{2}\right)}\left[B^-\left(\frac{1}{2}+q_R^-+\frac{\Phi}{\Phi_0}\right)\cos\alpha^-\,e^{i\pi q_R^-/2}+C^-\left(\frac{1}{2}-q_L^-+\frac{\Phi}{\Phi_0}\right)\cos\beta^-\,e^{-i\pi q_L^-/2}+\right.$$

$$\left.+B^+\left(\frac{1}{2}+q_R^++\frac{\Phi}{\Phi_0}\right)\sin\alpha^+\,e^{i\pi q_R^+/2}-C^+\left(\frac{1}{2}-q_L^++\frac{\Phi}{\Phi_0}\right)\sin\beta^+\,e^{-i\pi q_L^+/2}\right]=$$

$$=D^-\left(k^-+\frac{\Phi}{R\Phi_0}\right)\cos\gamma^-+iD^+\left(k^++\frac{\Phi}{R\Phi_0}\right)\sin\gamma^+. \tag{7.16}$$

As soon as the initial electron state is +100% spin-polarized, the equations (7.9) – (7.16) take the form

$$\left(e^{i\theta^+}+A^+\right)\cos\gamma^++iA^-\sin\gamma^-=e^{-\frac{i\pi}{2}\left(\frac{\Phi}{\Phi_0}-\frac{1}{2}\right)}\left(B^+\cos\alpha^+\,e^{-i\pi q_R^+/2}+\right.$$

$$\left.+C^+\cos\beta^+\,e^{i\pi q_L^+/2}-B^-\sin\alpha^-\,e^{-i\pi q_R^-/2}+C^-\sin\beta^-\,e^{i\pi q_L^-/2}\right), \tag{7.17}$$

$$A^-\cos\gamma^--i\left(e^{i\theta^+}-A^+\right)\sin\gamma^+=e^{-\frac{i\pi}{2}\left(\frac{\Phi}{\Phi_0}+\frac{1}{2}\right)}\left(B^-\cos\alpha^-\,e^{-i\pi q_R^-/2}+\right.$$

$$\left.+C^-\cos\beta^-\,e^{i\pi q_L^-/2}+B^+\sin\alpha^+\,e^{-i\pi q_R^+/2}-C^+\sin\beta^+\,e^{i\pi q_L^+/2}\right), \tag{7.18}$$

$$e^{\frac{i\pi}{2}\left(\frac{\Phi}{\Phi_0}-\frac{1}{2}\right)}\left(B^+\cos\alpha^+\,e^{i\pi q_R^+/2}+C^+\cos\beta^+\,e^{-i\pi q_L^+/2}-\right.$$

$$\left.-B^-\sin\alpha^-\,e^{i\pi q_R^-/2}+C^-\sin\beta^-\,e^{-i\pi q_L^-/2}\right)=D^+\cos\gamma^++iD^-\sin\gamma^-, \tag{7.19}$$

$$e^{\frac{i\pi}{2}\left(\frac{\Phi}{\Phi_0}+\frac{1}{2}\right)}\left(B^-\cos\alpha^-\,e^{i\pi q_R^-/2}+C^-\cos\beta^-\,e^{-i\pi q_L^-/2}+\right.$$

$$\left.+B^+\sin\alpha^+\,e^{i\pi q_R^+/2}-C^+\sin\beta^+\,e^{-i\pi q_L^+/2}\right)=D^-\cos\gamma^-+iD^+\sin\gamma^+, \tag{7.20}$$

$$\left[e^{i\theta^+}\left(k^+ + \frac{\Phi}{R\Phi_0}\right) + A^+\left(-k^+ + \frac{\Phi}{R\Phi_0}\right)\right]\cos\gamma^+ + iA^-\left(-k^- + \frac{\Phi}{R\Phi_0}\right)\sin\gamma^- =$$

$$= \frac{1}{R}e^{-\frac{i\pi}{2}\left(\frac{\Phi}{\Phi_0}-\frac{1}{2}\right)}\left[B^+\left(\frac{\Phi}{\Phi_0}+q_R^+ - \frac{1}{2}\right)\cos\alpha^+ e^{-i\pi q_R^+/2} + C^+\left(\frac{\Phi}{\Phi_0}-\frac{1}{2}-q_L^+\right)\cos\beta^+ e^{i\pi q_L^+/2}-\right.$$

$$\left.- B^-\left(\frac{\Phi}{\Phi_0}-\frac{1}{2}+q_R^-\right)\sin\alpha^-\,e^{-i\pi q_R^-/2} + C^-\left(\frac{\Phi}{\Phi_0}-\frac{1}{2}-q_L^-\right)\sin\beta^-\,e^{i\pi q_L^-/2}\right], \tag{7.21}$$

$$A^-\left(-k^- + \frac{\Phi}{R\Phi_0}\right)\cos\gamma^- - i\left[e^{i\theta^+}\left(k^+ + \frac{\Phi}{R\Phi_0}\right) - A^+\left(-k^+ + \frac{\Phi}{R\Phi_0}\right)\right]\sin\gamma^+ =$$

$$= \frac{1}{R}e^{-\frac{i\pi}{2}\left(\frac{\Phi}{\Phi_0}+\frac{1}{2}\right)}\left[B^-\left(\frac{1}{2}+q_R^- + \frac{\Phi}{\Phi_0}\right)\cos\alpha^-\,e^{-i\pi q_R^-/2} + C^-\left(\frac{1}{2}-q_L^- + \frac{\Phi}{\Phi_0}\right)\cos\beta^-\,e^{i\pi q_L^-/2}+\right.$$

$$\left.+ B^+\left(\frac{1}{2}+q_R^+ + \frac{\Phi}{\Phi_0}\right)\sin\alpha^+\,e^{-i\pi q_R^+/2} - C^+\left(\frac{1}{2}-q_L^+ + \frac{\Phi}{\Phi_0}\right)\sin\beta^+\,e^{i\pi q_L^+/2}\right], \tag{7.22}$$

$$\frac{1}{R}e^{\frac{i\pi}{2}\left(\frac{\Phi}{\Phi_0}-\frac{1}{2}\right)}\left[B^+\left(\frac{\Phi}{\Phi_0}-\frac{1}{2}+q_R^+\right)\cos\alpha^+ e^{i\pi q_R^+/2} + C^+\left(\frac{\Phi}{\Phi_0}-\frac{1}{2}-q_L^+\right)\cos\beta^+ e^{-i\pi q_L^+/2}-\right.$$

$$\left.- B^-\left(\frac{\Phi}{\Phi_0}-\frac{1}{2}+q_R^-\right)\sin\alpha^-\,e^{i\pi q_R^-/2} + C^-\left(\frac{\Phi}{\Phi_0}-\frac{1}{2}-q_L^-\right)\sin\beta^-\,e^{-i\pi q_L^-/2}\right] =$$

$$= D^+\left(k^+ + \frac{\Phi}{R\Phi_0}\right)\cos\gamma^+ + iD^-\left(k^- + \frac{\Phi}{R\Phi_0}\right)\sin\gamma^-, \tag{7.23}$$

$$\frac{1}{R}e^{\frac{i\pi}{2}\left(\frac{\Phi}{\Phi_0}+\frac{1}{2}\right)}\left[B^-\left(\frac{1}{2}+q_R^- + \frac{\Phi}{\Phi_0}\right)\cos\alpha^-\,e^{i\pi q_R^-/2} + C^-\left(\frac{1}{2}-q_L^- + \frac{\Phi}{\Phi_0}\right)\cos\beta^-\,e^{-i\pi q_L^-/2}+\right.$$

$$\left.+ B^+\left(\frac{1}{2}+q_R^+ + \frac{\Phi}{\Phi_0}\right)\sin\alpha^+\,e^{i\pi q_R^+/2} - C^+\left(\frac{1}{2}-q_L^+ + \frac{\Phi}{\Phi_0}\right)\sin\beta^+\,e^{-i\pi q_L^+/2}\right] =$$

$$= D^-\left(k^- + \frac{\Phi}{R\Phi_0}\right)\cos\gamma^- + iD^+\left(k^+ + \frac{\Phi}{R\Phi_0}\right)\sin\gamma^+. \tag{7.24}$$

The initial phases $\theta^\pm$ of the incident waves are explicitly included into the equations (7.9) – (7.24). (See the Chapter 4 for details.)

7.2 Appendix B

The explicit expressions for the elements of the matrices S_Φ, S_Θ, S_Φ^{-1}, S_Θ^{-1} read

$$S_\Phi^{11} = -\sqrt{\frac{g_2 b}{\lambda_1}}\sqrt{\frac{\varepsilon_1}{DD_2}} - \frac{d-a+\sqrt{D_2}}{2\sqrt{b}}\sqrt{\frac{g_2}{\lambda_2}}\sqrt{\frac{\varepsilon_1}{DD_2}}, \tag{7.25}$$

$$S_\Phi^{12} = \sqrt{\frac{g_2 b}{\lambda_1}}\sqrt{\frac{\varepsilon_2}{DD_2}} - \frac{a-d+\sqrt{D_2}}{2\sqrt{b}}\sqrt{\frac{g_2}{\lambda_2}}\sqrt{\frac{\varepsilon_2}{DD_2}}, \tag{7.26}$$

$$S_\Phi^{21} = \frac{1-g+\sqrt{D}}{2\sqrt{g_2}}\sqrt{\frac{b}{\lambda_1}}\sqrt{\frac{\varepsilon_1}{DD_2}} + \frac{(1-g-\sqrt{D})(d-a+\sqrt{D_2})}{4\sqrt{\lambda_2 g_2 b}}\left(\frac{\varepsilon_1}{DD_2}\right)^{\frac{1}{4}}, \tag{7.27}$$

$$S_\Phi^{22} = -\frac{1-g+\sqrt{D}}{2\sqrt{g_2}}\sqrt{\frac{b}{\lambda_1}\sqrt{\frac{\varepsilon_2}{DD_2}}} + \frac{(1-g-\sqrt{D})(a-d+\sqrt{D_2})}{4\sqrt{\lambda_2 g_2 b}}\left(\frac{\varepsilon_2}{DD_2}\right)^{\frac{1}{4}}, \qquad (7.28)$$

$$\left(S_\Phi^{11}\right)^{-1} = \frac{(a-d+\sqrt{D_2})(1-g-\sqrt{D})}{4\sqrt{bg_2\lambda_1}}\left(\frac{\varepsilon_1}{DD_2}\right)^{\frac{1}{4}} + \frac{(g-1-\sqrt{D})\sqrt{b}}{2\sqrt{g_2\lambda_2}}\left(\frac{\varepsilon_1}{DD_2}\right)^{\frac{1}{4}}, \qquad (7.29)$$

$$\left(S_\Phi^{12}\right)^{-1} = \frac{(a-d+\sqrt{D_2})\sqrt{g_2}}{2\sqrt{b\lambda_1}}\left(\frac{\varepsilon_1}{DD_2}\right)^{\frac{1}{4}} - \sqrt{\frac{g_2 b}{\lambda_2}\sqrt{\frac{\varepsilon_1}{DD_2}}}, \qquad (7.30)$$

$$\left(S_\Phi^{21}\right)^{-1} = \frac{(a-d-\sqrt{D_2})(1-g-\sqrt{D})}{4\sqrt{bg_2\lambda_1}}\left(\frac{\varepsilon_2}{DD_2}\right)^{\frac{1}{4}} + \frac{(g-1-\sqrt{D})\sqrt{b}}{2\sqrt{g_2\lambda_2}}\left(\frac{\varepsilon_2}{DD_2}\right)^{\frac{1}{4}}, \qquad (7.31)$$

$$\left(S_\Phi^{22}\right)^{-1} = \frac{(a-d-\sqrt{D_2})\sqrt{g_2}}{2\sqrt{b\lambda_1}}\left(\frac{\varepsilon_2}{DD_2}\right)^{\frac{1}{4}} - \sqrt{\frac{g_2 b}{\lambda_2}\sqrt{\frac{\varepsilon_2}{DD_2}}}, \qquad (7.32)$$

$$S_\Theta^{11} = -\sqrt{\frac{\lambda_1 g_2 b}{\sqrt{\varepsilon_1 DD_2}}} - \frac{d-a+\sqrt{D_2}}{2\sqrt{b}}\sqrt{\frac{g_2\lambda_2}{\sqrt{\varepsilon_1 DD_2}}}, \qquad (7.33)$$

$$S_\Theta^{12} = \sqrt{\frac{\lambda_1 g_2 b}{\sqrt{\varepsilon_2 DD_2}}} - \frac{a-d+\sqrt{D_2}}{2\sqrt{b}}\sqrt{\frac{g_2\lambda_2}{\sqrt{\varepsilon_2 DD_2}}}, \qquad (7.34)$$

$$S_\Theta^{21} = \frac{1-g+\sqrt{D}}{2\sqrt{g_2}}\sqrt{\frac{b\lambda_1}{\sqrt{\varepsilon_1 DD_2}}} + \frac{\sqrt{\lambda_2}(1-g-\sqrt{D})(d-a+\sqrt{D_2})}{4\sqrt{g_2 b\sqrt{\varepsilon_1 DD_2}}}, \qquad (7.35)$$

$$S_\Theta^{22} = -\frac{1-g+\sqrt{D}}{2\sqrt{g_2}}\sqrt{\frac{b\lambda_1}{\sqrt{\varepsilon_2 DD_2}}} + \frac{\sqrt{\lambda_2}(1-g-\sqrt{D})(a-d+\sqrt{D_2})}{4\sqrt{g_2 b\sqrt{\varepsilon_2 DD_2}}}, \qquad (7.36)$$

$$\left(S_\Theta^{11}\right)^{-1} = \frac{(a-d+\sqrt{D_2})(1-g-\sqrt{D})\sqrt{\lambda_1}}{4\sqrt{bg_2\sqrt{\varepsilon_1 DD_2}}} + \frac{(g-1-\sqrt{D})\sqrt{b\lambda_2}}{2\sqrt{g_2\sqrt{\varepsilon_1 DD_2}}}, \qquad (7.37)$$

$$\left(S_\Theta^{12}\right)^{-1} = \frac{(a-d+\sqrt{D_2})\sqrt{g_2\lambda_1}}{2\sqrt{b\sqrt{\varepsilon_1 DD_2}}} - \sqrt{\frac{g_2 b\lambda_2}{\sqrt{\varepsilon_1 DD_2}}}, \qquad (7.38)$$

$$\left(S_\Theta^{21}\right)^{-1} = \frac{(a-d-\sqrt{D_2})(1-g-\sqrt{D})\sqrt{\lambda_1}}{4\sqrt{bg_2\sqrt{\varepsilon_2 DD_2}}} + \frac{(g-1-\sqrt{D})\sqrt{b\lambda_2}}{2\sqrt{g_2\sqrt{\varepsilon_2 DD_2}}}, \qquad (7.39)$$

$$\left(S_\Theta^{22}\right)^{-1} = \frac{(a-d-\sqrt{D_2})\sqrt{g_2\lambda_1}}{2\sqrt{b\sqrt{\varepsilon_2 DD_2}}} - \sqrt{\frac{g_2 b\lambda_2}{\sqrt{\varepsilon_2 DD_2}}}. \qquad (7.40)$$

Here,

$$a = \lambda_1\left[\frac{1+g}{2} + g_4 - \frac{(1-g)^2 - 4g_2^2}{2\sqrt{D}}\right],$$

98

$$b = \sqrt{\lambda_1 \lambda_2} \left[(1-g) - \frac{(1-g)^2}{\sqrt{D}} \right],$$

$$c = \sqrt{\lambda_1 \lambda_2} \left[(1-g) + \frac{(1-g)^2}{\sqrt{D}} \right],$$

$$d = \lambda_2 \left[\frac{1+g}{2} + g_4 + \frac{(1-g)^2 - 4g_2^2}{2\sqrt{D}} \right],$$

$$\varepsilon_{1,2} = \frac{a + d \pm \sqrt{D_2}}{2},$$

$$\lambda_{1,2} = \frac{1+g}{2} + g_4 \mp \frac{1}{2}\sqrt{D},$$

and $D_2 = (a-d)^2 + 4bc$, $D = (1-g)^2 + 4g_2^2$, $g = v_L^- / v_R^-$, and $g_{2,4}$ being the interaction constants.

Bibliography

[1] S. A. Wolf, D. D. Awschalom, R. A. Buhrman, J. M. Daughton, S. von Molnar, M. L. Roukes, A. Y. Chtchelkanova, and D. M. Treger. Spintronics: A spin-based electronics vision for the future. *Science*, 294:1488, 2001.

[2] G. Gilder. Fiber keps its promise. Technical report, Gilder Technology Report, 1997.

[3] A. L. Chudnovskiy. Spintronics, 2004. Lectures given at Hamburg University.

[4] Yu.A. Bychkov and E.I. Rashba. Properties of 2D electron gas with lifted spectral degeneracy. *JEPT Letters*, 39:78, 1984.

[5] Yu.A. Bychkov and E.I. Rashba. Oscillatory effects and the magnetic susceptibility of carriers in inversion layers. *J. Phys. C*, 17:6039–6045, 1984.

[6] G. Engels, J. Lange, Th. Schäpers, and H. Lüth. Experimental and theoretical approach to spin splitting in modulation-doped $In_xGa_{1-x}As/InP$ quantum wells for $B \rightarrow 0$. *Phys. Rev. B*, 55:1958, 1997.

[7] C.-M. Hu, J. Nitta, T. Akazaki, H. Takayanagi, P. Pfeffer, and W. Zawadzki. Zero-field spin splitting in an inverted $In_{0.53}Ga_{0.47}As/In_{0.52}Al_{0.48}As$ heterostructure: Band nonparabolicity influence and the subband dependence. *Phys. Rev. B*, 60:7736, 1999.

[8] T. Matsuyama, R. Kürsten, C. Meissner, and U. Merkt. Rashba spin splitting in inversion layers on p-type bulk InAs. *Phys. Rev. B*, 61:15588, 2000.

[9] J. Nitta, T. Akazaki, H. Takayanagi, and T. Enoki. Gate control of spin-orbit interaction in an inverted $In_{0.53}Ga_{0.47}As/In_{0.52}Al_{0.48}As$ heterostructure. *Phys. Rev. Letters*, 78:1335, 1997.

[10] J. P. Heida, B. J. van Wees, J. J. Kuipers, and T. M. Klapwijk. Spin-orbit interaction in a two-dimensional electron gas in a InAs/AlSb quantum well with gate-controlled electron density. *Phys. Rev. B*, 57:11911, 1998.

[11] D. Grundler. Large Rashba splitting in InAs quantum wells due to electron wave function penetration into the barrier layers. *Phys. Rev. Letters*, 84:6074, 2000.

[12] D. Loss, Paul M. Goldbart, and A.V. Balatsky. Berry's phase and persistent charge and spin currents in textured mesoscopic rings. *Phys. Rev. Letters*, 65:1655–1658, 1990.

[13] A.G. Aronov and Y.B. Lyanda-Geller. Spin-orbit Berry phase in conducting rings. *Phys. Rev. Letters*, 70:343–346, 1993.

[14] F. E. Meijer, A. F. Morpurgo, and T. M. Klapwijk. One-dimensional ring in the presence of Rashba spin-orbit interaction: Derivation of the correct Hamiltonian. *Phys. Rev. B*, 66:033107, 2002.

[15] M.V. Berry. Quantal phase factors accompanying adiabatic changes. *Proc. Soc. Lond. A*, 392:45–57, 1984.

[16] A. Shapere and F. Wilczek, editors. *Geometric Phases in Physics*. World Scientific, Singapore, 1989.

[17] Y. Aharonov and J. Anandan. Phase change during a cyclic quantum evolution. *Phys. Rev. Letters*, 58:1593–1596, 1987.

[18] D. Loss and P. Goldbart. Persistent currents from Berry's phase in mesoscopic systems. *Phys. Rev. B*, 45:13544–13561, 1990.

[19] A. Stern. Berry's phase, motive forces, and mesoscopic conductivity. *Phys. Rev. Letters*, 68:1022–1025, 1992.

[20] Y. Lyanda-Geller, I.L. Aleiner, and Paul M. Goldbart. Domain walls and conductivity of mesoscopic ferromagnets. *Phys. Rev. Letters*, 81:3215–3218, 1998.

[21] H.-A.Engel and D. Loss. Conductance fluctuations in diffusive rings: Berry phase effects and criteria for adiabaticity. *Phys. Rev. B*, 62:10238–10254, 2000.

[22] Diego Frustaglia, Martina Hentschel, and Klaus Richter. Quantum transport in nonuniform magnetic fields: Aharonov-Bohm ring as a spin switch. *Phys. Rev. Letters*, 87:256602, 2001.

[23] D. Frustaglia and K. Richter. Spin interference effects in ring conductors subject to Rashba coupling. *Phys. Rev. B*, 69:235310, 2004.

[24] Markus Popp, Diego Frustaglia, and Klaus Richter. Conditions for adiabatic spin transport in disordered systems. *Phys. Rev. B*, 68:041303, 2003.

[25] M. Hentschel, H. Schomerus, D. Frustaglia, and K. Richter. Aharonov-Bohm physics with spin i: Geometric Phases in One-dimensional Ballistic Rings. *Phys. Rev. B*, 69:155326, 2004.

[26] M. Hentschel, D. Frustaglia, and K. Richter. Aharonov-Bohm physics with spin ii: Spin-flip effects in two-dimensional ballistic systems. *Phys. Rev. B*, 69:155327, 2004.

[27] Y. Aharonov and D. Bohm. Significance of electromagnetic potentials in the quantum theory. *Phys. Rev.*, 115:485–491, 1959.

[28] Yi-Chang Zhou, Hua-Zhong Li, and Xun Xue. Spin-orbit coupling in one-dimensional conducting rings. *Phys. Rev. B*, 49:14010–14011, 1994.

[29] Y. Lyanda-Geller. Topological transitions in Berry's phase interference effects. *Phys. Rev. Letters*, 71:657–661, 1993.

[30] Tie-Zheng Qian and Zhao-Bin Su. Spin-orbit interaction and Aharonov-Anandan phase in mesoscopic rings. *Phys. Rev. Letters*, 72:2311–2315, 1994.

[31] A.G. Mal'shukov, V.V. Shlyapin, and K.A. Chao. Effect of the spin-orbit geometric phase on the spectrum of Aharonov-Bohm oscillations in a semiconductor mesoscopic ring. *Phys. Rev. B*, 60:R2161–R2164, 1999.

[32] A. F. Morpurgo, J. P. Heida, T. M. Klapwijk, B. J. van Wees, and G. Borghs. Ensemble-average spectrum of Aharonov-Bohm conductance oscillations: Evidence for spin-orbit-induced Berry's phase. *Phys. Rev. Letters*, 80:1050–1053, 1998.

[33] J. Nitta, H. Takayanagi, and S. Calvet. Magnetoresistance oscillations in an Aharonov-Bohm ring using two-dimensional electron gas InAs. *Microelectron. Eng.*, 47:85, 1999.

[34] Jeng-Bang Yau, E. P. De Poortere, and M. Shayegan. Aharonov-Bohm oscillations with spin: Evidence for Berry s phase. *Phys. Rev. Letters*, 88:146801–146804, 2002.

[35] M.J. Yang, C.H. Yang, and Y.B. Lyanda-Geller. Quantum beating in the conductance of ballistic rings. *Physica E*, 22:304–307, 2004.

[36] M.J. Yang, C.H. Yang, and Y.B. Lyanda-Geller. Quantum beating in the conductance: observation of spin chiral states and Berry's phase. *Europhysics Letters*, 66:826–832, 2004.

[37] M. Büttiker, Y. Imry, and M. Ya. Azbel. Quantum oscillations in one-dimensional normal-metal rings. *Phys. Rev. A*, 30:1982–1989, 1984.

[38] R. Landauer and M. Büttiker. Resistance of small metallic loops. *Phys. Rev. Letters*, 54:2049–2052, 1985.

[39] M. Büttiker, Y. Imry, R. Landauer, and S. Pinhas. Generalized many-channel conductance formula with application to small rings. *Phys. Rev. B*, 31:6207–6215, 1985.

[40] Hans De Raedt. Comment on "Ensemble-average spectrum of Aharonov-Bohm conductance oscillations: Evidence for spin-orbit-induced Berry's phase". *Phys. Rev. Letters*, 83:1700, 1999.

[41] A. F. Morpurgo, J. P. Heida, T. M. Klapwijk, B. J. van Wees, and G. Borghs. Reply to De Raedt. *Phys. Rev. Letters*, 83:1701, 1999.

[42] A.G. Mal'shukov and K. A. Chao. Comment on "Aharonov-Bohm oscillations with spin: Evidence for Berry's phase". *Phys. Rev. Letters*, 90:179701, 2003.

[43] Jeng-Bang Yau, E. P. De Poortere, and M. Shayegan. Reply to Mal'shukov et al. *Phys. Rev. Letters*, 90:179702, 2003.

[44] A. G. Wagh and V. Ch. Rakhecha. Comment on "Aharonov-Bohm oscillations with spin: Evidence for Berry's phase". *Phys. Rev. Letters*, 90:119703, 2003.

[45] Jeng-Bang Yau, E. P. De Poortere, and M. Shayegan. Reply to Wagh et al. *Phys. Rev. Letters*, 90:119704, 2003.

[46] S. Datta and B. Das. Electronic analog of the electro-optic modulator. *Appl. Phys. Letters*, 56:665–667, 1990.

[47] A. Hirohata, S. J. Steinmueller, W. S. Cho, Y. B. Xu, C. M. Guertler, G. Wastlbauer, J. A. C. Bland, and S. N. Holmes. Ballistic spin filtering across ferromagnet/semiconductor interfaces at room temperature. *Phys. Rev. B*, 66:035330, 2002.

[48] S. E. Andresen, S. J. Steinmuller, A. Ionescu, G. Wastlbauer, C. M. Guertler, and J. A. C. Bland. Role of electron tunneling in spin filtering at ferromagnet/semiconductor interfaces. *Phys. Rev. B*, 68:073303, 2003.

[49] S. D. Ganichev, E. L. Ivchenko, S. N. Danilov, J. Eroms, W. Wegscheider, D. Weiss, and W. Prettl. Conversion of spin into directed electric current in quantum wells. *Phys. Rev. Letters*, 86:4358–4361, 2001.

[50] L. P. Rokhinson, V. Larkina, Y. B. Lyanda-Geller, L. N. Pfeiffer, and K. W. West. Spin separation in cyclotron motion. *Phys. Rev. Letters*, 93:146601, 2004.

[51] Erasmo A. de Andrada e Silva and Giuseppe C. La Rocca. Electron-spin polarization by resonant tunneling. *Phys. Rev. B*, 59:R15583–R15585, 1999.

[52] A. A. Kiselev and K. W. Kim. T-shaped ballistic spin filter. *Applied Physics Letters*, 78:775–777, 2001.

[53] Al. L. Efros, E. I. Rashba, and M. Rosen. Paramagnetic ion-doped nanocrystal as a voltage-controlled spin filter. *Phys. Rev. Letters*, 87:206601–206604, 2001.

[54] Takaaki Koga, Junsaku Nitta, Hideaki Takayanagi, and Supriyo Datta. Spin-filter device based on the Rashba effect using a nonmagnetic resonant tunneling diode. *Phys. Rev. Letters*, 88:126601–126604, 2002.

[55] A. G. Mal'shukov and K. A. Chao. Optoelectric spin injection in semiconductor heterostructures without a ferromagnet. *Phys. Rev. B*, 65:R241308, 2002.

[56] M. Governale, D. Boese, U. Zülicke, and C. Schroll. Filtering spin with tunnel-coupled electron wave guides. *Phys. Rev. B*, 65:140403, 2002.

[57] O. Wunnicke, Ph. Mavropoulos, R. Zeller, P. H. Dederichs, and D. Grundler. Ballistic spin injection from Fe(001) into ZnSe and GaAs. *Phys. Rev. B*, 65:R241306, 2002.

[58] S. Bellucci and P. Onorato. Rashba effect in two-dimensional mesoscopic systems with transverse magnetic field. *Phys. Rev. B*, 68:245322, 2003.

[59] M. Zwierzycki, K. Xia, P. J. Kelly, G. E. W. Bauer, and I. Turek. Spin injection through an Fe/InAs interface. *Phys. Rev. B*, 67:092401, 2003.

[60] A. Shekhter, M. Khodas, and A. M. Finkel'stein. Diffuse emission in the presence of an inhomogeneous spin-orbit interaction for the purpose of spin filtration. *Phys. Rev. B*, 71:125114, 2005.

[61] S. D. Ganichev, V. V. Bel'kov, Petra Schneider, E. L. Ivchenko, S. A. Tarasenko, W. Wegscheider, D. Weiss, D. Schuh, E. V. Beregulin, and W. Prettl. Resonant inversion of the circular photogalvanic effect in *n*-doped quantum wells. *Phys. Rev. B*, 68:035319, 2003.

[62] M. Khodas, A. Shekhter, and A. M. Finkel'stein. Spin polarization of electrons by nonmagnetic heterostructures: The Basics of Spin Optics. *Phys. Rev. Letters*, 92:086602, 2004.

[63] R. Hanson, B. Witkamp, L. M. K. Vandersypen, L. H. Willems van Beveren, J. M. Elzerman, and L. P. Kouwenhoven. Zeeman energy and spin relaxation in a one-electron quantum dot. *Phys. Rev. Letters*, 91:196802, 2003.

[64] M. Yamamoto. priv. comm.

[65] M. C. W. van Rossum and Th. M. Nieuwenhuizen. Multiple scattering of classical waves: microscopy, mesoscopy, and diffusion. *Rev. Mod. Phys.*, 71:313–371, 1999.

[66] A. R. Dedigama, D. Deen, Sh. Murphy, N. Goel, M. Santos, K. Suzuki, S. Miyashita, and Y. Hirayama. Current focusing in InSb heterostructures. In *16TH International Conference on Electronic Properties of Two-Dimensional Systems: Final Program and Abtsracts*, 2005.

[67] Jan von Delft and Herbert Schoeller. Bosonization for beginners - refermionization for experts. *Annalen der Physik*, 7:225, 1998.

[68] S. Tomonaga. Remarks on Bloch's method of sound waves applied to many-fermion problems. *Prog. Theor. Phys.*, 5:544, 1950.

[69] D. C. Mattis and E. H. Lieb. Exact solution of a many fermion system and its associated boson field. *J. Math. Phys.*, 6:304, 1965.

[70] J. M. Luttinger. An exactly soluble model of a many-fermion system. *J. Math. Phys.*, 4:1154, 1963.

[71] K. D. Schotte and U. Schatte. Tomonaga's model and the threshold singularity of X-ray spectra of metals. *Phys. Rev.*, 182:479, 1969.

[72] D. C. Mattis. New wave-operator identity applied to the study of persistent currents in 1D. *J. Math. Phys.*, 15:609, 1974.

[73] A. Luther and I. Peschel. Single-particle states, Kohn anomaly, and pairing fluctuations in one dimension. *Phys. Rev. B*, 9:2911, 1974.

[74] R. Heidenreich, B. Schroer, R. Seiler, and D. Uhlenbrock. The sine-Gordon equation and the one-dimensional electron gas. *Phys. Lett.*, 54A:119, 1975.

[75] F. D. M. Haldane. Coupling between charge and spin degrees of freedom in the one-dimensional Fermi gas with backscattering. *J. Phys. C*, 12:4791, 1979.

[76] F. D. M. Haldane. 'Luttinger liquid theory' of one-dimensional quantum fluids. i. Properties of the Luttinger model and their extension to the general 1d interacting spinless Fermi gas. *J. Phys. C*, 14:2585, 1981.

[77] V. Meden and K. Schönhammer. Spectral functions for the Tomonaga-Luttinger model. *Phys. Rev. B*, 46:15753–15760, 1992.

[78] J. Voit. Charge-spin separation and the spectral properties of Luttinger liquids. *Phys. Rev. B*, 47:6740–6743, 1993.

[79] A.V. Shytov, L.I. Glazman, and O.A. Starykh. Zeeman splitting of zero-bias anomaly in Luttinger liquids. *Phys. Rev. Letters*, 91:046801, 2003.

[80] T. Kimura, K. Kuroki, and H. Aoki. Generation of spin-polarized currents in Zeeman-split Tomonaga-Luttinger models. *Phys. Rev. B*, 53:9572–9575, 1996.

[81] A.V. Moroz, K.V. Samokhin, and C.H.W. Barnes. Spin-orbit coupling in interacting quasi-one-dimensional electron systems. *Phys. Rev. Letters*, 84:4164, 2000.

[82] A.V. Moroz, K.V. Samokhin, and C.H.W. Barnes. Theory of quasi-one-dimensional electron liquids with spin-orbit coupling. *Phys. Rev. B*, 62:16900–16911, 2000.

[83] A.V. Moroz and C.H.W. Barnes. Effect of the spin-orbit interaction on the band structure and conductance of quasi-one-dimensional systems. *Phys. Rev. B*, 60:14272–14285, 1999.

[84] A.O. Gogolin, A.A. Nersesyan, and A.M. Tsvelik. *Bosonization in Strongly Correlated Systems*. Cambridge University Press, 1998.

[85] S. Coleman. Quantum sine-Gordon equation as the massive Thirring model. *Phys. Rev. D*, 11:2088, 1975.

[86] C. L. Kane and M. P. A. Fisher. Transport in a one-channel Luttinger liquid. *Phys. Rev. Letters*, 68:1220, 1992.

[87] C. L. Kane and M. P. A. Fisher. Transmission through barriers and resonant tunneling in an interacting one-dimensional electron gas. *Phys. Rev. B*, 46:15233, 1992.

[88] G. Mahan. *Many-Particle Physics*. Plenum Press, New York, 1981.

[89] I. S. Gradstein and I. M. Ryzhik. *Tables of integrals, series and products*. Fizmatgiz, Moscow, 1962.

[90] L.D. Landau and E.M. Lifshitz. *Quantum Mechanics: Non-relativistic Theory*. Pergamon Press, 1958.

[91] F. Mireles and G. Kirczenow. Ballistic spin-polarized transport and Rashba spin precession in semiconductor nanowires. *Phys. Rev. B*, 64:024426, 2001.

[92] C. H. Yang, M. J. Yang, K. A. Cheng, and J. C. Culbertson. Characterization of one-dimensional quantum channels in InAs/AlSb. *Phys. Rev. B*, 66:115306, 2002.

[93] E. N. Bulgakov and A. F. Sadreev. Spin-rotation for ballistic electron transmission induced by spin-orbit interaction. *Phys. Rev. B*, 66:075331, 2002.

[94] A. V. Chaplik and R. H. Blick. On geometric potentials in nanomechanical circuits, cond-mat/0308040.

[95] J. von Delft and H. Schoeller. Bosonization for beginners — refermionization for experts. *Ann. der Phys.*, 4:225–305, 1984.

[96] M. Büttiker. Quantized transmission of a saddle-point constriction. *Phys. Rev. B*, 41:7906–7909, 1990.

[97] D. Gammon. Electrons in artificial atoms. *Nature*, 405:899, 2000.

[98] R. J. Warburton, C. Schäflein, D. Haft, F. Bickel, A. Lorke, J. M. Garcia, W. Schoenfeld, and P. M. Petroff. Optical emission from a charge-tunable quantum ring. *Nature*, 405:926, 2000.

[99] T. V. Shahbazyan, I. E. Perakis, and M. E. Raikh. Spectral functions for the Tomonaga-Luttinger model. *Phys. Rev. B*, 64:115317, 2001.

Acknowledgments